Spring 2007

Low-thrust control of a lunar orbiter

Nathan Harl

Department:

LOW-THRUST CONTROL OF A LUNAR ORBITER

by

NATHAN ROBERT HARL

A THESIS

Presented to the Faculty of the Graduate School of the

UNIVERSITY OF MISSOURI-ROLLA

In Partial Fulfillment of the Requirements for the Degree

MASTER OF SCIENCE IN AEROSPACE ENGINEERING

2007

Approved by

Dr. Henry J. Pernicka, Advisor	Dr. Robert G. Landers

Dr. K. Krishnamurthy

ABSTRACT

In 2004, President Bush unveiled his Vision for Space Exploration (VSE) plan, which defined many goals for NASA including revisiting the Moon in unmanned and manned missions. As a result, there has been a renewed interest in the study of lunar missions, particularly pertaining to lunar orbits that would be suitable for mapping missions. One type of lunar orbit that is beneficial for a mapping mission is a Sun-synchronous orbit, which provides constant lighting conditions for imaging. However, lunar Sun-synchronous orbits do not exist naturally, and instead must be created and continuously maintained using active control hardware.

This thesis presents a method for maintaining a long-term lunar Sun-synchronous orbit using continuous low-thrust hardware. The control method is developed using optimal control theory, which involves controlling a system through the minimization of a desired cost function. The advantage of this method is that the creation of the cost function is entirely up to the user, and thus can be easily modified to control various orbital elements depending on the needs of the mission at hand. Weights can also be assigned to the elements in the cost function in order to prioritize the control of one element over another

A transition matrix algorithm is used to solve the optimal control problem. Simulations of this algorithm are presented which show its effectiveness for maintaining the Sun-synchronous condition, as well as keeping the orbit near-polar. Case studies are also presented which describe the effects on the trajectory and control magnitudes from changing the control weighting in the cost function.

ACKNOWLEDGMENTS

I would like to thank the University of Missouri-Rolla for providing me with many great opportunities to better myself as both a student and a person. I especially would like to thank my advisor Dr. Pernicka, not only for being such a great advisor and professor, but also for motivating me to pursue the field of orbital mechanics. I would also like to thank Dr. Landers and Dr. Krishnamurthy for serving on my graduate committee. Finally, I would like to thank my family and friends for constantly providing me with motivation and support throughout my academic career.

TABLE OF CONTENTS

LIST OF ILLUSTRATIONS

LIST OF TABLES

1. INTRODUCTION

1.1. INTRODUCTION TO SUN-SYNCHRONOUS ORBITS

With the announcement of NASA's Vision for Space Exploration there has been a renewed interest in lunar missions. One of the more significant goals of the VSE is to commence unmanned and manned missions to the Moon by 2008 and 2020, respectively. Each of these missions will require a lunar orbit that is tailored to satisfy predetermined mission requirements. One special type of lunar orbit that is useful for a variety of missions is a lunar Sun-synchronous orbit.

A Sun-synchronous orbit can be defined as a near-polar orbit in which the line of nodes rotates at such a rate that it is always oriented at a constant angle with a vector directed from the Sun to the body the spacecraft is orbiting [1]. Figure 1.1 depicts a lunar Sun-synchronous orbit, and shows how the line of nodes is oriented relative to the Sun by the angle ϕ in such an orbit.

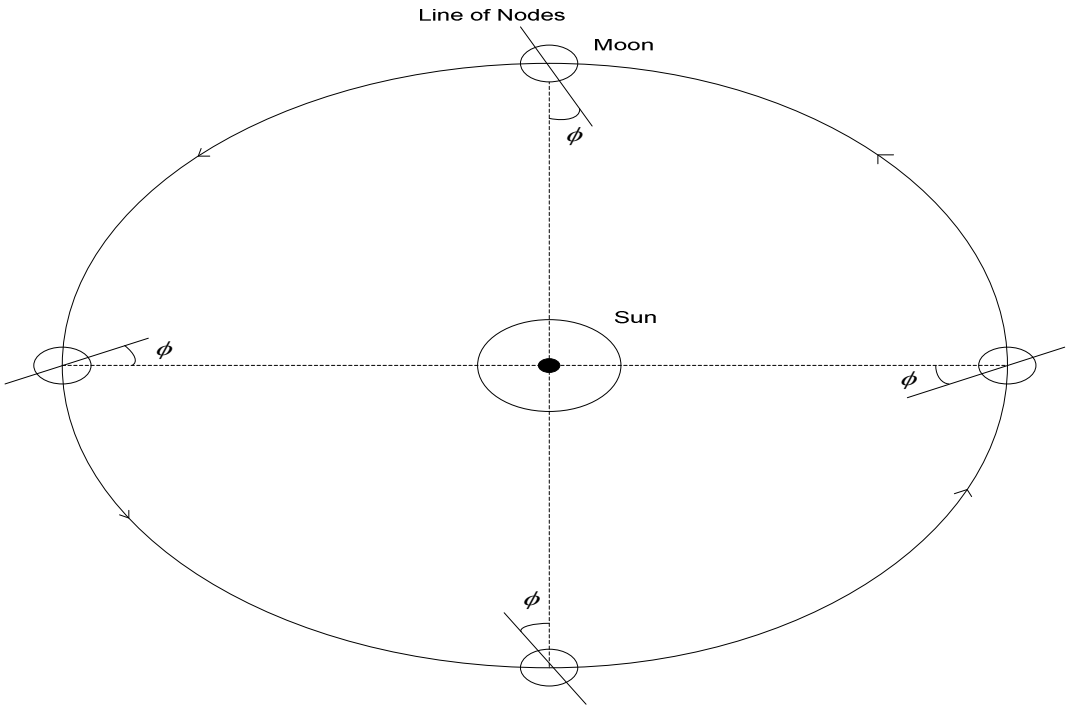

Figure 1.1. Example of a Sun-Synchronous Orbit

These types of orbits are useful for many reasons. For example, mapping missions can benefit from the constant lighting conditions along the spacecraft's groundtrack, and many more missions can benefit from the constant thermal environment due to unvarying solar exposure [1].

The exact rate at which the line of nodes needs to rotate in order for the orbit to be Sun-synchronous will generally depend on what body in space is being orbited. For example, since the Earth orbits the Sun in one sidereal year (365.2563 days), a Sun-synchronous orbit about the Earth would require a nodal rotation of 360°/365.2563 days, or 0.9856°/day. This rotation rate of 0.9856°/day would apply to a lunar Sun-synchronous orbit as well since the Moon also makes a full revolution around the Sun in one sidereal year.

Earth Sun-synchronous missions benefit from the Earth's oblateness or "bulge" about the equator, which allows for the generation of Sun-synchronous orbits that do not require maneuvers to maintain the orbit. The equatorial oblateness creates an out of plane gravitational force which, for orbits with certain altitudes and inclinations, can rotate an orbit at the desired Sun-synchronous rate [1]. Since the lunar oblateness is much less than the Earth's, this luxury is not present when trying to generate a lunar Sun-synchronous orbit. Instead, generating and maintaining a lunar Sun-synchronous orbit requires continuously applying an out-of-plane thrust to rotate the orbit at the desired rate.
The goal of this work was to develop methods to efficiently establish and maintain such lunar Sun-synchronous orbits.

1.2. THESIS OVERVIEW

Following this introductory section, the remainder of the document is organized as follows:

- Section 2 - This section reviews the current state of low-thrust hardware, summarizes low-thrust missions that have been proposed and studied, and gives an overview of previous work that has been performed in lunar Sun-synchronous orbit mission design.

- Section 3 - This section presents the equations of motion for a low-altitude lunar orbiter. The section ends with a case study of how increasing the degree and order of a lunar gravity model affects the results. Appendices A and B contain additional information related to this section.
- Section 4 – This section provides an introduction to optimal control theory, and goes on to derive an algorithm for controlling a lunar Sun-synchronous orbit.
- Section 5 – This section presents results generated from the controller described in Section 4 and contains case studies showing the effect of applying weights to the control requirements and the control inputs.
- Section 6 – This section summarizes the results gained from this work and provides conclusions.
- Section 7 – This section provides an overview of future developments for this research.

2. LITERATURE REVIEW

2.1. CURRENT STATE OF LOW-THRUST HARDWARE

While interest in the use of low-thrust systems for aerospace applications has been around since the 1960s, efficient and reliable low-thrust hardware has been developed only recently. Today, many commercial communication satellites are equipped with low-thrust systems, using the small thrust levels for orbit stationkeeping [2].Two of the most prevalent types of low-thrust hardware currently being used for space applications are Hall and Ion thrusters. This section summarizes a review of the capabilities of current Hall and ion thrusters.

Wilson in [2] discusses new Hall and Ion thrusters currently being produced by Aerojet. In terms of Hall systems, Aerojet is currently producing a Hall Thruster Propulsion System (HTPS) which uses a BPT-4000 Hall thruster. The power level of the HTPS can be toggled between 3 to 4.5 kW, giving a thrust range of 161 to 282 mN. Aerojet also recently developed the NEXT ion propulsion system. The NEXT system can operate at power levels ranging from 0.54-6.9 kW, with a maximum thrust that is greater than 236 mN. Aerojet developed the NEXT system with application to future NASA robotic exploration missions.

In [3], Spores and Birkan present current low-thrust hardware efforts within the U.S. Air Force (USAF). Of particular note is a dual-mode Hall thruster that the authors describe. Under development by the Busek Co., Inc., the thruster is being designed to toggle between a low and high thrust level. The thruster is expected to develop I_{sp} values greater than 1900 sec with a thrust near 550 mN, and also be able to operate at an I_{sp} of 1000 sec and a thrust of 750 mN.

NASA has also been working on low-thrust systems, developing a highly efficient ion propulsion system called Dawn [4], [5]. Dawn's engines have a specific impulse of 3100 s and a maximum thrust level of 90 mN. The Dawn ion propulsion system will be used on a mission to rendezvous with and map the two largest main-belt asteroids, Vesta and Ceres, and will be the first use of ion propulsion on a full-up NASA science mission. The launch of the spacecraft equipped with the Dawn system is planned for summer 2007.

In [6], Jacobson and Manzella describe the 457-M Hall Thruster developed by NASA. The thruster was tested over a range of 8.5 kW to 74.0 kW, and was found to produce thrust levels ranging from 390 mN to 2.5 N. In this test, Krypton was used as a propellant, rather than using the propellant most common in current Hall systems, Xenon. It was found that while using Krypton as a propellant increases the maximum thrust levels, it also leads to a slightly lower efficiency.

2.2. REVIEW OF LOW-THRUST MISSIONS

Due to many of the promising aspects of using low-thrust systems, previous work has been performed on applying a low-thrust analysis to various mission types. This section gives an overview of the types of previously researched missions that were identified of interest.

2.2.1. Low-Thrust Trajectory Optimization. One field that has seen many low-thrust analyses is trajectory optimization. Trajectory optimization can be defined as the process of designing a trajectory that minimizes or maximizes some measure of performance. The following are examples of the low-thrust work that has been done in this field.

Whiting studied optimal low-thrust transfers between LEO and GEO in [14]. What is unique about his method is that he presents a controller that simulates a thruster with variable specific impulse at constant power and others that include periods of coasting along the transfer. One of the coasting controllers involves turning off the engine whenever the spacecraft is in the Earth's shadow, a method which Whiting calls "Eclipse Control." When the spacecraft is in the Earth's shadow, the engine is power by solar panels alone, which helps conserve the batteries for use after the transfer. He compares the results from the various controllers, and shows that using Eclipse Control leads to the lowest total ΔV.

In [7], Kluever presents an approach to an Earth-Moon trajectory optimization problem. The approach consists of three phases: a continuous-thrust spiral escape trajectory from a Low-Earth Orbit (LEO), a sub-optimal translunar coasting phase, and then a continuous-thrust spiral capture trajectory at the Moon. Sequential Quadratic Programming (SQP) is used in solving the associated optimal control problem. Kluever

uses this approach for a planar Earth-Moon trajectory, with a total trip time of 7.73 days. He then adds more complexity to the approach in [8] by analyzing trajectories from LEO to an inclined low-lunar orbit. It was found that, compared to the planar case in [7], only 0.6% more fuel is required to transfer into a polar lunar orbit. The total trip time was found to be around 7.5 days for this case.

Kluever further examines the approach of [7] and [8] by specifying specific types of propulsion systems for the transfer. In [9], he examines a transfer using combined chemical-electrical propulsion. The spiral Earth-escape trajectory is replaced with a chemical-stage boost from LEO to the translunar coasting phase, and then the electrical system is used for the capture spiral to a lunar polar orbit. For the capture spiral, two types of electrical propulsion were studied: arcjet thrusters and stationary plasma thrusters (SPT). It was found that using the arcjet thrusters led to a total trip time of 46.4 days, and using an SPT system led to a total trip time of 48.52 days.

A low-thrust Earth-Moon trajectory problem was also analyzed by Conway and Herman in [10]. Rather than use the thrust-coast-thrust approach studied in [7-9] however, the authors study a fully continuous thrust trajectory from a Geostationary Earth Orbit (GEO) to a polar low-lunar orbit with no coasting phase. The authors also use an initial thrust acceleration of 10^{-4} g, a thrust level which is 30 times smaller than the magnitude assumed by Kluever. Their analysis led to a total trip time of 32.54 days.

In [11], Kim creates an optimization algorithm to solve general minimum time transfer trajectory optimization problems. Kim's approach consists of first generating an optimal trajectory with given boundary conditions using adaptive simulated annealing and Newton methods. Once this optimal trajectory is found, symmetry methods are used to find other optimal trajectories. The author analyzed Earth-Mars transfer and Earth-Mars-Earth transfers using electric propulsion and solar sail spacecraft.

In [12] and [13], Thorne studies minimum-time transfers between coplanar circular orbits. The transfers are performed using continuous thrust of constant magnitude. Thorne places special emphasis on employing methods of generating optimal initial costates.

2.2.2. Low-Thrust Stationkeeping. Low-thrust systems are particularly useful for missions which require orbital stationkeeping. Stationkeeping involves keeping a

spacecraft in a desired orbit despite all of the natural perturbations that would decay the orbit. Since most stationkeeping missions only require making small corrections in the orbit, low-thrust systems are becoming a crucial candidate for their success. Today, a vast majority of geostationary communication satellites are outfitted with electric propulsion systems for stationkeeping purposes [2]. The following summarizes research that has been performed into various low-thrust stationkeeping missions.

One of the earliest works relating to low-thrust stationkeeping was performed by Hunziker in 1970 [15]. In [15], Hunziker creates a controller for the purposes of stationkeeping a nearly circular equatorial orbit for a 24-hour satellite. The goal of his controller was to minimize the change in spacecraft longitude over the course of the integration, leading to the spacecraft staying directly overhead a certain point on the Earth and the "24-hour satellite" designation. Hunziker pursued a bang-bang controller approach to the problem, solving the problem using variation of parameters and correcting each initial estimate for the optimal trajectory using a Newton-Rhapson method. His controller was a success, leading to a maximum longitude change of only 0.4° over the course of 105 days.

More recently, the authors in [16] present an analysis of using solar electric propulsion (SEP) for insertion into a geostationary orbit and for 15 year North-South stationkeeping once in that geostationary orbit. The method involves using the remaining fuel in the Centaur stage of an Atlas IIAS rocket along with onboard chemical propulsion systems to insert the spacecraft into what the authors refer to as an "SEP starting orbit." Once on the SEP orbit, the electric propulsion systems are used to insert the spacecraft into GEO. Once in the GEO, the electric systems are used for North-South station keeping for a total of 15 years. The authors analyze the net mass increase associated by using SEP rather than chemical systems to insert into a GEO, and discover that the net mass is increased by as much as 45% through the use of SEP.

In [17], the authors compare two different strategies for the stationkeeping of a geostationary satellite using ionic propulsion. One of the strategies splits the stationkeeping into two branches: North-South (N-S) stationkeeping for controlling the inclination of the orbit and East-West (E-W) stationkeeping for controlling the eccentricity and longitude drift. The other strategy, created by the authors, involves

controlling the inclination, eccentricity, and longitude drift all together during N-S stationkeeping by making use of the large thruster cant angles. Simulations were performed, and it was found that performing all stationkeeping maneuvers during N-S stationkeeping required only 1 percent more fuel than controlling only inclination. The authors conclude that the N-S stationkeeping strategy is favorable when there are tight restrictions on the eccentricity, but the combined N-S and E-W stationkeeping strategy is more efficient for missions where the restrictions on eccentricity are not very strict.

In [18], Losa presents a geostationary low-thrust stationkeeping controller that uses a direct optimization approach. The controller is created with the goal of holding a satellite's latitude and longitude constant to within 0.01° for 28 days. For solving the control problem, a method called differential inclusion was used. Differential inclusion is a direct optimization approach which involves discretizing the state variable time history and replacing constraints on the control with constraints on values of the state variable time rates of change [19]. Using this approach, results were presented which showed the controller's success at keeping a satellite's latitude and longitude constant for 28 days, with a maximum required thrust force of around 40 mN.

2.2.3. Low-Thrust Rendezvous Missions. One final type of mission that has seen low-thrust research is the rendezvous mission. A rendezvous is defined as a mission where a spacecraft, usually called a chaser or interceptor, attempts to transfer from an initial state to a final state that coincides with some target body at some desired time. The target body is typically either another spacecraft or some small body in space such as an asteroid. The following is a summary of research that has been performed towards a variety of rendezvous missions.

One of the earliest works on low-thrust rendezvous was performed in 1964 by Edelbaum [20]. In [20], Edelbaum derives a method for the optimal correction of all six orbital elements of a general elliptic orbit. His method involves finding a closed-form analytic solution relating changes in the orbital elements to Lagrangian multipliers which define the control variables. Results are presented on the optimal thrust programs for changing various elements, and the author states that this method could also easily be applied to low-thrust stationkeeping.

Another early work on low-thrust rendezvous was performed by Billik [21]. In [21], Billik analyzed various low-thrust rendezvous missions by employing the technique of differential games. He presents solutions to three different rendezvous problems. The first problem, called a passive rendezvous, involves transferring the interceptor spacecraft from its initial state to a final state which is coincident with the target spacecraft. The second problem involves the transfer of the interceptor from some initial state to a final state in which the interceptor passes at some desired distance from the target, and is called a passive fly-by. Both of these problems involve an interceptor spacecraft with continuous thrust capabilities and a target body on a circular orbit that has no control capabilities. The final problem Billik presents is called active rendezvous, a case in which both vehicles have low-acceleration engines. This final problem can be seen as a "pursuit and evasion" type of problem, in which the interceptor spacecraft has to attempt rendezvous with a target spacecraft that is trying to escape. Billik presents solution methods to all three of these problems using optimal control theory and the technique of differential games.

In 1969, Euler further developed the passive rendezvous problem presented by Billik by analyzing coplanar rendezvous maneuvers between a maneuvering spacecraft and a nonmaneuvering target in an elliptic orbit [22]. The optimal rendezvous trajectories are found using a Newton-Rhapson algorithm, and Euler presents simulations showing that rendezvous with the target is successfully achieved with a maximum required thrust magnitude of around 0.016 N.

In [23], the authors study rendezvous missions to minor planets between Earth and Jupiter. Minor planets are also sometimes known as planetoids or asteroids, and account for thousands of bodies that orbit the Sun between Earth and Jupiter. The propulsion system used in the authors' analysis is a 30 cm Kaufman thruster with a thrust force of 0.132 N at a power input of 2.7 kW. Simulations are presented for rendezvous missions to ten different minor planets, with total flight times ranging from 240 to 480 days. The authors note that in several cases, enough propellant remains after rendezvous with the target minor planet for a continuation of the mission to a second target. One two-target mission of this type was studied to the bodies Aten and 1951 NL, both of which

orbit in nearly the same plane. The total trip time for this mission was found to be 807 days.

In [24], Aleshin and Guelman study low-thrust, fixed-time rendezvous missions between spacecraft in LEO. The authors present a method slightly different than previous papers by imposing constraints on the chaser's final approach to the target. Their approach to the problem involves a two-stage process. The first stage involves a transfer from the initial conditions to an intermediate point in the final line of approach, and the second stage involves the constrained terminal approach to the target approach. The authors present results showing how the terminal approach direction of the chaser spacecraft is successfully controlled. In [25], the authors expand their approach by imposing a constraint on the maximum control acceleration of 5×10^{-4} m/s^2. The authors present simulations of chaser trajectories with this control constraint and show that the optimal terminal approach direction is still obtained.

2.3. REVIEW OF WORK IN GENERATING LUNAR MAPPING ORBITS

Sun-synchronous orbits are useful for many different missions, but a mission type for which such orbits are specifically useful are mapping orbits. A mapping orbit is typically a low-altitude, polar orbit designed to obtain the maximum coverage of the body by a satellite equipped with cameras or other sensors. Due to an increasing interest in the Moon, most of the recent and upcoming lunar missions involve mapping of the lunar surface. Mapping orbits used to image of the surface benefit from the constant lighting conditions produced by a Sun-synchronous orbit. This section discusses some of the research into the field of lunar mapping and details some of the recent lunar mapping missions that have been conducted.

In [26], Park and Junkins present lunar mapping orbits that are created using a frozen orbit concept. A frozen orbit is typically defined as an orbit in which the eccentricity, argument of periapsis, and inclination variations are approximately zero. Such an orbit is "fixed" in its structure, hence the name frozen orbit. The authors show that by using this frozen orbit concept, lunar orbits can be obtained which are near circular, near constant low altitude, and near polar. It is also shown that at an inclination of 101.4°, a near Sun-synchronous orbit exists in which the orbit node deviates from the

Sun-synchronous condition by approximately 10° over one month. To obtain the frozen orbit conditions, the authors studied Lagrange's Planetary equations of motion. These equations are differential equations in terms of the six orbital elements, and a frozen orbit is found by finding the elements which make some of the derivatives equal to zero. Using this method, the authors found a frozen orbit which exists at an eccentricity of 0.0013 and an argument of periapsis of 90°. The authors present results which show that the orbit stays roughly frozen while keeping within 10° of the Sun-synchronous nodal condition over a month. After a month, however, the orbit node line will continue to rotate away from the Sun-synchronous condition.

Lunar mapping orbits are also studied by Ramanan and Adimurthy in [27]. The authors abandon the idea of identifying a Sun-synchronous orbit, and instead focus on finding a near polar, circular, low altitude lunar orbit with a long lifetime. In particular, the authors study the effect of the initial inclination on the lifetime of a 100 km altitude circular orbit. It is shown that the orbital lifetime is directly related to the inclination, minimizing at approximately 20 days for an initial inclination of 11° and lasting longer than 730 days for an initial inclination of 95°. For the 95° inclination case, the authors show that the periapsis altitude variation is only around 26 km. The authors also show that the initial ascending node can have an impact on the orbital lifetime, and that an initial ascending node of 120° can extend the lifetime by around 35 days.

Due to constantly evolving interest in the Moon, several lunar mapping missions have actually been conducted. One such mission is the 1994 Clementine mission that was jointly led by NASA and the Naval Research Laboratory (NRL) [28, 29]. The goals of the Clementine mission were to map the lunar surface through the use of an advanced sensor complement and then perform a close flyby of the asteroid 1620 Geographos. The lunar mapping portion of the mission involved a two month stay in a polar lunar orbit with an eccentricity of 0.36 and a semimajor axis of 5,116 km. During each orbit, 80 minutes of mapping was performed around periapsis with 139 minutes of downlink time around apoapsis. The periapsis location was initially 30 degrees below the lunar equator for the first month of the mapping mission, and a maneuver was performed to shift the periapsis to 30 degrees above the equator for the second month. The lunar mapping portion of the mission was a success, but a computer malfunction after the mapping phase

prevented Clementine from reaching its second objective of performing a flyby around Geographos.

After Clementine, the next lunar mapping mission to be performed was NASA's Lunar Prospector (LP) mission in 1998 [30]. The goals of the LP mission were to map the composition of the lunar surface, study the Moon's gravity and magnetic fields, investigate levels of tectonic and volcanic activity, and search for evidence of water ice at the Moon's poles. LP consisted of a one-year stay in a 100 km altitude polar mapping orbit, with correction maneuvers performed every 56 days to correct the eccentricity and argument of periapsis. In order to minimize the maneuvers required and maximize the orbital lifetime, the LP mapping orbit was a Quasi-Frozen orbit which lowered the eccentricity and argument of periapsis variations [31]. The LP mission was a success, providing a high-resolution map of the Moon as well as obtaining a large amount of data on the Moon's gravity field.

NASA is also currently planning another lunar mapping mission which will begin in 2008 [32, 33]. Called the Lunar Reconnaissance Orbiter (LRO) mission, some of its primary goals are to map mineralogy across the Moon, search for indications of ice, provide sub-meter resolution imaging of the Moon and to provide an assessment of possible lunar landing sites. The LRO will conduct its mission from a 50 km polar lunar orbit for a duration of one year. While no maneuvers are to be made to obtain a Sun-synchronous orbit, as explained in [33] stationkeeping maneuvers will be performed to correct the eccentricity and argument of periapsis drift. The stationkeeping maneuvers are intended to be performed once per lunar orbit period, or 27.4 days.

In light of the previous work performed in generating lunar mapping orbits, the efforts presented in this thesis can be seen as a strong advancement to the field. In particular, while previous efforts have been made towards generating short duration Sun-synchronous missions, a method for generating long-duration Sun-synchronous missions will be presented in this thesis. Also, it will be shown that Sun-synchronous orbits can be achieved using current-age low-thrust hardware, something which up to this point has not been a focus of study.

3. SYSTEM MODELS AND EQUATIONS OF MOTION

3.1. MEAN SELENOGRAPHIC REFERENCE FRAME

3.1.1. Definition of the Mean Selenographic Reference Frame. Since orbits about the Moon are to be analyzed, it is desired to solve the system dynamics in a reference frame that is fixed in the Moon. For this reason, a selenographic reference frame is chosen. A selenographic frame is defined as a rotating reference frame with the origin in the center of the Moon, where the $\hat{x}$, $\hat{y}$ and $\hat{z}$ axes correspond to the Moon's principal axes of inertia [34]. The $\hat{x}$ axis is in the Moon's equatorial plane pointing towards Earth, the $\hat{z}$ axis is through the Moon's north pole, and the $\hat{y}$ axis completes the right-handed coordinate system. Figure 3.1 depicts such a selenographic coordinate system.

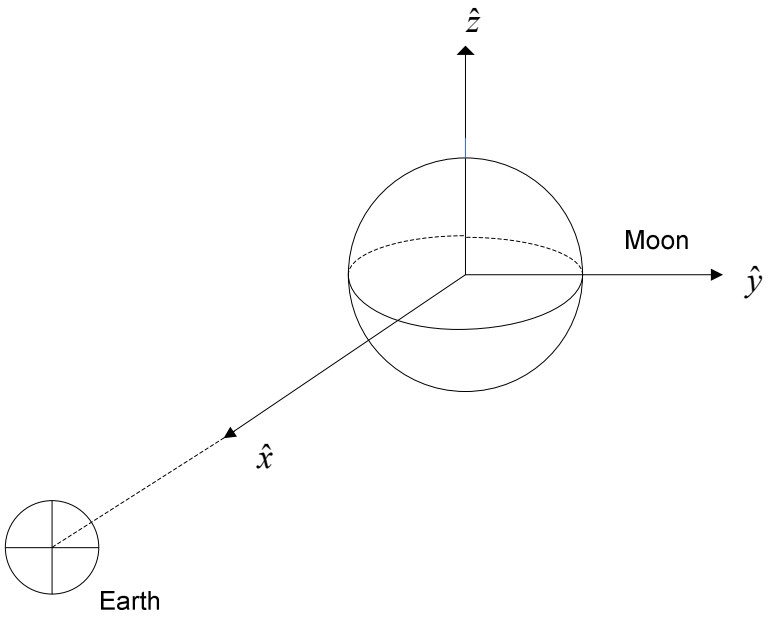

Figure 3.1. Example of Selenographic Coordinate Frame

Escobal in [34] describes two basic types of selenographic reference frames. One, called the true selenographic coordinate system, incorporates the physical librations of

the Moon, while another, the mean selenographic reference frame, does not include the librations. It was decided to use the mean selenographic reference frame for this initial analysis, due in part to the Moon's librations being very complicated to model and because the libration effects likely cause very small perturbations in the model.

3.1.2. Transformation from Ecliptic Frame to Mean Selenographic Frame.

In solving the equations of motion presented later, it will be necessary to convert from the ecliptic frame to the mean selenographic frame discussed in Section 3.1.1. The ecliptic frame is defined as the plane of Earth's orbit around the Sun. The $\hat{\boldsymbol{x}}$ axis of the ecliptic frame is directed towards the vernal equinox, the $\hat{z}$ axis is tilted approximately 23.44° from the Earth's north pole, and the $\hat{\boldsymbol{y}}$ axis completes the right-handed coordinate system. This coordinate transformation is required because position vectors originating from Earth, such as the vectors from the Earth to the Sun or from the Earth to the Moon, are typically defined in an ecliptic frame. The coordinate frame transformation which is described in this section is derived in Escobal [34].

It is first required to calculate some auxiliary angles that will be needed in the transformation. These angles are defined with respect to the independent variable

$$T_u = \frac{J.D. - (J.D.)_{Jan0.5,1900}}{36525} \tag{3.1}$$

where *J.D.* is the current Julian date with the epoch date taken as

$$(J.D.)_{Jan0.5,1900} = 2415020 \tag{3.2}$$

Now, define the variables λ_{moon} and Ω as follows [34],

$$\lambda_{moon} = 270.4341639° + 481{,}267.8831417° T_u - 0.001133333° {T_u}^2 + 0.1888889° x10^{-5} {T_u}^3 \tag{3.3}$$

$$\Omega = 259.1832750° - 1{,}934.1420083° T_u + 0.002077778° {T_u}^2 + 0.2222222 x10^{-5} {T_u}^3 \tag{3.4}$$

Ω is the longitude of the mean ascending of the lunar orbit measured in the ecliptic frame from the mean equinox of date, and λ_{moon} is the geocentric mean longitude of the Moon, $\lambda_{moon} = \Omega + \eta$, where η is the angle between the Moon and the location at which its orbit crosses the ecliptic plane. Equations (3.3) and (3.4) are very useful in that they give precise values for both λ_{moon} and Ω as a function of time.

Three different rotations are needed in order to convert from the ecliptic frame to the mean selenographic frame. Figure 3.2 shows these three required rotations.

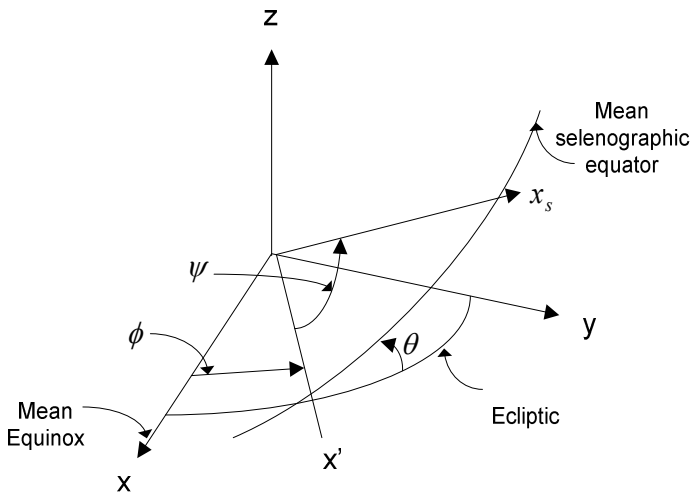

Figure 3.2. Transformation from Ecliptic to Mean Selenographic Frame

The first rotation, ϕ, is taken about the $\hat{z}$ axis of the ecliptic frame and is equal to

$$\phi = \Omega + \pi \tag{3.5}$$

The second rotation, θ, is taken about the intermediate $\hat{x}'$ axis and is equal to

$$\theta = I \tag{3.6}$$

where I is the mean inclination of the mean selenographic reference frame to the ecliptic frame which is equal to 1.53889°. The final rotation is about the resultant $\hat{z}''$ axis and is equal to

$$\psi = \lambda_{moon} - \Omega \tag{3.7}$$

The ϕ, θ, and ψ angles, also known as the Euler angles, are used to create a direction cosine matrix (DCM) which will convert a position vector expressed in the ecliptic frame to the mean selenographic frame. It should be noted that the trigonometric expressions in the following DCM are abbreviated as

$$S_\alpha = \sin(\alpha) \tag{3.8}$$

$$C_\alpha = \cos(\alpha) \tag{3.9}$$

The resulting DCM, as described in Escobal [34], is

$$DCM = \begin{bmatrix} C_\phi C_\psi - C_\theta S_\phi S_\psi & S_\phi C_\psi + C_\theta C_\phi S_\psi & S_\psi S_\theta \\ -S_\psi C_\phi - C_\theta S_\phi C_\psi & -S_\phi S_\psi + C_\theta C_\phi C_\psi & S_\theta C_\psi \\ S_\phi S_\theta & -C_\phi S_\theta & C_\theta \end{bmatrix} \tag{3.10}$$

With the DCM given by Equation (3.10), a position vector in the ecliptic frame can be expressed in the mean selenographic frame as

$$\boldsymbol{r}_{selenographic} = [DCM]\boldsymbol{r}_{ecliptic} \tag{3.11}$$

If it were also desired to convert velocities from the ecliptic to the mean selenographic frame, additional calculations would have to be made. However, since for this work only position vectors will need to be converted, Equation (3.11) will suffice.

3.2. DERIVATION OF THE EQUATIONS OF MOTION

In this section, the equations of motion of a low-altitude lunar orbiter will be derived. The equations will incorporate perturbations from Earth, the Sun, and the highly nonuniform lunar gravity field.

As depicted in Figure 3.3, the system consists of four bodies: Earth, Sun, Moon, and spacecraft. Also, the point "O" in Figure 3.3 is considered to be an inertially fixed point in space, and is needed for starting the derivations.

Let the vector from the Moon to the spacecraft be defined by

$$\boldsymbol{r}_{moon-s/c} = x\hat{\boldsymbol{x}} + y\hat{\boldsymbol{y}} + z\hat{\boldsymbol{z}} \tag{3.12}$$

where the $\hat{\boldsymbol{x}}$, $\hat{\boldsymbol{y}}$ and $\hat{\boldsymbol{z}}$ axes correspond to the mean selenographic frame described in Section 3.1. This position vector is defined with respect to a rotating reference frame, but the velocity and acceleration vectors must be expressed in an inertial reference frame in order to be used in Newton's Law.

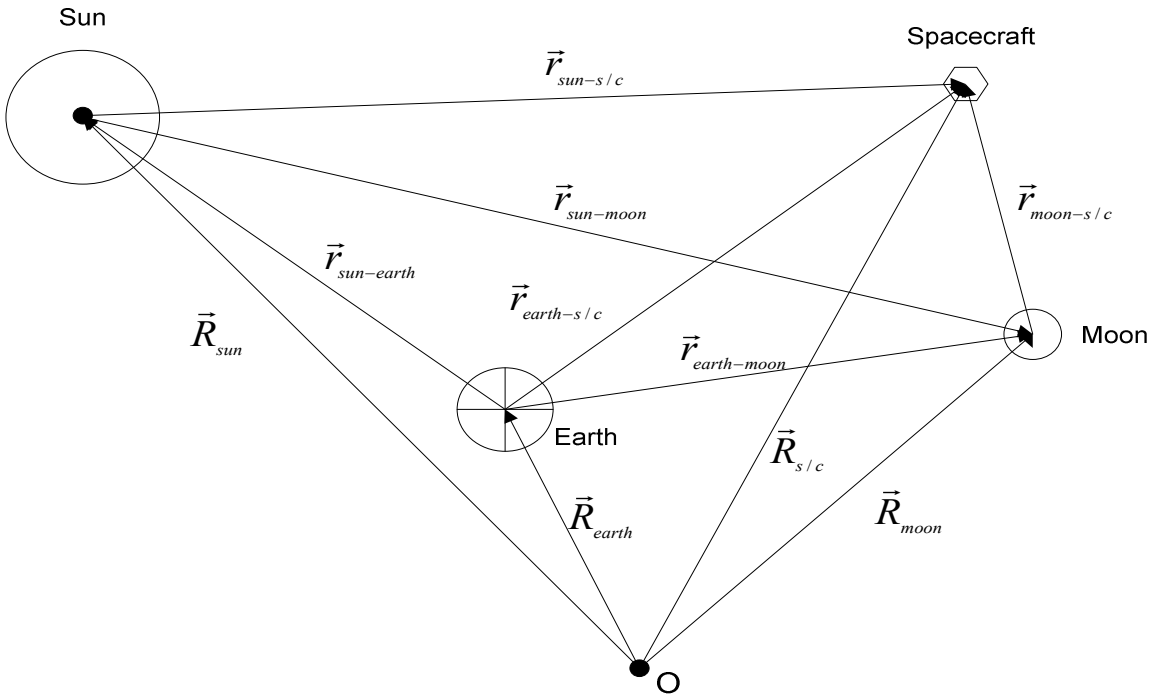

Figure 3.3. Four-Body Sun-Earth-Moon-Spacecraft System

In order to express the velocity and acceleration with respect to an inertial reference frame, the basic kinematic equation (BKE) must be used to express the first and second derivatives of (3.12) as

$$\dot{\boldsymbol{r}}_{moon-s/c} = \frac{{}^{I}d\boldsymbol{r}_{moon-s/c}}{dt} = \frac{{}^{R}d\boldsymbol{r}_{moon-s/c}}{dt} + {}^{I}\boldsymbol{w}^{R} x \boldsymbol{r}_{s/c} \tag{3.13}$$

$$\ddot{\boldsymbol{r}}_{moon-s/c} = \frac{{}^{I}d^{2}\boldsymbol{r}_{moon-s/c}}{dt^{2}} = \frac{{}^{R}d^{2}\boldsymbol{r}_{moon-s/c}}{dt^{2}} + {}^{I}\boldsymbol{w}^{R} x \frac{{}^{I}d\boldsymbol{r}_{moon-s/c}}{dt} \tag{3.14}$$

where ${}^{I}\boldsymbol{w}^{R} = w_m \hat{\boldsymbol{z}}$ and $w_m = 2.661699x10^{-6}$ rad/sec is the Moon's rotational velocity. Evaluating (3.13) and (3.14) leads to

$$\dot{\boldsymbol{r}}_{moon-s/c} = (\dot{x} - w_m y)\hat{\boldsymbol{x}} + (\dot{y} + w_m x)\hat{\boldsymbol{y}} + \dot{z}\hat{\boldsymbol{z}} \tag{3.15}$$

$$\ddot{\boldsymbol{r}}_{moon-s/c} = (\ddot{x} - 2w_m \dot{y} - w_m{}^{2} x)\hat{\boldsymbol{x}} + (\ddot{y} + 2w_m \dot{x} - w_m{}^{2} y)\hat{\boldsymbol{y}} + \ddot{z}\hat{\boldsymbol{z}} \tag{3.16}$$

Equations (3.15) and (3.16) give the inertial position and velocity of the spacecraft with respect to the Moon.

Next, using Newton's Law

$$m_{s/c}\ddot{\boldsymbol{R}}_{s/c} = \boldsymbol{F}_{s/c} \tag{3.17}$$

where $\boldsymbol{F}_{s/c}$ is the sum of the external forces on the spacecraft. Also, from Figure 3.3

$$\boldsymbol{R}_{s/c} = \boldsymbol{R}_{moon} + \boldsymbol{r}_{moon-s/c} \tag{3.18}$$

From (3.18), it can be seen that

$$\ddot{\boldsymbol{r}}_{moon-s/c} = \ddot{\boldsymbol{R}}_{s/c} - \ddot{\boldsymbol{R}}_{moon} \tag{3.19}$$

Now, it can be shown that

$$m_{\boldsymbol{s/c}}\ddot{\boldsymbol{R}}_{s/c} = -G\frac{m_{s/c}m_{earth}}{r_{earth-s/c}^{3}}\boldsymbol{r}_{earth-s/c} - G\frac{m_{s/c}m_{sun}}{r_{sun-s/c}^{3}}\boldsymbol{r}_{sun-s/c} + m_{\boldsymbol{s/c}}\nabla U_{Moon} \tag{3.20}$$

and that

$$m_{\boldsymbol{moon}}\ddot{\boldsymbol{R}}_{moon} = -G\frac{m_{moon}m_{earth}}{r_{earth-moon}^{3}}\boldsymbol{r}_{earth-moon} - G\frac{m_{moon}m_{sun}}{r_{sun-moon}^{3}}\boldsymbol{r}_{sun-moon} \tag{3.21}$$

where from Figure 3.3

$$\boldsymbol{r}_{earth-sc} = \boldsymbol{r}_{earth-moon} + \boldsymbol{r}_{moon-s/c} \tag{3.22}$$

$$\boldsymbol{r}_{sun-sc} = -\boldsymbol{r}_{earth-sun} + \boldsymbol{r}_{earth-moon} + \boldsymbol{r}_{moon-sc} \tag{3.23}$$

$$\boldsymbol{r}_{sun-moon} = -\boldsymbol{r}_{earth-sun} + \boldsymbol{r}_{earth-moon} \tag{3.24}$$

In Equations (3.20) and (3.21), $G = 6.673x10^{-20}\,\frac{\mathrm{km}^3}{\mathrm{kg.s}^2}$ is the universal gravitational constant, ∇U_{Moon} is the gradient of the lunar gravity potential which is defined in the next section, and m_{earth}, m_{sun}, and m_{moon} correspond to the masses of the Earth, Sun, and Moon, respectively. Ephemeris equations presented in Escobal [34] and in the JPL software Quick [35, 36] are used to solve for $\boldsymbol{r}_{earth-moon}$ and $\boldsymbol{r}_{earth-sun}$ in Equations (3.22-3.24). The ephemeris equations give accurate positions of the bodies as a function of the current

Julian Date. Since both vectors are computed in the ecliptic frame, they have to be converted into the selenographic frame through the process detailed in Section 3.1.2.

Now, define the gravitational parameter terms $\mu_{earth} = Gm_{earth}$ and $\mu_{sun} = Gm_{sun}$. Dividing Equations (3.20) and (3.21) by $m_{s/c}$ and m_{moon}, respectively and substituting the resultant equations into Equation (3.19) yields

$$\ddot{\boldsymbol{r}}_{moon-s/c} = \frac{-\mu_{earth}}{r_{earth-s/c}^{\ 3}}\boldsymbol{r}_{earth-s/c} - \frac{\mu_{sun}}{r_{sun-s/c}^{\ 3}}\boldsymbol{r}_{sun-s/c} + \frac{\mu_{earth}}{r_{earth-moon}^{\ 3}}\boldsymbol{r}_{earth-moon} + \frac{\mu_{sun}}{r_{sun-moon}^{\ 3}}\boldsymbol{r}_{sun-moon} + \nabla U_{Moon} \tag{3.25}$$

It is now desired to convert this second-order system into a first-order form. Let the state vector $\vec{\mathbf{x}}$ be defined as

$$\boldsymbol{x} = \begin{bmatrix} x_1 \\ x_2 \\ x_3 \\ x_4 \\ x_5 \\ x_6 \end{bmatrix} = \begin{bmatrix} x \\ y \\ z \\ \dot{x} \\ \dot{y} \\ \dot{z} \end{bmatrix} \tag{3.26}$$

Also, allow for the possibility of a control acceleration along each direction as u_1, u_2, and u_3, respectively. By setting Equation (3.16) equal to Equation (3.25), the six differential equations are obtained

$$\dot{x}_1 = x_4 \tag{3.27}$$

$$\dot{x}_2 = x_5 \tag{3.28}$$

$$\dot{x}_3 = x_6 \tag{3.29}$$

$$\dot{x}_4 = 2w_m x_5 + w_m{}^2 x_1 - \frac{\mu_{earth} r_{earth-sc_x}}{\left|\boldsymbol{r}_{earth-sc}\right|^3} - \frac{\mu_{sun} r_{sun-sc_x}}{\left|\boldsymbol{r}_{sun-sc}\right|^3} + \frac{\mu_{earth} r_{earth-moon_x}}{\left|\boldsymbol{r}_{earth-moon}\right|^3} + \frac{\mu_{sun} r_{sun-moon_x}}{\left|\boldsymbol{r}_{sun-moon}\right|^3} + \nabla U_{Moon_x} + u_1 \tag{3.30}$$

$$\dot{x}_5 = -2w_m x_4 + w_m{}^2 x_2 - \frac{\mu_{earth} r_{earth-sc_y}}{\left|\boldsymbol{r}_{\boldsymbol{earth-sc}}\right|^3} - \frac{\mu_{sun} r_{sun-sc_y}}{\left|\boldsymbol{r}_{\boldsymbol{sun-sc}}\right|^3} + \frac{\mu_{earth} r_{earth-moon_y}}{\left|\boldsymbol{r}_{\boldsymbol{earth-moon}}\right|^3} + \frac{\mu_{sun} r_{sun-moon_y}}{\left|\boldsymbol{r}_{\boldsymbol{sun-moon}}\right|^3} + \nabla U_{Moon_y} + u_2 \tag{3.31}$$

$$\dot{x}_6 = \frac{-\mu_{earth} r_{earth-sc_z}}{\left|\boldsymbol{r}_{\boldsymbol{earth-sc}}\right|^3} + \frac{\mu_{sun} r_{sun-scz}}{\left|\boldsymbol{r}_{\boldsymbol{sun-sc}}\right|3} + \frac{\mu_{earth} r_{earth-moon_z}}{\left|\boldsymbol{r}_{\boldsymbol{earth-moon}}\right|^3} + \frac{\mu_{sun} r_{sun-moon_z}}{\left|\boldsymbol{r}_{\boldsymbol{sun-moon}}\right|^3} + \nabla U_{Moon_z} + u_3 \tag{3.32}$$

Equations (3.27-3.32) represent six first-order equations that specify the dynamics of a low-altitude lunar orbiter under perturbations from Earth, the Sun, and the Moon's gravity field. The lunar gravitational potential term, ∇U_{Moon}, in Equations (3.30-3.32) is derived in the following section.

3.3. DERIVATION OF LUNAR GRAVITATIONAL POTENTIAL

The primary perturbation that a low-altitude lunar orbiter experiences comes from the Moon's highly nonspherical gravity field. Therefore, a good model of the lunar gravitational potential is crucial for obtaining a high-fidelity dynamic model. This section will describe a numerical method for calculating the gradient of the lunar gravitational potential using the most recent gravity model available for the Moon. A majority of the analysis in this section is taken from Vallado [37].

As described in Vallado [37], the gravitational potential *U* of any general body can be described as

$$U = G\sum_{Q=1}^{\infty} \frac{m_Q}{\rho_Q} \tag{3.33}$$

where G is the gravitational constant of the body, m_Q is an infinitesimal mass on the body, and ρ_Q, called the slant range, is defined as the distance from the infinitesimal mass to some point in space P at which it desired to evaluate the potential. In this case, point P will correspond to a satellite. Figure 3.4 shows the geometry involved.

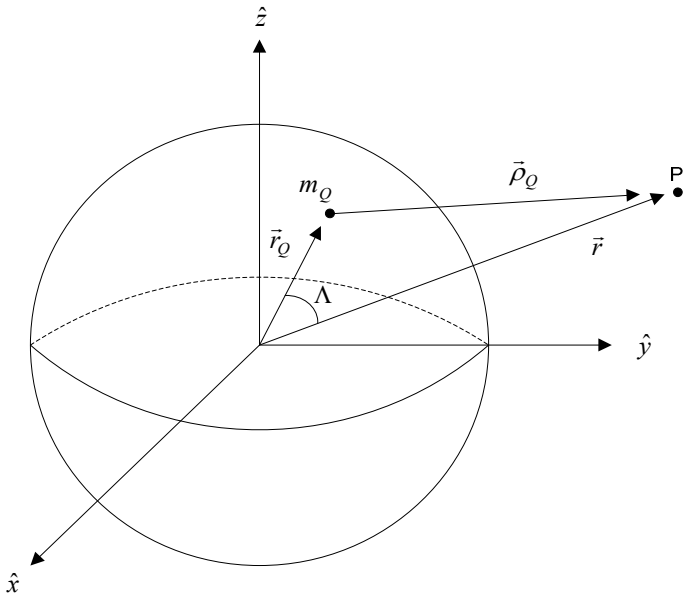

Figure 3.4. Setup for the Lunar Gravitational Potential Derivation

Equation (3.33) can further be expressed in the form of an integral over the entire body as

$$U = G \int_{Body} \frac{1}{\rho_Q} dm \tag{3.34}$$

Now, define the geocentric distance from the body to the satellite at point P as r and the distance from the center of the body to the infinitesimal point as r_Q where

$$r = \sqrt{x^2 + y^2 + z^2} \tag{3.35}$$

$$r_Q = \sqrt{\varepsilon^2 + \eta^2 + \xi^2} \tag{3.36}$$

Using the law of cosines, the slant range ρ_Q can be computed as

$$\rho_Q^2 = r^2 - 2 r r_Q \cos(\Lambda) \tag{3.37}$$

where as shown in Figure 3.4, Λ is the angle between the $\boldsymbol{r}$ and $\boldsymbol{r}_Q$ vectors. The Λ angle can be computed through the dot product of the position vectors as

$$\cos(\Lambda) = \frac{x\varepsilon + y\eta + z\xi}{rr_Q} = \frac{\boldsymbol{r} \cdot \boldsymbol{r}_Q}{rr_Q} \tag{3.38}$$

Inserting Equation (3.38) in Equation (3.37), the slant range is now

$$\rho_Q = r\sqrt{1 - 2\alpha\cos(\Lambda) + \alpha^2} \tag{3.39}$$

where

$$\alpha = \frac{r_Q}{r} \tag{3.40}$$

Using Equation (3.38), the gravitational potential of the body now becomes

$$U = G \int_{Body} \frac{dm}{r\sqrt{1 - 2\alpha\cos(\Lambda) + \alpha^2}} \tag{3.41}$$

The α variable will always be less than 1.0 for a point P outside the body, and the absolute value of the $\cos(\Lambda)$ quantity will always be less than or equal than 1.0, therefore the binomial theorem can be used to expand the denominator of Equation (3.41) into a series. As explained in Vallado [37], this leads to the following equation for the gravitational potential *U:*

$$U = \frac{G}{r} \int_{Body} \sum_{l=0}^{\infty} \alpha^l P_l[\cos(\Lambda)] dm \tag{3.42}$$

The $P_l[\cos(\Lambda)]$ term in Equation (3.42) is referred to as a Legendre polynomial, and the full equation involves a series of Legendre polynomials. Setting $\cos(\Lambda) = \omega$, Vallado [37] gives an equation for the Legendre polynomials as

$$P_l[\omega] = \frac{1}{2^l l!} \frac{d^l(\omega^2 - 1)^l}{d\omega^l} = \frac{1}{2^l} \sum_{j=0}^{\infty} \frac{(-1)^j (2l - 2j)!}{j!(l-j)!(l-2j)!} \omega^{l-2j} \tag{3.43}$$

The first six Legendre polynomials are

$$P_0[\omega] = 1 \tag{3.44}$$

$$P_1[\omega] = \omega \tag{3.45}$$

$$P_2[\omega] = \frac{1}{2}(3\omega^2 - 1) \tag{3.46}$$

$$P_3[\omega] = \frac{1}{2}(5\omega^3 - 3\omega) \tag{3.47}$$

$$P_4[\omega] = \frac{1}{8}(35\omega^4 - 30\omega^2 + 3) \tag{3.48}$$

$$P_5[\omega] = \frac{1}{8}(63\omega^5 - 70\omega^3 + 15\omega) \tag{3.49}$$

It should also be noted that the l=0 term of Equation (3.42) is

$$U_0 = \frac{G}{r}\int dm = \frac{Gm}{r} = \frac{\mu}{r} \tag{3.50}$$

which is the standard equation for the gravitational potential of a spherically symmetric and homogenous body. For some bodies Equation (3.50) is a good approximation for the gravitational potential, but due to the Moon's nonspherical gravity field an accurate high-fidelity model for a lunar orbiter involves computing a large amount of the terms in Equation (3.42).

In order to compute the Legendre polynomials for large degrees of l, the following recursive algorithm is used.

- Define the first two Legendre polynomials by Equations (3.44) and (3.45).
- Use Bonnet's recursion to solve for the rest of the Legendre polynomials up to a desired maximum degree l_{max}:

$$P_{l+1}(\omega) = \frac{2l+1}{l+1}\omega P_l(\omega) - \frac{l}{l+1}P_{l-1}(\omega) \tag{3.51}$$

Further simplifying Equation (3.42), Vallado [37] illustrates that by using the addition theorem of spherical harmonics the $P_l[\cos(\Lambda)]$ term can also be expressed as

$$\begin{aligned} P_l[\cos(\Lambda)] = {} & P_l[\sin(\phi_{gc_Q})]P_l[\sin(\phi_{gc_{sat}})] + 2\sum_{m=1}^{l}\frac{(l-m)!}{(l+m)!}\{P_{l,m}[\sin(\phi_{gc_Q})]\cos(m\lambda_Q)\cdot \\ & P_{l,m}[\sin(\phi_{gc_{sat}})]\cos(m\lambda_{sat}) + P_{l,m}[\sin(\phi_{gc_Q})]\sin(m\lambda_Q)\cdot P_{l,m}[\sin(\phi_{gc_{sat}})]\cos(m\lambda_{sat})\} \end{aligned} \tag{3.52}$$

where ϕ_{gc_Q}, λ_Q, ϕ_{gc_P} and λ_P are the geocentric latitude and longitude of the infinitesimal mass on the body and the point P, respectively, and the summation indices *l* and *m* are the degree and order, respectively.

The $P_{l,m}$ terms in Equation (3.52) are referred to as associated Legendre functions. These functions have the general form of

$$P_{l,m}(\omega) = \frac{1}{2^l l!}(1-\omega^2)^{m/2}\frac{d^{l+m}}{d\omega^{l+m}}(\omega^2-1)^l = (1-\omega^2)^{m/2}\frac{d^m}{d\omega^m}P_l(\omega) \tag{3.53}$$

Some of the first few associate Legendre functions are

$$P_{0,0} = 1 \tag{3.54}$$

$$P_{1,0} = \sin(\phi_{gc_{sat}}) \tag{3.55}$$

$$P_{1,1} = \cos(\phi_{gc_{sat}}) \tag{3.56}$$

$$P_{2,0} = \frac{1}{2}\left\{3\sin^2(\phi_{gc_{sat}})-1\right\} \tag{3.57}$$

$$P_{2,1} = 3\sin(\phi_{gc_{sat}})\cos(\phi_{gc_{sat}}) \tag{3.58}$$

$$P_{2,2} = 3\cos^2(\phi_{gc_{sat}}) \tag{3.59}$$

When *m* = 0, or for zero order, the associated Legendre function is equal to the Legendre polynomial evaluated at the same value of *l*.

While Equation (3.53) is sufficient for hand calculations, it is inefficient for calculations on a computer due to the derivative term. Therefore, it is desired to obtain a recursive equation for computing the associated Legendre functions that would be easy to implement on computer software. The following algorithm is used for obtaining this recursive equation:

- First define the three starting values for the associated Legendre functions by Equations (3.54-3.56). Also define the three starting values for the derivative term in Equation (3.53) as

$$\frac{d^0}{d\omega^0}P_0(\omega) = 1 \tag{3.60}$$

$$\frac{d^0}{d\omega^0}P_1(\omega)=\omega \tag{3.61}$$

$$\frac{d}{d\omega}P_1(\omega)=1 \tag{3.62}$$

- Use the following recursive equation for calculating the derivatives of the Legendre polynomials up to some l_{max} and m_{max}:

$$\frac{d^m}{d\omega^m}P_l(w)=\frac{d^m}{d\omega^m}P_{l-2}(\omega)+(2l-1)\frac{d^{m-1}}{d\omega^{m-1}}P_{l-1}(\omega) \tag{3.63}$$

  It should be noted that for the cases where $m = 0$, $\frac{d^m}{d\omega^m}P_l(\omega)=P_l(\omega)$.

- With the derivatives obtained from Equation (3.63), the associated Legendre functions can be computed using Equation (3.53).

With expressions obtained for the associated Legendre functions, Equation (3.42) can now be separated into terms that are dependent on the satellite's location and terms that only depend on the central body. While all of the equations before this point would apply for any general body, at this point the focus will change to specifically choosing the Moon as the central body. The Moon's radius will be defined as R_{Moon}, which is equal to 1737.4 km, and the mass of the Moon will be defined as m_{Moon}, which is equal to $7.36\text{x}10^{22}$ kg. To begin the separation of the terms in Equation (3.42) define the following coefficients:

$$C'_{l,m}=\int_{Moon} r_Q^l\, 2\frac{(l-m)!}{(l+m)!}P_{l,m}[\sin(\phi_{gc_Q})]\cos(m\lambda_Q)dm \tag{3.64}$$

$$S'_{l,m}=\int_{Moon} r_Q^l\, 2\frac{(l-m)!}{(l+m)!}P_{l,m}[\sin(\phi_{gc_Q})]\sin(m\lambda_Q)dm \tag{3.65}$$

The $C'_{l,m}$ and $S'_{l,m}$ coefficients in Equations (3.64) and (3.65) represent the mathematical modeling of the Moon's shape using spherical harmonics and are referred to as gravitational coefficients. Each of the gravitational coefficients describes surface spherical harmonics for some point on the Moon. For example, the $m = 0$ coefficients

describe zonal harmonics and represent bands of latitude , the $l=m$ coefficients describe sectorial harmonics which represent bands of longitude, and the $l \neq m$ terms describe tesseral harmonics indicating specific regions of the Moon. Also, if the center of the coordinate system corresponds with the attracting body's center of mass, the coefficients $C'_{1,0}$, $C'_{1,1}$ and $S'_{1,1}$ are equal to zero.

Substituting Equations (3.64) and (3.65) into Equation (3.42) leads to the following series representation for U:

$$U = \frac{G}{r}\sum_{l=0}^{\infty}\frac{P_l[\sin(\phi_{gc_{sat}})]}{r^l}C'_{l,0} + \frac{G}{r}\sum_{l=1}^{\infty}\sum_{m=1}^{l}\frac{P_{l,m}[\sin(\phi_{gc_{sat}})]}{r^l}\left\{C'_{l,m}\cos(m\lambda_{sat}) + S'_{l,m}\sin(m\lambda_{sat})\right\} \quad (3.66)$$

It is seen from Equation (3.65) that in order to have proper units, the C' and S' gravitational coefficients will need to be nondimensionalized. Therefore, the coefficients are nondimensionalized as

$$C_{l,m} = \frac{C'_{l,}\,m}{R^l_{Moon}m_{Moon}} \quad (3.67)$$

$$S_{l,m} = \frac{S'_{l,m}}{R^l_{Moon}m_{Moon}} \quad (3.68)$$

Substituting Equations (3.67) and (3.68) into Equation (3.66) and noting that the U_0 term is defined by Equation (3.50), the final equation for the gravitational potential is obtained as

$$U = \frac{\mu}{r}\left[1 + \sum_{l=2}^{\infty}\sum_{m=0}^{l}\left(\frac{R_{Moon}}{r}\right)^l P_{l,m}[\sin(\phi_{gc_{sat}})]\left\{C_{l,m}\cos(m\lambda_{sat}) + S_{l,m}\sin(m\lambda_{sat})\right\}\right] \quad (3.69)$$

The C and S gravitational coefficients are typically computed from observing the results of missions that have been conducted around the desired central body. For the Moon, many missions have been conducted, some of which are the Apollo Missions, the Clementine Mission, and the Lunar Prospector mission. Current lunar gravity models contain C and S coefficients that have been determined using the results from many of these missions. The lunar gravity model used in this work is the LP165P gravity model

obtained from the NASA PDS Geosciences Node, which contains lunar *C* and *S* coefficients up to a degree and order of 165x165 [39]. This gravity model is free for public use, and was obtained off of the NASA website.

Now that the gravitational potential function is defined by Equation (3.69), the next step is to calculate the acceleration, equal to the gradient of the gravitational potential function defined as

$$\nabla U_{Moon} = \frac{\partial U}{\partial \boldsymbol{r}} = \left\langle \frac{\partial U}{\partial x}, \frac{\partial U}{\partial y}, \frac{\partial U}{\partial z} \right\rangle \tag{3.70}$$

However, since U is defined in terms of spherical coordinates (r, ϕ_{gc_P} , λ_P) and it is desired to find the acceleration is Cartesian coordinates (x, y, z), the chain rule must be applied. This leads to the equation for the gradient as

$$\nabla U_{Moon} = \frac{\partial U}{\partial r}\left(\frac{\partial r}{\partial \boldsymbol{r}}\right)^T + \frac{\partial U}{\partial \varphi_{gc_{sat}}}\left(\frac{\partial \varphi_{gc_{sat}}}{\partial \boldsymbol{r}}\right)^T + \frac{\partial U}{\partial \lambda_{sat}}\left(\frac{\partial \lambda_{sat}}{\partial \boldsymbol{r}}\right) \tag{3.71}$$

where

$$\frac{\partial U}{\partial r} = -\frac{\mu}{r^2}\left[1 + \sum_{l=2}^{\infty}\sum_{m-0}^{l}\left(\frac{R_{moon}}{r}\right)^l (l+1) P_{l,m}[\sin(\phi_{gc_{sat}})]\left\{C_{l,m}\cos(m\lambda_{sat}) + S_{l,m}\sin(m\lambda_{sat})\right\}\right] \tag{3.72}$$

$$\begin{aligned}\frac{\partial U}{\partial \phi_{gc_{sat}}} = \frac{\mu}{r}\sum_{l=2}^{\infty}\sum_{m=0}^{l}\left(\frac{R_{moon}}{r}\right)^l \left\{P_{l,m+1}[\sin(\phi_{gc_{sat}})] - m\tan(\phi_{gc_{sat}}) P_{l,m}[\sin(\phi_{gc_{sat}})]\right\} \\ \times\left\{C_{l,m}\cos(m\lambda_{sat}) + S_{l,m}\sin(m\lambda_{sat})\right\}\end{aligned} \tag{3.73}$$

$$\frac{\partial U}{\partial \lambda_{sat}} = \frac{\mu}{r}\sum_{l=2}^{\infty}\sum_{m=0}^{l}\left(\frac{R_{moon}}{r}\right)^l m P_{l,m}[\sin(\phi_{gc_{sat}})]\left\{S_{l,m}\cos(m\lambda_{sat}) - C_{l,m}\sin(m\lambda_{sat})\right\} \tag{3.74}$$

$$\frac{\partial r}{\partial \boldsymbol{r}} = \frac{\boldsymbol{r}^T}{r} \tag{3.75}$$

$$\frac{\partial \varphi_{gc_{sat}}}{\partial \boldsymbol{r}} = \frac{1}{\sqrt{r_x^2 + r_y^2}} \left(-\frac{\boldsymbol{r}^T r_z}{r^2} + \frac{\partial r_z}{\partial \boldsymbol{r}} \right) \tag{3.76}$$

$$\frac{\partial \lambda_{sat}}{\partial \boldsymbol{r}} = \frac{1}{r_x^2 + r_y^2} \left(r_x \frac{\partial r_y}{\partial \boldsymbol{r}} - r_y \frac{\partial r_x}{\partial \boldsymbol{r}} \right) \tag{3.77}$$

After the substitution of Equations (3.72-3.77) into Equation (3.71), Equation (3.71) can be used to solve for the acceleration induced by the lunar gravitational potential. The three components of Equation (3.70), ∇U_{Moon_x}, ∇U_{Moon_y}, and ∇U_{Moon_z} are then used in the equations of motion for the satellite, Equations (3.27-3.32). As explained at the beginning of this section, the lunar gravitational potential is one of the main perturbations on a low-altitude lunar orbiter, thus the addition of Equation (3.71) to the equations of motion greatly increases the fidelity of the dynamic model.

3.4. DYNAMIC MODEL CREATION AND RESULTS

This section details the development of a dynamic model in MATLAB, and concludes with results that show the evolution of a low-altitude lunar orbit over an extended period of time and the effects of using a large number of terms from the gravity model.

For the purposes of integrating Equations (3.27-3.32), a MATLAB ode integrator is utilized. In particular, the "ode113" integrator is used, which is a variable order Adams-Bashforth-Moulton PECE solver [39]. The inputs that the integrator requires are an initial state vector and the desired timespan. The user specifies the initial orbital elements, and the elements are then sent through a subroutine that converts them to Cartesian coordinates. This conversion process from orbital elements to Cartesian coordinates is described in Appendix A. It is also possible to specify the error tolerances for the integrator. For this work, the absolute and relative error tolerances are both set to $1x10^{-14}$.

After all of the inputs for the integrator are set, the integration is performed with the output selected as the state vector across the desired timespan. However, the integration is performed in coordinates with respect to the rotating selenographic frame

while it is desired to plot the results with respect to an inertial frame. Therefore, after the integration is completed the states are converted to an inertial frame. This conversion is detailed in Appendix B.

With the dynamic model created, the results can be analyzed in order to observe the long term behavior of the lunar orbits. It should be noted that the only variables that will affect the structure of the resultant orbit are the initial orbital elements and the order and degree of the gravity model that will be used, i.e. l_{max} and m_{max}. The constraint on the l_{max} and m_{max} variables is that neither can be larger than 165, as the lunar gravity model used for this work is of degree and order 165x165. The integrator timespan specifies the time length over which the results are presented, and does not affect that actual structure of the orbit. For most of the graphs presented in this section, the timespan is held constant.

It was found that the length of computer running time is directly related to the size of the l_{max} and m_{max} variables, so an analysis was made to see if sufficient accuracy can still be obtained by using a small fraction of the lunar gravity model. This involved a case study where a set of initial orbital elements is fixed, and integrations are performed with different values for l_{max} and m_{max}. The six initial orbital elements used for this case study are presented in Table 1.1. These initial orbital elements were chosen to specify a 100 km, nearly circular, polar orbit. The values for the ascending node, argument of periapsis, and true anomaly were chosen arbitrarily.

Table 1.1. Initial Orbital Elements for Dynamic Model Simulations

Orbital Parameter	*Value*
Semimajor axis, a_i	1837.4 km
Eccentricity, e_i	0.0013
Inclination, i_i	90°
Ascending Node, Ω_i	45°
Argument of Periapsis, ω_i	45°
True Anomaly, ν_i	0°

Graphs were created using the initial orbital elements defined in Table 1.1 and a constant timespan of 20 days for various values of l_{max} and m_{max}, and are presented as Figures 3.5-3.9.

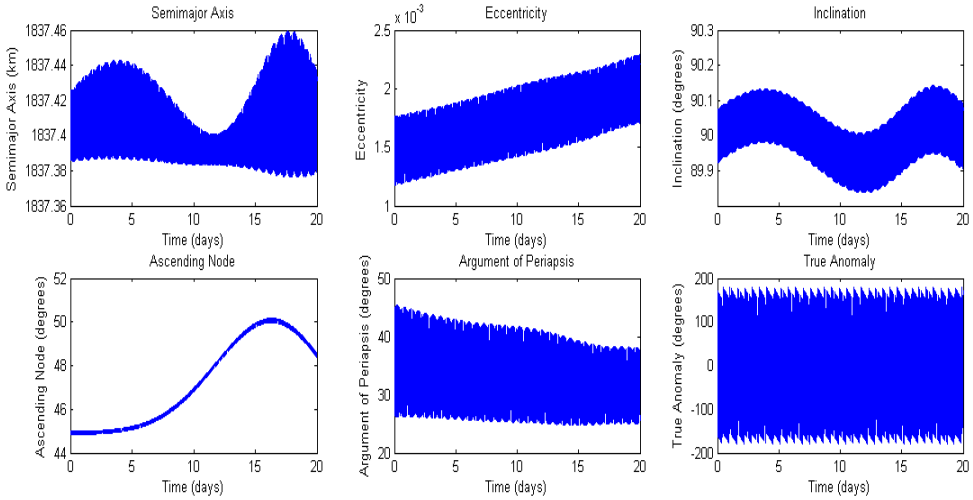

Figure 3.5. 20-Day Orbit for $l_{max} = 2$, $m_{max} = 0$

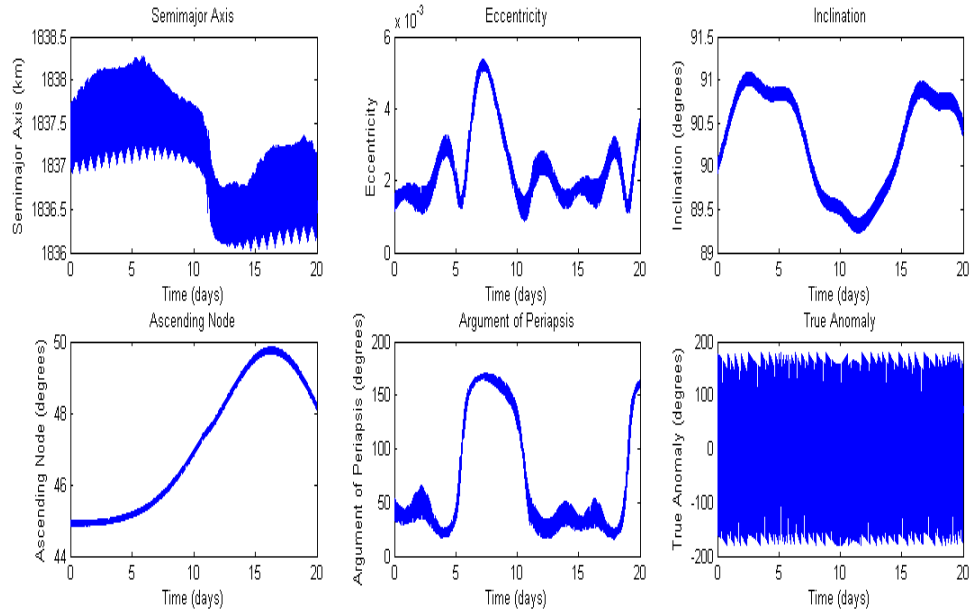

Figure 3.6. 20-Day Orbit for $l_{max} = 10$, $m_{max} = 10$

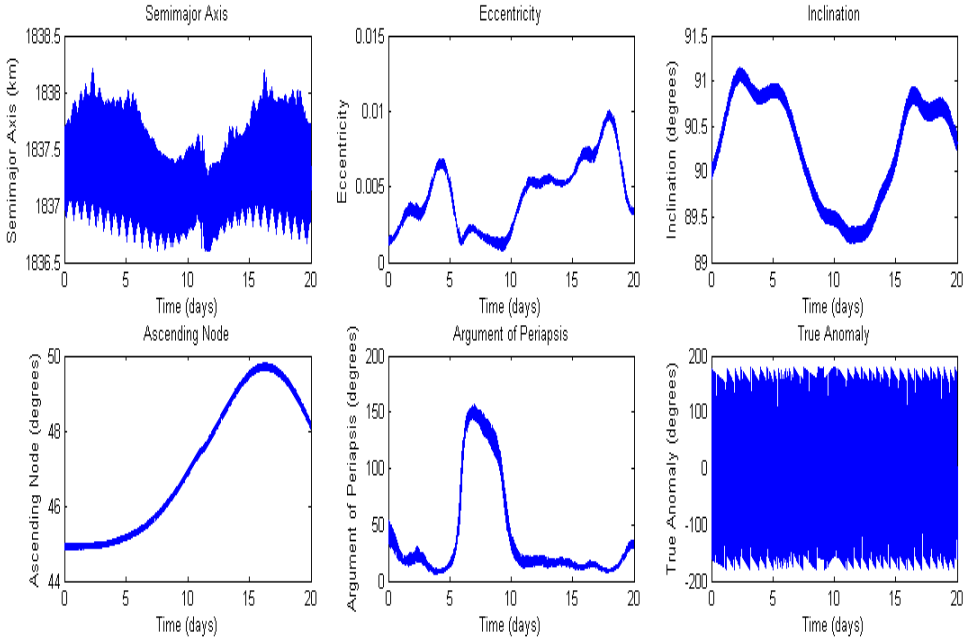

Figure 3.7. 20-Day Orbit for $l_{max} = 20$, $m_{max} = 20$

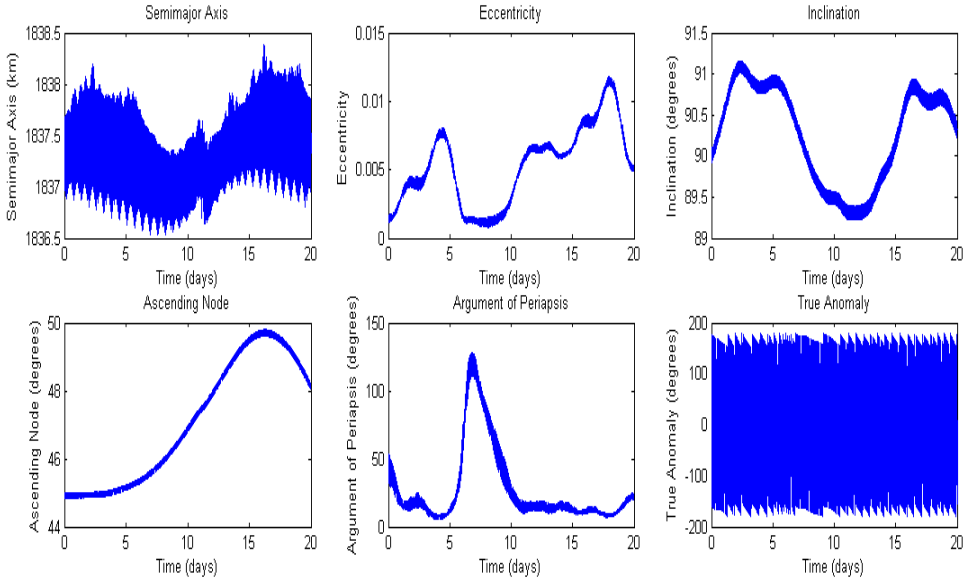

Figure 3.8. 20-Day Orbit for $l_{max} = 25$, $m_{max} = 25$

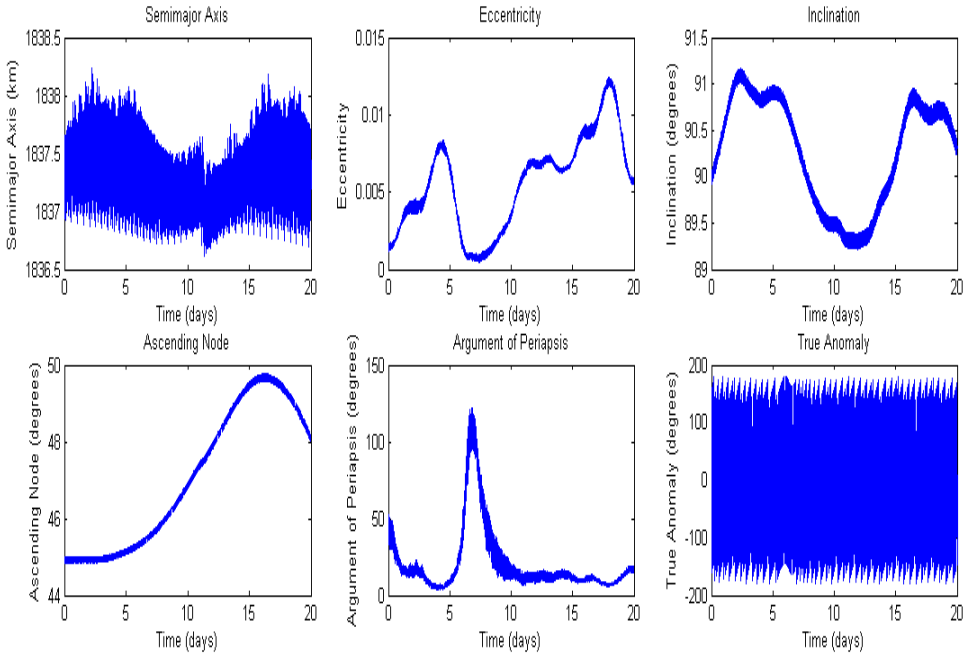

Figure 3.9. 20-Day Orbit for l_{max} = 50, m_{max} = 50

Figures 3.5-3.9 show the large impact of the lunar gravity field on a lunar orbiter. It can be seen from the plots that while the trajectories of a majority of the orbital elements are directly affected by the higher order terms in the lunar gravity model, the ascending node appears to be unaffected. Also, investigation of the plots shows that using further terms beyond 25x25 has a very minimal effect on the results. Because of this, it was decided to only use the gravity model terms up to 25x25 for the remainder of the analyses in this work. Doing so saves a tremendous amount of computing time while maintaining accurate results.

In order to get an indication of the long-term behavior of the solutions, a 105-day integration was performed using the same initial orbital elements defined above and using up to 25x25 in the lunar gravity model. This plot can be found in Figure 3.10. Also, it was desired to see how close the spacecraft will get to the Moon during this simulation. For this reason, a plot was also made of the periapsis evolution, which can be found in Figure 3.11.

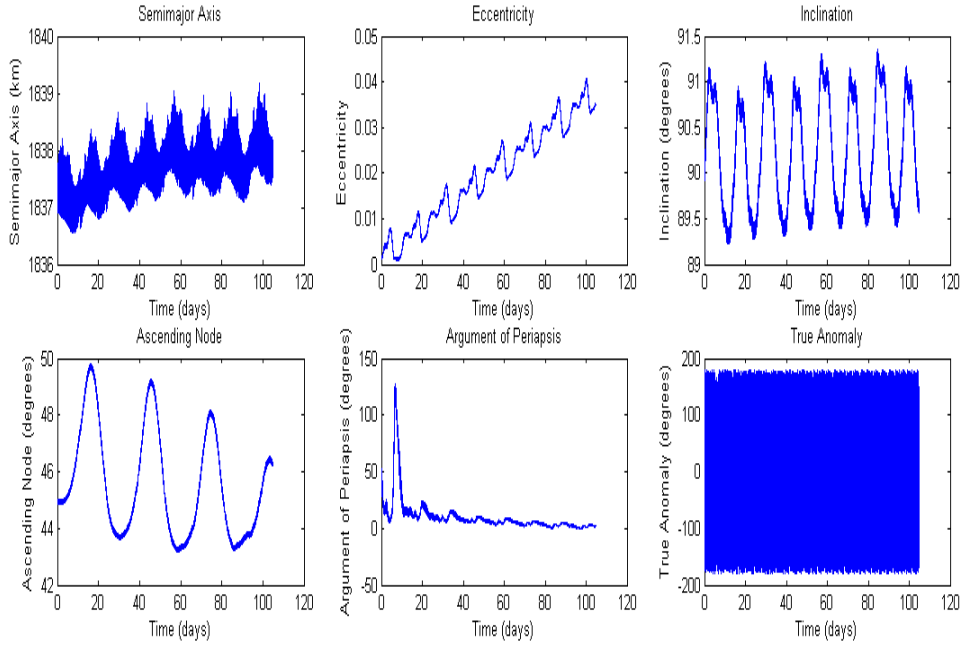

Figure 3.10. Orbital Element Trajectories for 105-Day integration

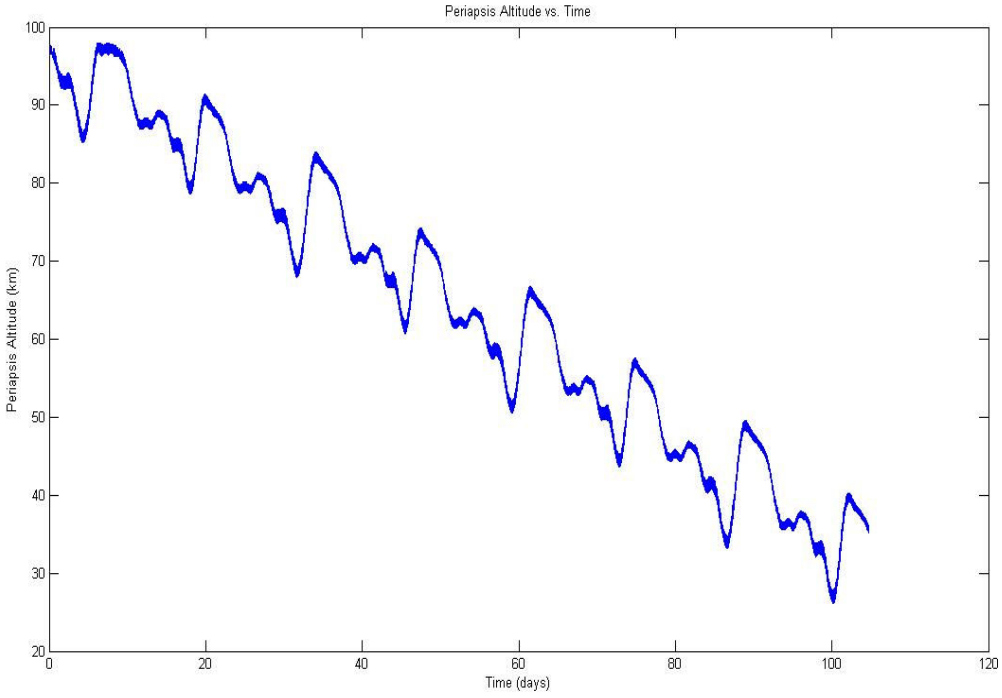

Figure 3.11. Periapsis Altitude Evolution for 105-Day Integration

Figure 3.10 shows that in the long-term, a low-altitude lunar orbit will experience drifts in semimajor axis and eccentricity which will eventually need to be corrected depending on how long it is desired for the satellite to remain in orbit. This drift occurs primarily because of the effects of the highly nonspherical lunar gravity field. It can also be seen from Figure 3.10 that the ascending node and inclination both stay in roughly the same region, performing oscillations of similar amplitudes.

Figure 3.11 shows another interesting result of the higher order lunar gravity terms. In particular, it can be seen that in 105 days the periapsis altitude decreases by approximately 70 km. Since the periapsis is the closest point on the orbit to the lunar surface, this gives an indication of the risk of the crashing into the surface. This decrease in altitude is caused by the drift in the semi-major axis and eccentricity seen in Figure 3.10, and it can clearly be assumed that without performing altitude control the spacecraft will eventually crash.

4. OPTIMAL CONTROL ANALYSIS

This section discusses optimal control theory and its application to the low-thrust control of a lunar orbiter. The section begins with an introduction to optimal control theory, and then leads into the method chosen for solving the two-point boundary value problem, the selection of the desired cost function, and the evaluation of the necessary conditions for optimality.

4.1. INTRODUCTION TO OPTIMAL CONTROL THEORY

The discipline of optimal control theory has been around for a relatively long time, with its origins emerging in the 1940's. Optimal control has roots in electrical engineering, with engineers first using it to design electromechanical apparatus that were efficiently self-correcting relative to some target objective. Since its creation, much work has been performed on improving optimal control solution techniques, and it is now an often used method of control.

Solving optimal control problems requires the use of calculus of variations. A good reference for information on calculus of variations is [40]. The general optimal control problem involves finding a control input u(t) for a generally nonlinear system

$$\dot{x} = f(x,u,t),\ x(t_0)\ \text{given} \tag{4.1}$$

where x(t) and u(t) are vector functions of size n and m, respectively in order to minimize or maximize the performance index

$$J = \phi(x_{t_f},t_f) + \int_{t_0}^{t_f} L(x,u,t)dt \tag{4.2}$$

while satisfying the constraint

$$\psi(x_{t_f},\ t_f) = 0 \tag{4.3}$$

In Equation (4.2), $\phi(x_{t_f},\ t_f)$ is a weighting function on the final state and *L(x, u, t)* is a cost function to be minimized during the integration [41]. The final weighting function $\phi(x_{t_f},\ t_f)$ and the constraint $\psi(x_{t_f},\ t_f)$ should not be confused. $\phi(x_{t_f},\ t_f)$ is a function

of the final state that is desired to be small, but may not necessarily be zero. On the other hand, $\psi(x_{t_f}, t_f)$ is a function of the final state that is desired to be fixed at exactly zero.

The dynamics constraint $\dot{x} = f(x,u,t)$ and the constraint on the final state $\psi(x_{t_f}, t_f)$ can be adjoined to the performance index of Equation (4.2) with multiplier functions λ(t) and ν, respectively [41]. This leads to the modified performance index

$$J' = \phi(x(t_f),t_f) + \nu^T \psi(x(t_f),t_f) + \int_{t_0}^{t_f} \left[L(x,u,t) + \lambda^T(t)\{f(x,u,t) - \dot{x}\} \right] dt \tag{4.4}$$

To simplify Equation (4.4), define a scalar function *H* called the Hamiltonian as

$$H(x,u,t) = L(x,u,t) + \lambda^T(t) f(x,u,t) \tag{4.5}$$

Substituting Equation (4.5) into Equation (4.4) leads to

$$J' = \phi(x(t_f),t_f) + \nu^T \psi(x(t_f),t_f) + \int_{t_0}^{t_f} \{H(x,u,t) - \lambda^T(t)\dot{x}\} dt \tag{4.6}$$

The second term in the integral of Equation (4.6) can be integrated by parts, leading to

$$J' = \phi(x(t_f),t_f) + \nu^T \psi(x(t_f),t_f) - \lambda^T(t_f)x(t_f) + \lambda^T(t_0)x(t_0) + \int_{t_0}^{t_f} \{H(x,u,t) + \dot{\lambda}^T(t)x(t)\} dt \tag{4.7}$$

In order to find the minimum of *J'*, the variation in *J'* due to variations in the control vector *u*(t) for fixed times t_0 and t_f. According to Lagrange theory, the constrained minimum of *J* occurs at the unconstrained minimum of *J'*, which is achieved when $\delta J' = 0$ [42]. This means that the differential of *J'* must be calculated as

$$\delta J' = \left[\left(\frac{\partial \phi}{\partial x} + \nu^T \frac{\partial \psi}{\partial x} - \lambda^T \right) \delta x \right]_{t=t_f} + \left[\lambda^T \delta x \right]_{t=t_0} + \int_{t_0}^{t_f} \left[\left(\frac{\partial H}{\partial x} + \dot{\lambda}^T(t) \right) \delta x + \frac{\partial H}{\partial u} \delta u + \left(\frac{\partial H}{\partial \lambda} - \dot{x} \right) \delta \lambda \right] dt \tag{4.8}$$

Since it would be very difficult to calculate the variations in $\delta x(t)$ and $\delta\lambda(t)$ caused by a given $\delta u(t)$, the λ(t) multipliers are chosen to make the coefficients of $\delta x(t)$ and $\delta\lambda(t)$ in Equation (4.8) vanish [41]. This implies

$$\dot{x} = \frac{\partial H}{\partial \lambda} = f(x,u,t) \tag{4.9}$$

and that

$$\dot{\lambda}^T(t) = -\frac{\partial H}{\partial x} \tag{4.10}$$

with the boundary condition

$$\lambda^T(t_f) = \frac{\partial \phi}{\partial x(t_f)} + \nu^T \frac{\partial \psi}{\partial x(t_f)} \tag{4.11}$$

Equation (4.8) now becomes

$$\delta J' = \lambda^T(t_0)\partial x(t_0) + \int_{t_0}^{t_f} \frac{\partial H}{\partial u}\delta u dt \tag{4.12}$$

According to Lagrange theory, the constrained minimum of J occurs at the unconstrained minimum of J' [42]. For J' to be a minimum, $\delta J'$ must be equal to zero for an arbitrary $\delta u(t)$. As seen from Equation (4.12), this occurs only if

$$\frac{\partial H}{\partial u} = 0 \tag{4.13}$$

Taking the partial of H in Equation (4.12), it is found that

$$\frac{\partial H}{\partial u} = \left(\frac{\partial f}{\partial u}\right)^T \lambda + \left(\frac{\partial L}{\partial u}\right)^T = 0 \tag{4.14}$$

Equations (4.9), (4.10), (4.11) and (4.14) are the necessary conditions for a minimum of J, and all solutions to the necessary conditions will lead to stationary points of J. Therefore, the necessary conditions do not guarantee a minimum solution; the solution could actually be a minimum, a maximum, or a saddle point. In order to guarantee a minimum or maximum of J, the sufficient conditions for a minimum must be evaluated which involve evaluating the second derivatives of J. However, in this work only stationary points are studied.

In order to find the control vector function u(t) that provides a stationary value of J, the $2n$ differential equations, Equations (4.9) and (4.10) must be integrated from t_0 to t_f

while computing $u(t)$ from Equation (4.14). The boundary conditions for Equations (4.9) and (4.10) are $x(t_0)$ given and Equation (4.11). Also, it should be noted that the boundary conditions are split, with one set of boundary conditions being defined at t_0 and the other set being defined at t_f. This implies that the solution of the optimal control problem involves solving a two-point boundary value problem, which is typically very difficult to solve for nonlinear systems and requires using numerical methods.

The following chapter will discuss the differences between the types of methods used to solve optimal control problems, and detail the method chosen for this work.

4.2. SOLVING THE TWO-POINT BOUNDARY VALUE PROBLEM

Due in part to the fact that optimal control theory has been around for over forty years, much work has been done in generating methods and algorithms for solving optimal control problems. Reference [43] gives an excellent overview of many of the current methods in use. Of all the current methods available, most can be classified as one of two types: indirect and direct [43].

Indirect methods involve deriving the expressions for the necessary conditions for optimality and solving the associated two-point boundary value problem [43]. Commonly used indirect methods include backward sweep algorithms, indirect shooting methods, and indirect transcription methods. One rather serious drawback of indirect methods is that they require a very good guess for the initial costates in order to converge. However, if a sufficient initial guess is made, these methods typically benefit from quick convergence and a guaranteed optimal solution. Another drawback of indirect methods is that for complex systems, deriving expressions for the necessary conditions for optimality can be tedious.

Direct methods, on the other hand, solve the optimal control problem by adjusting the control variables at each iteration in an attempt to continually reduce the performance index. All direct methods introduce some parametric representation for the control variables. Some examples of direct methods used today include collocation [44] and direct transcription [43]. One immediate advantage of these methods is that they typically do not require deriving expressions for the necessary conditions for optimality, making these types of methods more appealing for complex systems. These methods also have a

much larger region of convergence than indirect methods, therefore they do not require as good of a guess for the initial costates. However, a handicap of direct methods is that they tend to take much longer to converge than indirect methods.

Both methods have their advantages and disadvantages, as summarized above. However, as stated above, if a good guess for the initial costates is available, indirect methods are the best choice due to their fast convergence compared to direct methods and the guarantee of an optimal solution. Testing was performed, which is explained in more detail in Section 5, and it was found that for the system used in this work if it is assumed that initially the states are on or near their nominal values, or in other words if it is assumed that negligible control accelerations are needed initially, then an initial guess of $\lambda(t_0)=0$ is a sufficient guess for convergence. Taking advantage of this, an indirect method was chosen.

The indirect method that was chosen is a Transition Matrix algorithm described in references [41] and [42]. This algorithm is based off of assuming a linear relationship between the initial and final costates, and finding a transition matrix that can be used to relate changes between them. For the simulations presented in this thesis, no weighting or constraints are placed on the final states, therefore Equation (4.11) reduces to

$$\lambda(t_f)=0 \tag{4.15}$$

Equation (4.15) is needed in the implementation of the Transition Matrix algorithm.

A step-by-step walkthrough of the algorithm is as follows:

- **Step 1:** Guess the *n* unspecified initial costates, $\lambda(t_0)$.
- **Step 2:** Numerically integrate Equations (4.9) and (4.10) forward from t_0 to t_f, using Equation (4.14) to determine the control vector u(t).
- **Step 3:** Record $\lambda_1(t_f)$, $\lambda_2(t_f)$, …… $\lambda_n(t_f)$.
- **Step 4:** Determine the (*n* x *n*) transition matrix $\left[\frac{\partial\mu(t_f)}{\partial\lambda_{t_0}}\right]$. This matrix is found through a finite differencing method by performing *n* additional integrations of Equations (4.9) and (4.10), where in each of the integrations one of the $\lambda_i(t_0)$ values is changed by a small amount. After each of the integrations, the

quantities $\delta\mu(t_f)$ are calculated as the difference between the final costates achieved and the values recorded in Step 3

$$\delta\mu(t_f) = \begin{bmatrix} \delta\lambda_1(t_f) \\ . \\ . \\ . \\ \delta\lambda_n(t_f) \end{bmatrix} \tag{4.16}$$

and then are divided by $\delta\lambda_i(t_0)$. Each $\delta\mu(t_f)$ vector makes up one column of the total $\left[\frac{\partial\mu(t_f)}{\partial\lambda_{t_0}}\right]$ matrix.

- **Step 5:** Choose another $\delta\mu(t_f)$ vector which will bring the next solution closer to the desired final costate values. This $\delta\mu(t_f)$ vector is found by comparing the final costates recorded in Step 3 with the desired values specified by Equation (4.15).
- **Step 6:** With the $\delta\mu(t_f)$ vector computed in Step 5, invert the transition matrix from Step 4 to find $\delta\lambda(t_0)$:

$$\delta\lambda(t_0) = \left[\frac{\partial\mu(t_f)}{\partial\lambda(t_0)}\right]^{-1} \delta\mu(t_f) \tag{4.17}$$

- **Step 7:** Calculate the corrected initial costates as

$$\lambda(t_0)_{new} = \lambda(t_0)_{old} + \delta\lambda(t_0) \tag{4.18}$$

and then repeats Steps 1-6 until the required $\delta\lambda(t_0)$ is sufficiently small.

In most of the simulations performed in this thesis, the above algorithm converges to the optimal trajectory within only three to four iterations. While the algorithm has proven to be very useful, it should be noted that due to the linearity assumption inherent to use of the transition matrix, the algorithm may not necessarily be as efficient when trying to control a different system under different constraints. The requirement that no large control accelerations are needed initially is also a handicap, as it leads to a lack of

robustness for the controller. For these reasons, future efforts with this work will involve studying the use of direct optimal control methods.

4.3. COST FUNCTION SELECTION

The selection of the *L(x,u,t)* cost function to be used in the performance index defined by Equation (4.2) will typically depend directly on the requirements of the particular mission being analyzed. In this work, the following objectives are prescribed:

- Maintain a polar orbit
- Maintain a Sun-synchronous orbit by forcing the ascending node to rotate at the rate of 0.9856 °/day
- Minimize the total amount of thrust acceleration required

From the above objectives, it is evident that the cost function will need to have terms relating to inclination, ascending node, and the control accelerations. Taking this into account, a cost function was chosen as

$$L(x,u,t) = w_1 \cos^2(i) + w_2\left[\cos\left(\Omega_R(t)\right) - \cos\left(\Omega_{t_0} + \dot{\Omega}_{sunsynch}(t-t_0) - \omega_m(t-t_0)\right)\right]^2 + w_3\left(u_1{}^2 + u_2{}^2 + u_3\right)^2 \tag{4.19}$$

In Equation (4.19), $\Omega_R(t)$ is the ascending node with respect to the rotating frame, Ω_{t_0} is the initial ascending node, and $\dot{\Omega}_{sunsynch}$ is the desired Sun-synchronous rate of 0.9856 °/day. Also, the variables w_1, w_2, and w_3 are weights which can be defined by the user in order to stress the minimization of one element of the cost function over another.

By minimizing the first term of Equation (4.19), the inclination *i* is kept close to 90°. The second term involves minimizing the difference between the actual ascending node and the desired Sun-synchronous ascending node. It should be noted that the $\omega_{moon}t$ term accounts for the fact that the ascending node is measured with respect to a rotating frame rather than an inertial frame. Finally, the squared control terms in Equation (4.19) indicate that the total energy is to be minimized. It should also be noted that all of the terms in Equation (4.19) are squared in order to satisfy the requirement that *L(x,u,t)* must be positive definite in order for a minimum to exist.

In order to use the above cost function with the dynamics described in Section 3, the first two terms of Equation (4.19) will need to be converted into a Cartesian form.

The conversion of each of these terms into Cartesian coordinates is described in the remainder of this section, beginning with the $\cos^2(i)$ term.

The inclination *i* is defined as

$$i = \cos^{-1}\left(\frac{h_z}{|\boldsymbol{h}|}\right) \tag{4.20}$$

where $\boldsymbol{h}$ is the angular momentum vector

$$\boldsymbol{h} = \boldsymbol{r} \times \boldsymbol{V} = (y\dot{z} - z\dot{y})\hat{\boldsymbol{x}} + (z\dot{x} - x\dot{z})\hat{\boldsymbol{y}} + (x\dot{y} - y\dot{x})\hat{\boldsymbol{z}} \tag{4.21}$$

and h_z is the $\hat{z}$ component of the angular momentum vector

$$h_z = x\dot{y} - y\dot{x} \tag{4.22}$$

It can be seen from Equation (4.20) that

$$\cos(i) = \frac{h_z}{|\boldsymbol{h}|} \tag{4.23}$$

Substituting Equations (4.21) and (4.22) into Equation (4.23), taking the square, and using the state space format defined in Section 3 leads to

$$\cos^2(i) = \frac{(x_1x_5 - x_2x_4)^2}{(x_2x_6 - x_3x_5)^2 + (x_3x_4 - x_1x_6)^2 + (x_1x_5 - x_2x_4)^2} \tag{4.24}$$

With $\cos^2(i)$ expressed in terms of the state space coordinates defined in Section 3, the next step is to perform the same conversion for the second term of Equation (4.19). Begin by calculating the node vector $\vec{n}$, which is the vector from the origin of the coordinate frame to the ascending node of the orbit. This vector is defined as

$$\boldsymbol{n} = \hat{\boldsymbol{z}} \times \frac{\boldsymbol{h}}{|\boldsymbol{h}|} \tag{4.25}$$

Carrying out the cross product in Equation (4.25) leads to

$$\boldsymbol{n} = \frac{-h_y}{|\boldsymbol{h}|}\hat{\boldsymbol{x}} + \frac{h_x}{|\boldsymbol{h}|}\hat{\boldsymbol{y}} \tag{4.26}$$

Now, the cosine of the ascending node, $\cos(\Omega_{\boldsymbol{R}})$, is defined as

$$\cos(\Omega_R) = \frac{\hat{\boldsymbol{x}} \cdot \boldsymbol{n}}{|\boldsymbol{n}|} \tag{4.27}$$

Substituting Equation (4.26) into Equation (4.27) leads to

$$\cos(\Omega_R) = \frac{\dfrac{-h_y}{|\boldsymbol{h}|}}{\dfrac{\sqrt{h_x^2 + h_y^2}}{|\boldsymbol{h}|}} = \frac{-h_y}{\sqrt{h_x^2 + h_y^2}} \tag{4.28}$$

Noting the definition of the angular momentum components from Equation (4.20) and substituting the appropriate components into Equation (4.28), the equation for $\cos(\Omega_R)$ in terms of the state space variables is obtained as

$$\cos(\Omega_R) = \frac{x_1 x_6 - x_4 x_3}{\sqrt{(x_2 x_6 - x_3 x_5)^2 + (x_4 x_3 - x_6 x_1)^2}} \tag{4.29}$$

With Equations (4.24) and (4.29) in hand, they can be substituted into Equation (4.19) in order to obtain a cost function that is represented in terms of state space variables. This representation for the cost function is found as

$$\begin{aligned} L(x,u,t) = {} & w_1\left[\frac{(x_1 x_5 - x_2 x_4)^2}{(x_2 x_6 - x_3 x_5)^2 + (x_3 x_4 - x_1 x_6)^2 + (x_1 x_5 - x_2 x_4)^2}\right] + \\ & w_2\left[\frac{x_1 x_6 - x_4 x_3}{\sqrt{(x_2 x_6 - x_3 x_5)^2 + (x_4 x_3 - x_6 x_1)^2}} - \cos\left(\Omega_{t_0} + \dot{\Omega}_{sunsynch}(t - t_0) - \omega_m(t - t_0)\right)\right]^2 + \\ & w_3\left(u_1^2 + u_2^2 + u_3^2\right) \end{aligned} \tag{4.30}$$

It should be noted that the $\cos\left(\Omega_{t_0} + \dot{\Omega}_{sunsynch}(t - t_0) - \omega_m(t - t_0)\right)$ term is left in its original form because it is a function of time only, and not the states.

4.4. DERIVATION OF NECESSARY CONDITIONS FOR OPTIMALITY

With the cost function generated in the previous section and the system dynamics described in Section 3, it is now possible to evaluate the necessary conditions for optimality for this system. These conditions are defined by Equations (4.9), (4.10), (4.11), and (4.14). As explained in Section 4.1, the necessary conditions for optimality guarantee a stationary point for the performance index used in this work

$$J = \int_{t_0}^{t_f} L(x,u,t) \tag{4.31}$$

but do not guarantee a minimum.

The first condition, Equation (4.9), simplifies to Equations (3.27-3.32), the equations of motion for the system. This specifies six differential equations with the boundary condition of $x(t_0)$ given.

The second condition is Equation (4.10), which specifies the differential equations for the six costates. Carrying out the partial derivative in Equation (4.10) leads to

$$\dot{\lambda} = -\frac{\partial f(x,u,t)}{\partial x}^T \lambda - \frac{\partial L(x,u,t)}{\partial x}^T \tag{4.32}$$

It is evident that in order to utilize Equation (4.32) the partials $\frac{\partial f(x,u,t)}{\partial x}$ and $\frac{\partial L(x,u,t)}{\partial x}$ must be calculated.

The first partial in Equation (4.32), $\frac{\partial f(x,u,t)}{\partial x}$, is obtained by taking the partials of Equations (3.27-3.32) with respect to the six state variables. The physical significance of this matrix is that it indicates the change to the state dynamics that occurs from a small change in one of the states. The $\frac{\partial f(x,u,t)}{\partial x}$ matrix is a 6x6 matrix of the form

$$\frac{\partial f(x,u,t)}{\partial x}=\begin{bmatrix} \frac{\partial f_1(x,u,t)}{\partial x_1} & \frac{\partial f_1(x,u,t)}{\partial x_2} & \cdots & \frac{\partial f_1(x,u,t)}{\partial x_6} \\ \frac{\partial f_2(x,u,t)}{\partial x_1} & \frac{\partial f_2(x,u,t)}{\partial x_2} & \cdots & \vdots \\ \vdots & \vdots & \cdots & \vdots \\ \vdots & \vdots & \cdots & \vdots \\ \vdots & \vdots & \cdots & \vdots \\ \frac{\partial f_6(x,u,t)}{\partial x_1} & \vdots & \cdots & \frac{\partial f_6(x,u,t)}{\partial x_6} \end{bmatrix} \tag{4.33}$$

The individual terms of the matrix in Equation (4.32) are

$$\frac{\partial f_1}{\partial x_1}=0,\ \frac{\partial f_1}{\partial x_2}=0,\ \frac{\partial f_1}{\partial x_3}=0,\ \frac{\partial f_1}{\partial x_4}=1,\ \frac{\partial f_1}{\partial x_5}=0,\ \frac{\partial f_1}{\partial x_6}=0 \qquad \text{(4.34 a, b, c, d, e, f)}$$

$$\frac{\partial f_2}{\partial x_1}=0,\ \frac{\partial f_2}{\partial x_2}=0,\ \frac{\partial f_2}{\partial x_3}=0,\ \frac{\partial f_2}{\partial x_4}=0,\ \frac{\partial f_2}{\partial x_5}=1,\ \frac{\partial f_2}{\partial x_6}=0 \qquad \text{(4.35 a, b, c, d, e, f)}$$

$$\frac{\partial f_3}{\partial x_1}=0,\ \frac{\partial f_3}{\partial x_2}=0,\ \frac{\partial f_3}{\partial x_3}=0,\ \frac{\partial f_3}{\partial x_4}=0,\ \frac{\partial f_3}{\partial x_5}=0,\ \frac{\partial f_3}{\partial x_6}=1 \qquad \text{(4.36 a, b, c, d, e, f)}$$

$$\frac{\partial f_4}{\partial x_1}=\omega_m^2-\frac{\mu_{earth}}{\left|\boldsymbol{r}_{\boldsymbol{earth-sc}}\right|^3}+3\mu_{earth}\frac{r_{earth-sc_x}^2}{\left|\boldsymbol{r}_{\boldsymbol{earth-sc}}\right|^5}-\frac{\mu_{sun}}{\left|\boldsymbol{r}_{\boldsymbol{sun-sc}}\right|^3}+3\mu_{sun}\frac{r_{sun-sc_x}^2}{\left|\boldsymbol{r}_{\boldsymbol{sun-sc}}\right|^5}-\frac{\mu_{moon}}{\left|\boldsymbol{r}_{\boldsymbol{moon-sc}}\right|^3}+3\mu_{moon}\frac{x_1^2}{\left|\boldsymbol{r}_{\boldsymbol{moon-sc}}\right|^5} \tag{4.37a}$$

$$\frac{\partial f_4}{\partial x_2}=3\mu_{earth}\frac{r_{earth-sc_x}r_{earth-sc_y}}{\left|\boldsymbol{r}_{\boldsymbol{earth-sc}}\right|^5}+3\mu_{sun}\frac{r_{sun-sc_x}r_{sun-sc_y}}{\left|\boldsymbol{r}_{\boldsymbol{sun-sc}}\right|5}+3\mu_{moon}\frac{x_1x_2}{\left|\boldsymbol{r}_{\boldsymbol{moon-sc}}\right|^5} \qquad \text{(4.37 b)}$$

$$\frac{\partial f_4}{\partial x_3}=3\mu_{earth}\frac{r_{earth-sc_x}r_{earth-sc_z}}{\left|\boldsymbol{r}_{\boldsymbol{earth-sc}}\right|^5}+3\mu_{sun}\frac{r_{sun-sc_x}r_{sun-sc_z}}{\left|\boldsymbol{r}_{\boldsymbol{sun-sc}}\right|^5}+3\mu_{moon}\frac{x_1x_3}{\left|\boldsymbol{r}_{\boldsymbol{moon-sc}}\right|^5} \qquad \text{(4.37 c)}$$

$$\frac{\partial f_4}{\partial x_4}=0,\ \frac{\partial f_4}{\partial x_5}=2\omega_m,\ \frac{\partial f_4}{\partial x_6}=0 \qquad \text{(4.37 d, e, f)}$$

$$\frac{\partial f_5}{\partial x_1}=3\mu_{earth}\frac{r_{earth-sc_x}r_{earth-sc_y}}{\left|\boldsymbol{r}_{\boldsymbol{earth-sc}}\right|^5}+3\mu_{sun}\frac{r_{sun-sc_x}r_{sun-sc_y}}{\left|\boldsymbol{r}_{\boldsymbol{sun-sc}}\right|^5}+3\mu_{moon}\frac{x_1x_2}{\left|\boldsymbol{r}_{\boldsymbol{moon-sc}}\right|^5} \qquad \text{(4.38 a)}$$

$$\frac{\partial f_5}{\partial x_2} = \omega_m^2 - \frac{\mu_{earth}}{\left|\boldsymbol{r}_{\boldsymbol{earth-sc}}\right|^3} + 3\mu_{earth}\frac{r_{earth-sc_y}^2}{\left|\boldsymbol{r}_{\boldsymbol{earth-sc}}\right|^5} - \frac{\mu_{sun}}{\left|\boldsymbol{r}_{\boldsymbol{sun-sc}}\right|^3} + 3\mu_{sun}\frac{r_{sun-sc_y}^2}{\left|\boldsymbol{r}_{\boldsymbol{sun-sc}}\right|^5} - \frac{\mu_{moon}}{\left|\boldsymbol{r}_{\boldsymbol{moon-sc}}\right|^3} + 3\mu_{moon}\frac{x_2^2}{\left|\boldsymbol{r}_{\boldsymbol{moon-sc}}\right|^5} \quad (4.38\text{ b})$$

$$\frac{\partial f_5}{\partial x_3} = 3\mu_{earth}\frac{r_{earth-sc_y}r_{earth-sc_z}}{\left|\boldsymbol{r}_{\boldsymbol{earth-sc}}\right|^5} + 3\mu_{sun}\frac{r_{sun-sc_y}r_{sun-sc_z}}{\left|\boldsymbol{r}_{\boldsymbol{sun-sc}}\right|^5} + 3\mu_{moon}\frac{x_2x_3}{\left|\boldsymbol{r}_{\boldsymbol{moon-sc}}\right|^5} \quad (4.38\text{ c})$$

$$\frac{\partial f_5}{\partial x_4} = -2\omega_m\,,\ \frac{\partial f_5}{\partial x_5} = 0\,,\ \frac{\partial f_5}{\partial x_6} = 0 \quad (4.38\text{ d, e, f})$$

$$\frac{\partial f_6}{\partial x_1} = 3\mu_{earth}\frac{r_{earth-sc_x}r_{earth-sc_z}}{\left|\boldsymbol{r}_{\boldsymbol{earth-sc}}\right|^5} + 3\mu_{sun}\frac{r_{sun-sc_x}r_{sun-sc_z}}{\left|\boldsymbol{r}_{\boldsymbol{sun-sc}}\right|^5} + 3\mu_{moon}\frac{x_1x_3}{\left|\boldsymbol{r}_{\boldsymbol{moon-sc}}\right|^5} \quad (4.39\text{ a})$$

$$\frac{\partial f_6}{\partial x_2} = 3\mu_{earth}\frac{r_{earth-sc_y}r_{earth-sc_z}}{\left|\boldsymbol{r}_{\boldsymbol{earth-sc}}\right|^5} + 3\mu_{sun}\frac{r_{sun-sc_y}r_{sun-sc_z}}{\left|\boldsymbol{r}_{\boldsymbol{sun-sc}}\right|^5} + 3\mu_{moon}\frac{x_2x_3}{\left|\boldsymbol{r}_{\boldsymbol{moon-sc}}\right|^5} \quad (4.39\text{ b})$$

$$\frac{\partial f_6}{\partial x_3} = -\frac{\mu r_{earth}}{\left|\boldsymbol{r}_{\boldsymbol{earth-sc}}\right|^3} + 3\mu_{earth}\frac{r_{earth-sc_z}^2}{\left|\boldsymbol{r}_{\boldsymbol{earth-sc}}\right|^5} - \frac{\mu_{sun}}{\left|\boldsymbol{r}_{\boldsymbol{sun-sc}}\right|^3} + 3\mu_{sun}\frac{r_{sun-sc_z}^2}{\left|\boldsymbol{r}_{\boldsymbol{sun-sc}}\right|^5} - \frac{\mu_{moon}}{\left|\boldsymbol{r}_{\boldsymbol{moon-sc}}\right|^3} + 3\mu_{moon}\frac{x_3^2}{\left|\boldsymbol{r}_{\boldsymbol{moon-sc}}\right|^5} \quad (4.39\text{ c})$$

$$\frac{\partial f_6}{\partial x_4} = 0\,,\ \frac{\partial f_6}{\partial x_5} = 0\,,\ \frac{\partial f_6}{\partial x_6} = 0 \quad (4.39\text{ d, e, f})$$

The second partial derivative in Equation (4.32) is $\frac{\partial L(x,u,t)}{\partial x}$. This partial derivative vector is found by taking the partials of Equation (4.30) with respect to the six state variables and is in the form of

$$\frac{\partial L(x,u,t)}{\partial x} = \left[\frac{\partial L(x,u,t)}{\partial x_1}\quad \frac{\partial L(x,u,t)}{\partial x_2}\quad \frac{\partial L(x,u,t)}{\partial x_3}\quad \frac{\partial L(x,u,t)}{\partial x_4}\quad \frac{\partial L(x,u,t)}{\partial x_5}\quad \frac{\partial L(x,u,t)}{\partial x_6}\right] \quad (4.40)$$

Physically, the $\frac{\partial L(x,u,t)}{\partial x}$ vector indicates the sensitivity of the cost function to a small change in the state variables.

Before solving for the individual terms in Equation (4.40), the following auxiliary variables are defined:

$$A = h_x = x_2 x_6 - x_3 x_5 \tag{4.41}$$

$$B = h_y = x_3 x_4 - x_1 x_6 \tag{4.42}$$

$$C = h_z = x_1 x_5 - x_2 x_4 \tag{4.43}$$

$$D = A^2 + B^2 + C^2 \tag{4.44}$$

$$E = A^2 + B^2 \tag{4.45}$$

$$\beta = \Omega_{t_0} + \dot{\Omega}_{sunsynch}(t - t_0) - \omega_m (t - t_0) \tag{4.46}$$

In terms of the auxiliary variables, the cost function in Equation (4.30) becomes

$$L(x,u,t) = w_1 \left[\frac{C^2}{D} \right] + w_2 \left[\frac{-B}{\sqrt{E}} - \cos(\beta) \right]^2 + w_3 \left[u_1^2 + u_2^2 + u_3^2 \right] \tag{4.47}$$

and the six partial derivatives required for Equation (4.40) are

$$\frac{\partial L(x,u,t)}{\partial x_1} = w_1 \left[\frac{2Cx_5}{D} - \frac{C^2(-2Bx_6 + 2Cx_5)}{D^2} \right] + 2w_2 \left[\frac{-B}{\sqrt{E}} - \cos(\beta) \right] \left[\frac{x_6}{\sqrt{E}} - \frac{B^2 x_6}{E^{1.5}} \right] \tag{4.48}$$

$$\frac{\partial L(x,u,t)}{\partial x_2} = w_1 \left[\frac{-2Cx_4}{D} - \frac{C^2(2Ax_6 - 2Cx_4)}{D^2} \right] + 2w_2 \left[\frac{-B}{\sqrt{E}} - \cos(\beta) \right] \left[\frac{ABx_6}{E^{1.5}} \right] \tag{4.49}$$

$$\frac{\partial L(x,u,t)}{\partial x_3} = w_1 \left[-\frac{C^2(-2Ax_5 + 2Bx_4)}{D^2} \right] + 2w_2 \left[\frac{-B}{\sqrt{E}} - \cos(\beta) \right] \left[\frac{-x_4}{\sqrt{E}} + \frac{B(-Ax_5 + Bx_4)}{E^{1.5}} \right] \tag{4.50}$$

$$\frac{\partial L(x,u,t)}{\partial x_4} = w_1 \left[\frac{-2Cx_2}{D} - \frac{C^2(2Bx_3 - 2Cx_2)}{D^2} \right] + 2w_2 \left[\frac{-B}{\sqrt{E}} - \cos(\beta) \right] \left[\frac{-x_3}{\sqrt{E}} + \frac{B^2 x_3}{E^{1.5}} \right] \tag{4.51}$$

$$\frac{\partial L(x,u,t)}{\partial x_5} = w_1 \left[\frac{2Cx_1}{D} - \frac{C^2(-2Ax_3 + 2Cx_1)}{D^2} \right] + 2w_2 \left[\frac{-B}{\sqrt{E}} - \cos(\beta) \right] \left[\frac{-ABx_3}{E^{1.5}} \right] \tag{4.52}$$

$$\frac{\partial L(x,u,t)}{\partial x_6} = w_1 \left[-\frac{C^2(2Ax_2 - 2Bx_1)}{D^2} \right] + 2w_2 \left[\frac{-B}{\sqrt{E}} - \cos(\beta) \right] \left[\frac{x_1}{\sqrt{E}} + \frac{B(Ax_2 - Bx_1)}{E^{1.5}} \right] \tag{4.53}$$

Equation (4.32) specifies six first order differential equations for the costates. The boundary condition for these differential equations comes from the third necessary condition for optimality, Equation (4.11). As explained in Section 4.2, since no weights or constraints are being placed on the final states, Equation (4.11) becomes

$$\lambda(t_f) = 0 \tag{4.54}$$

The final necessary condition for optimality is Equation (4.14). This condition is called the stationarity condition, and it states that the optimal control input will lead to a stationary value of the Hamiltonian, *H*. The usefulness of Equation (4.14) is that it can be used to solve for the optimal control input.

As seen from Equation (4.14), the matrices $\frac{\partial f(x,u,t)}{\partial u}$ and $\frac{\partial L(x,u,t)}{\partial u}$ must be found. By taking partial derivatives with respect to the three control inputs u_1, u_2, and u_3, these matrices are found as

$$\frac{\partial f(x,u,t)}{\partial u} = \begin{bmatrix} 0 & 0 & 0 \\ 0 & 0 & 0 \\ 0 & 0 & 0 \\ 1 & 0 & 0 \\ 0 & 1 & 0 \\ 0 & 0 & 1 \end{bmatrix} \tag{4.55}$$

and

$$\frac{\partial L(x,u,t)}{\partial u} = \begin{bmatrix} 2w_3u_1 & 2w_3u_2 & 2w_3u_3 \end{bmatrix} \tag{4.56}$$

Substituting Equations (4.55) and (4.56) into Equation (4.14) leads to

$$\begin{bmatrix} 0 & 0 & 0 & 1 & 0 & 0 \\ 0 & 0 & 0 & 0 & 1 & 0 \\ 0 & 0 & 0 & 0 & 0 & 1 \end{bmatrix} \begin{bmatrix} \lambda_1 \\ \lambda_2 \\ \lambda_3 \\ \lambda_4 \\ \lambda_5 \\ \lambda_6 \end{bmatrix} + \begin{bmatrix} 2w_3u_1 \\ 2w_3u_2 \\ 2w_3u_3 \end{bmatrix} = 0 \tag{4.57}$$

Equation (4.57) can now be solved to obtain the equations for the three control inputs as

$$u_1 = -\frac{1}{2w_3}\lambda_4 \tag{4.58}$$

$$u_2 = -\frac{1}{2w_3}\lambda_5 \tag{4.59}$$

$$u_3 = -\frac{1}{2w_3}\lambda_6 \tag{4.60}$$

Equations (4.58-4.60) indicate that if the costates are known, the control inputs required for the equations of motion (Equations (3.27-3.32)) can easily be found.

The result of the analysis in this section is twelve differential equations supplied by Equations (3.27-3.32) and Equation (4.32) with boundary conditions given by $x(t_0)$ given and Equation (4.54), where the three control inputs are found via Equations (4.58-4.60). It should be noted that the differential equations are highly nonlinear and also that the state and costate dynamics are interrelated. Because of this, the system is very sensitive to small changes in the unspecified boundary conditions. Since the boundary conditions for the differential equations are split, the method presented in Section 4.2 must be used in order to solve the system.

Incorporating the equations derived in this section with the dynamic model created in Section 3 allowed for a controller to be made in MATLAB. Called "Controller A", this controller is suitable for use when the initial states are very close to nominal values. A second controller was also created which is suitable for cases in which the initial states deviate from nominal values, and is described in the next section.

4.5. TERMINAL STATE CONTROLLER

The analysis outlined in the previous sections works well when the initial states are such that no large control accelerations are required to correct them. When this is the case, as explained in Section 4.2, a guess for the initial costates of $\lambda(t_0) = 0$ has been found to be very sufficient for convergent. However, when this is not the case, the methods described above are not sufficient. For example, the method described above would not be able to correct an initial inclination deviation of 5°. This section presents

another method that can be used in the cases where corrections are needed for the initial states.

The primary reason that the transition matrix algorithm outlined in Section 4.2 is not sufficient when the initial states need to be corrected is due to the fact that it requires a full integration over a specified timespan in order to correct the guess for the initial costates. When the initial states do not need to be corrected and a guess of $\lambda(t_0)=0$ is made for the costates, a stable trajectory is obtained which easily allows for the costates to be corrected. However, if the initial states are slightly off of their nominal values and need corrected, using a guess of $\lambda(t_0)=0$ will lead to a diverging trajectory. In such a scenario, the difference between the final costates produced by the integration and the desired final costates of $\lambda(t_f)=0$ is so large that a correction cannot be found. Therefore, in order for the transition matrix algorithm to be used for these cases, either a better guess for the initial costates must be found or simplifications must be made which will allow for a stable trajectory over the integration.

It was decided that when a situation arises where corrections are needed for the initial states, a controller is desired that will correct the initial states to their nominal values in a specified amount of time. Such a controller is often called a terminal state controller. After the states achieve their nominal values, a switch will be made to Controller A since at that point the method defined in the previous sections will be applicable. However, it should be noted that since a controller switch is made, the combined trajectories are no longer optimal but rather suboptimal.

If it is only desired to get the states from some point A to another point B in some time *t* with no restrictions on the path between the two points, certain simplifications can be made. Namely, the inclination and ascending node weights in the cost function of Equation (4.30), w_1 and w_2, can both be set to zero. Doing this states that the inclination and ascending node are allowed to attain any possible values along the path. With this simplification, it is easily seen that

$$\frac{\partial L(x,u,t)}{\partial x}=0 \tag{4.61}$$

Substitution of Equation (4.61) into the equation for the costate dynamics (Equation (4.32)) leads to

$$\dot{\lambda} = \left(\frac{\partial f(x,u,t)}{\partial x} \right)^T \lambda \tag{4.62}$$

It can be seen from Equation (4.62) that if the initial costates are set to zero, the costates will be equal to zero for any time $t > 0$. If the costates are zero then the control input is also zero via Equations (4.58-4.60), so a guess of $\lambda(t_0) = 0$ will lead to an uncontrolled trajectory. While this uncontrolled trajectory will have a deviation from the desired optimal trajectory, it will at least be a stable trajectory, which implies that a correction to the initial costates can be made.

Aside from a simplified set of dynamics for the costates (Equation 4.62), the only other difference between this terminal state controller and Controller A will be the terminal boundary conditions. While the terminal boundary condition for Controller A takes the form of Equation (4.54), the terminal boundary condition for this controller is in the form of $x(t_f)$ given. The $x(t_f)$ conditions specify a polar, Sun-synchronous orbit with a prescribed semimajor axis and eccentricity. Essentially, the six conditions of Equation (4.54) are traded with another set of conditions, $x(t_f)$ given, so that the problem still has twelve boundary conditions.

In summary, the terminal state controller, called "Controller B", consists of twelve differential equations (Equations (3.27-3.32) and Equation (4.62) with boundary conditions of $x(t_0)$ and $x(t_f)$ given, where the three control inputs are found through Equations (4.58-4.60). Using a guess of $\lambda(t_0) = 0$, the transition matrix algorithm described in Section 4.2 can be used to solve this system. Since the specified terminal boundary condition is in terms of the states rather than the costates, the $\delta\mu(t_f)$ vectors required in the algorithm are found by comparing the final values of the states rather than the costates, taking the form

$$\delta\mu(t_f) = \begin{bmatrix} \delta x_1(t_f) \\ \delta x_2(t_f) \\ \cdot \\ \cdot \\ \cdot \\ \delta x_6(t_f) \end{bmatrix} \tag{4.63}$$

To demonstrate the effectiveness of this method, Figure 4.1 shows the results of attempting to correct an initial inclination error of 15° in 144 minutes.

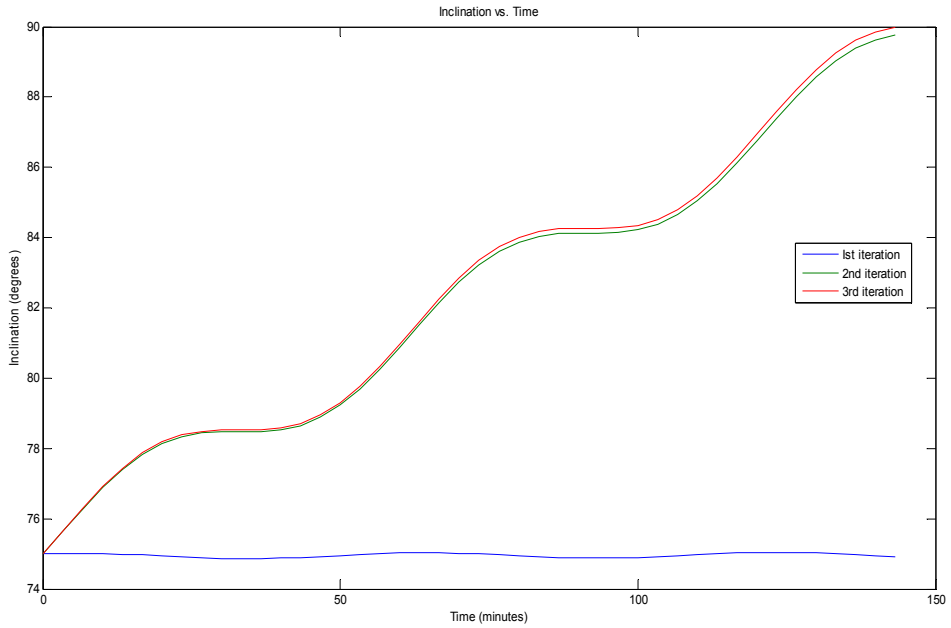

Figure 4.1. Correction of an Initial 15° Inclination Error

As seen in Figure 4.1, the 15° error is sufficiently corrected after only three iterations.

It is emphasized that assuming that no constraints are imposed on the values of the ascending node and inclination along the path can only be tolerated for small time durations. Therefore, Controller B is not used for long time durations, for if it were it would defeat the purpose of obtaining a Sun-synchronous orbit.

4.6. SPECIAL CONSIDERATIONS FOR EQUATOR AND POLE CROSSINGS

An analysis of the partial derivatives of the cost function in Equation (4.30) has shown that there are certain regions where the partial of one of the terms will go to zero. Specifically, it has been found that around equator crossings the partial derivative due to the ascending node term will go to zero and around pole crossings the inclination term

will go to zero. This comes from the fact that due to the geometry of the orbit, the ascending node and inclination cannot physically be controlled around equator and pole crossings, respectively. In other words, in these areas a suitable control function simply does not exist. When attempts are made to use Controller A through these regions, a specific trend is seen. As the spacecraft enters the problematic region, the orbital element that cannot by physically controlled will start to exhibit uncontrolled oscillations, and after getting passing through the region the oscillations will increase rather than decrease. Figure 4.2 shows an example of this behavior when trying to use Controller A to control the inclination around the Moon's North Pole.

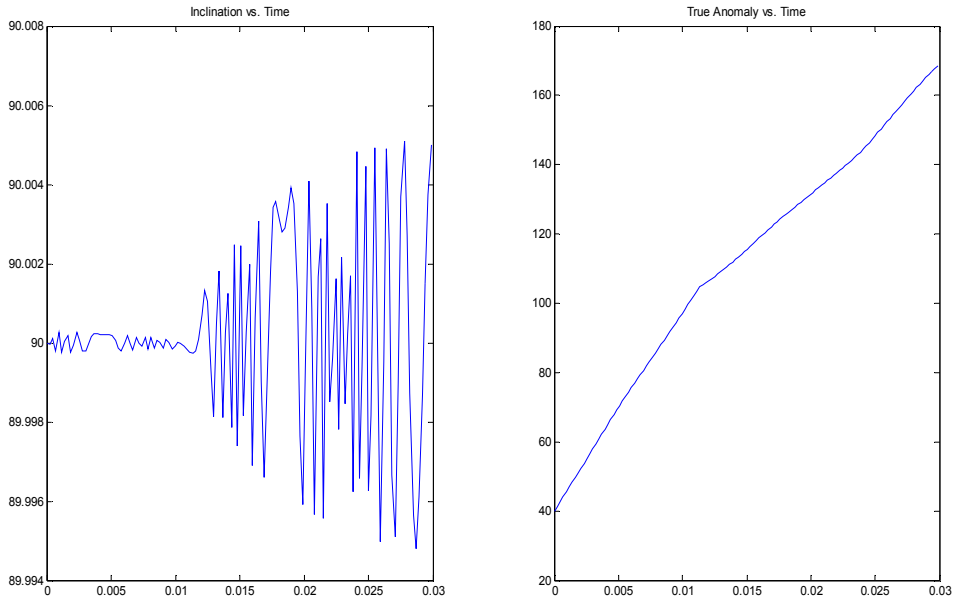

Figure 4.2. Example of Control Difficulties around Pole Crossings

It is theorized that this behavior occurs due to problems with the transition matrix algorithm not being able to converge when singularities exist along the path. It is possible that there might be a value for $\lambda(t_0)$ that, when used, will allow Controller A to stabilize the trajectory after one of these regions, but $\lambda(t_0)=0$ is apparently not a sufficient initial

guess for achieving the desired $\lambda(t_0)$. Due to this difficulty, a different type of controller needs to be used when traversing these problematic regions.

It would seem that one possible method for solving this problem would be to simply set the weight for the orbital element that cannot be controlled to be equal to zero when going through these regions. However, after leaving the region, the oscillations of the uncontrolled orbital element would then have to be dampened out, leading to the same situation stated earlier. A better solution is to utilize the terminal state controller that was described in the previous section.

It was arbitrarily decided that at approximately 10° in latitude before each equator and pole crossing, a switch would be made from Controller A to Controller B. The final values of the states produced by Controller A are set as the initial states for Controller B. Controller B is then used from 10° before the problematic region to 10° after, with the terminal boundary conditions specifying a polar, Sun-synchronous orbit. After completion of the Controller B run, a switch is made back to Controller A, which can now operate successfully due to the states being corrected to their nominal values.

As stated in Section 4.5, one difficulty with Controller B is that it can only be used for small time durations since it places no constraints on the ascending node and inclination along the path. However, since the 20° of latitude over which Controller B would operate in the above plan would only account for roughly six minutes of the satellite's total orbit period, this does not pose a problem.

It should again be noted that because of this switching method, the combined trajectories can no longer be considered optimal. Ambiguity is added to the problem by switching to Controller B at 10° in latitude before the problematic regions, since it is possible that switching to the controller at a different latitude could lead to a more optimal trajectory. The 10° in latitude was chosen by simply performing simulations and noticing that one of the orbital elements will start to follow its uncontrolled path roughly 10° before an equator or pole crossing. A search will be made for a method to get beyond these problematic regions and still generate trajectories that can be considered optimal, as explained in Section 7.

5. CASE STUDIES AND RESULTS

This section contains simulations performed using the controllers developed in Section 4, as well as case studies to show the effects of changing the control weight w_3 in the cost function. Results are first presented for inclination-only and ascending node-only control to show the controller's effectiveness at controlling each individual element. Next, results are presented for combined inclination and ascending node control, and it is shown that difficulties arise when attempting to control both orbital elements at the same time. Finally, longer duration simulations are presented which show the successful generation of a longer-term Sun-synchronous orbit. Each of the simulations presented in this section is performed using terms in the lunar gravity model up to 25x25.

5.1. SIMULATIONS OF ASCENDING NODE-ONLY CONTROL

In this section, simulations are presented which show the effectiveness of Controller A at maintaining a Sun-synchronous orbit. For this analysis the polar orbit requirement is removed, and it is therefore only desired to control the rate of change of the ascending node to coincide with the Sun-synchronous rate of 0.9856°/day. This is performed by setting the inclination weight w_1 in Equation (4.30) to be equal to zero.

The simulations in this section were all performed using the initial orbital elements defined in Table 5.1.

Table 5.1. Initial Orbital Elements for Ascending Node-only Control Simulations

Orbital Parameter	*Value*
Semimajor axis, a_i	1837.4 km
Eccentricity, e_i	0.0013
Inclination, i_i	90°
Ascending Node, Ω_i	45°
Argument of Periapsis, ω_i	15°
True Anomaly, ν_i	10°

The initial orbital elements were chosen to start in a specific type of orbit. The semimajor axis is chosen as 1837.4 km so that the orbit will initially be roughly 100 km in altitude, which corresponds to a low-lunar orbit. Also, the eccentricity is chosen as 0.0013 so that the orbit will be nearly circular and the inclination is chosen as 90° so that the orbit will be polar. Finally, the true anomaly was chosen as 10° so that the orbit is begun directly after an equator crossing.

Figures 5.1-5.3 show the results of a 0.03 day (43.2 minutes) integration of Controller A with Ascending Node-only control using the initial orbital elements defined in Table 5.1. The small 43.2 minute timespan is chosen so that an equator crossing does not have to be dealt with. Because of this, no switch from Controller A to Controller B needs to be made, and therefore the trajectories presented can be considered optimal. Figure 5.1 shows the orbital element trajectories, Figure 5.2 contains a plot showing the evolution of the costates, and Figure 5.3 shows a plot of the optimal control accelerations.

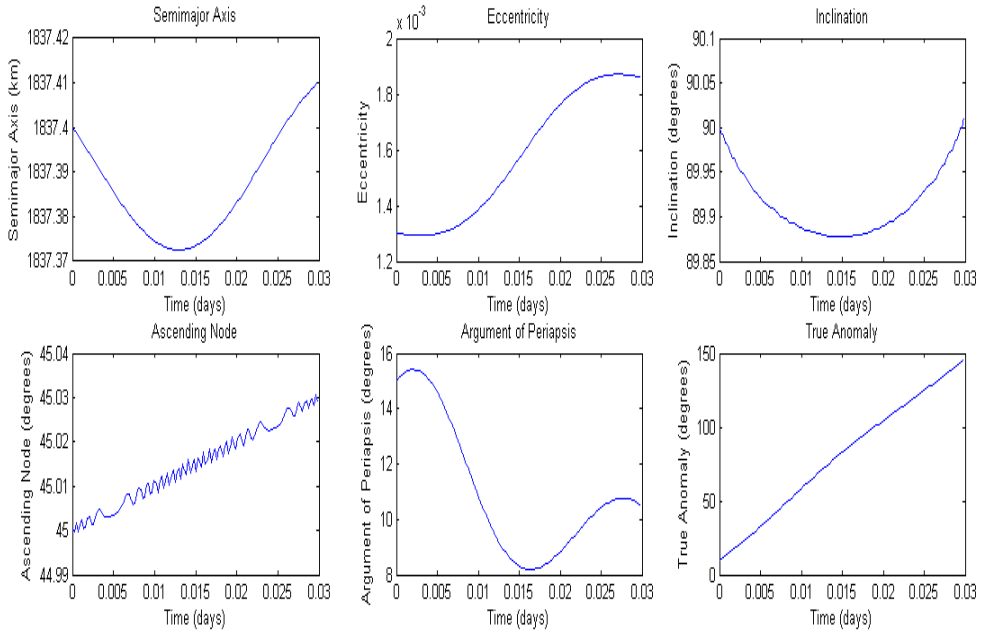

Figure 5.1. Simulation of Ascending Node-only Control

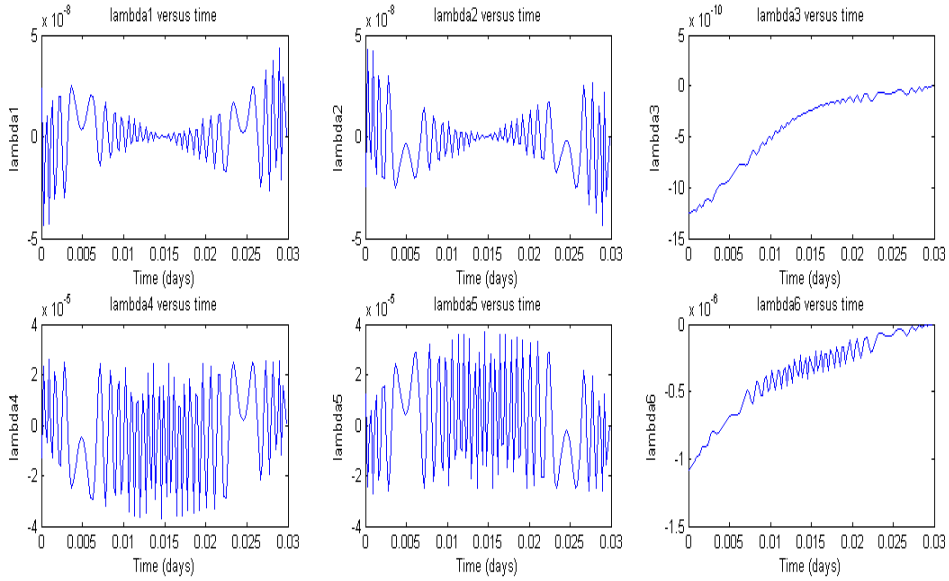

Figure 5.2. Costate Evolution for Ascending Node-only Control

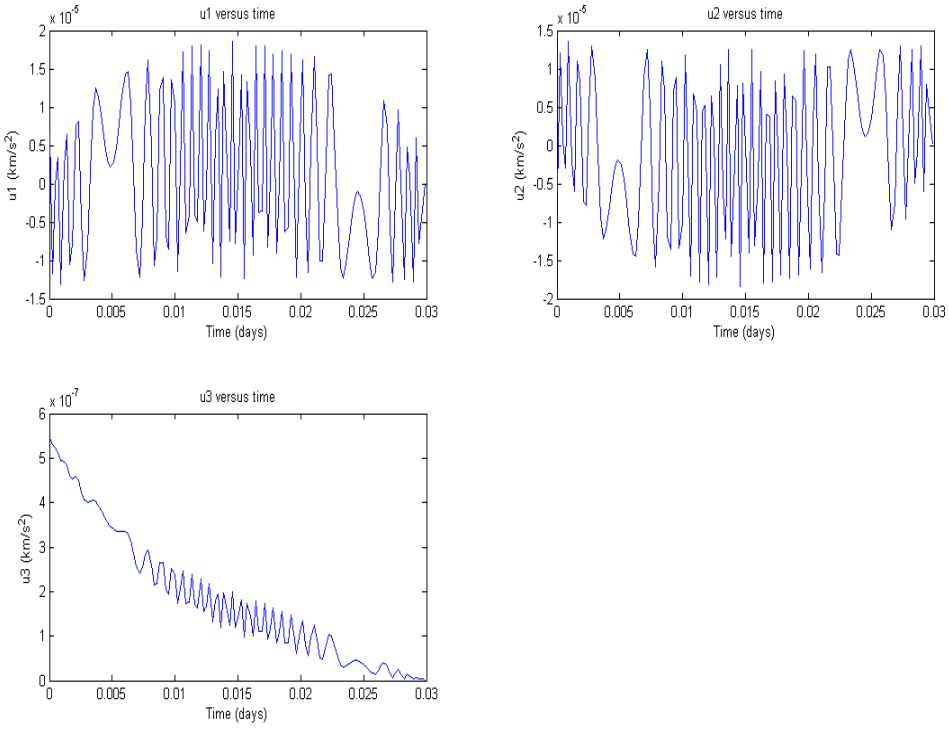

Figure 5.3. Control Accelerations for Ascending Node-Only Control

From Figure 5.1, the main feature to notice is that the ascending node is correctly rotated by approximately 0.03° in 0.03 days, demonstrating that a Sun-synchronous orbit is obtained. While performing this, it is seen that the other five orbital elements are not adversely affected by the continuous thrusting. The semimajor axis and eccentricity actually follow their uncontrolled trajectories since no in-plane thrusting is performed.

Figure 5.2 shows the behavior of the costates during the integration, and it can be seen from the plots that the costates are all successfully driven to the desired final costate value of $\lambda(t_f) = 0$ prescribed by Equation (4.54). The final costates converged after only three iterations, validating the transition matrix algorithm used to solve the problem. Since Equation (4.54) is satisfied, the necessary conditions for optimality are all achieved and a stationary point of the performance index J is obtained.

It can be seen from Figure 5.3 that the required control accelerations stay fairly small, never getting larger than 2 x 10^{-5} km/s^2. Also, it is found that the acceleration in the $\hat{z}$ direction, u_3, is two orders of magnitude smaller than the other two acceleration components. This is due to the fact that the inclination is very close to 90°, meaning that the $\hat{z}$ axis will be almost parallel to the orbit plane. Since only out-of-plane thrusting is performed, it is thus expected that u_3 will be very small.

Having shown that a Sun-synchronous orbit is achieved, it is next desired to study the effects of increasing the weight on the control accelerations, w_3, in order to see if it is possible to decrease the required control accelerations while still achieving a Sun-synchronous orbit. A case study was therefore performed in order to examine the effects of large control weights. In order to convert the control accelerations into forces, a spacecraft mass of 1000 kg is assumed. A 0.03 day integration of Controller A was performed for various values of w_3, and plots of the ascending and control force magnitude

$$u_{mag} = \sqrt{u_1^2 + u_2^2 + u_3^2} \tag{5.1}$$

were obtained from each integration. These plots can be found in Figures 5.4-5.8.

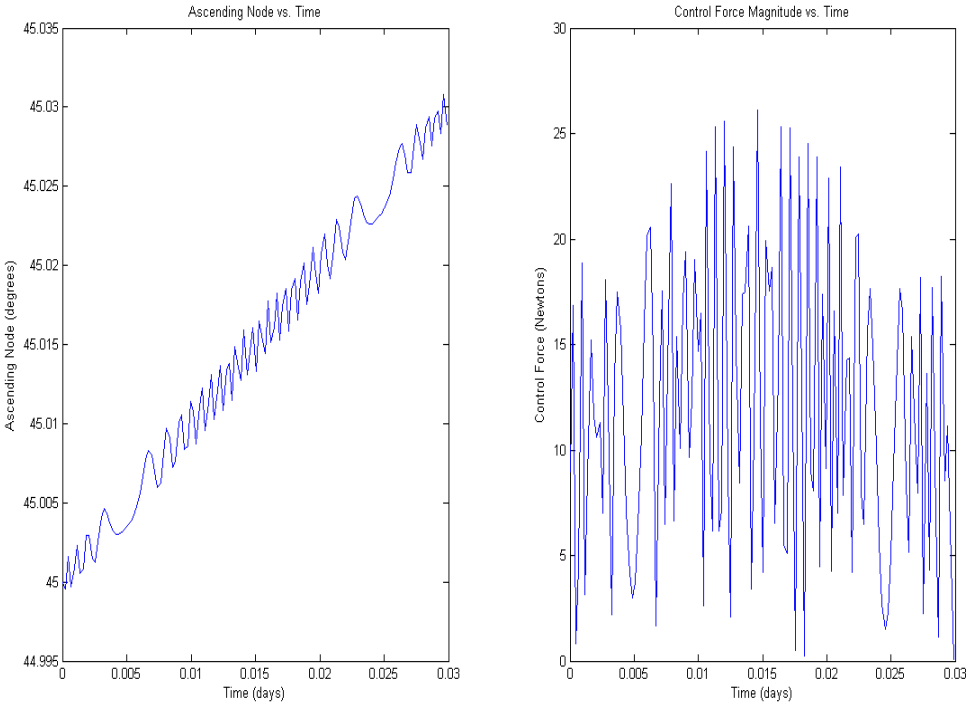

Figure 5.4. Case Study 1: $w_3 = 1$

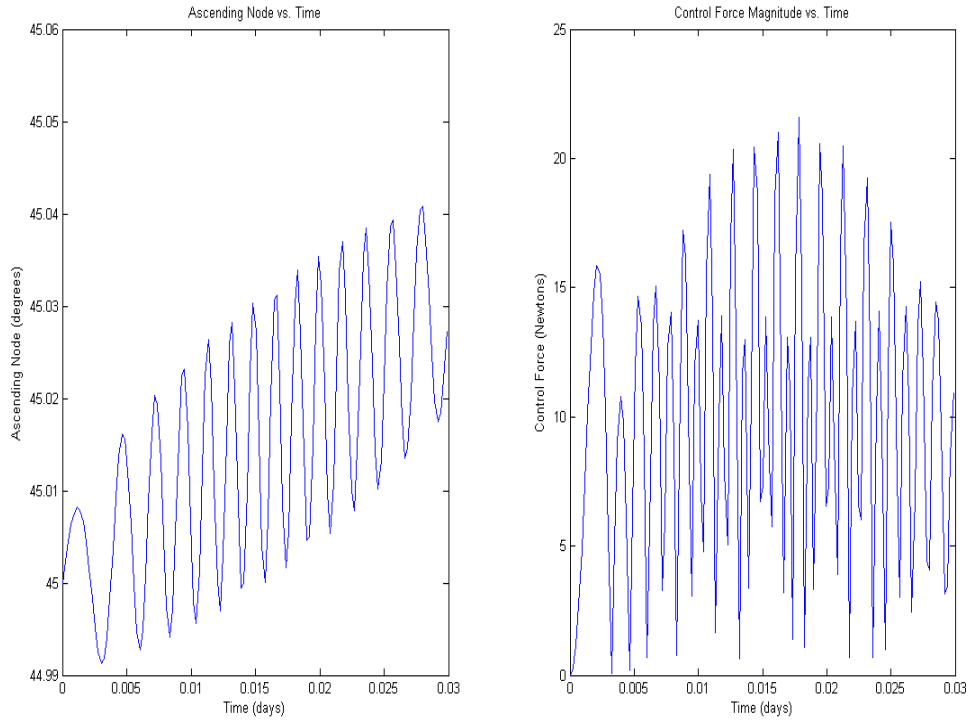

Figure 5.5. Case Study 1: $w_3 = 3$

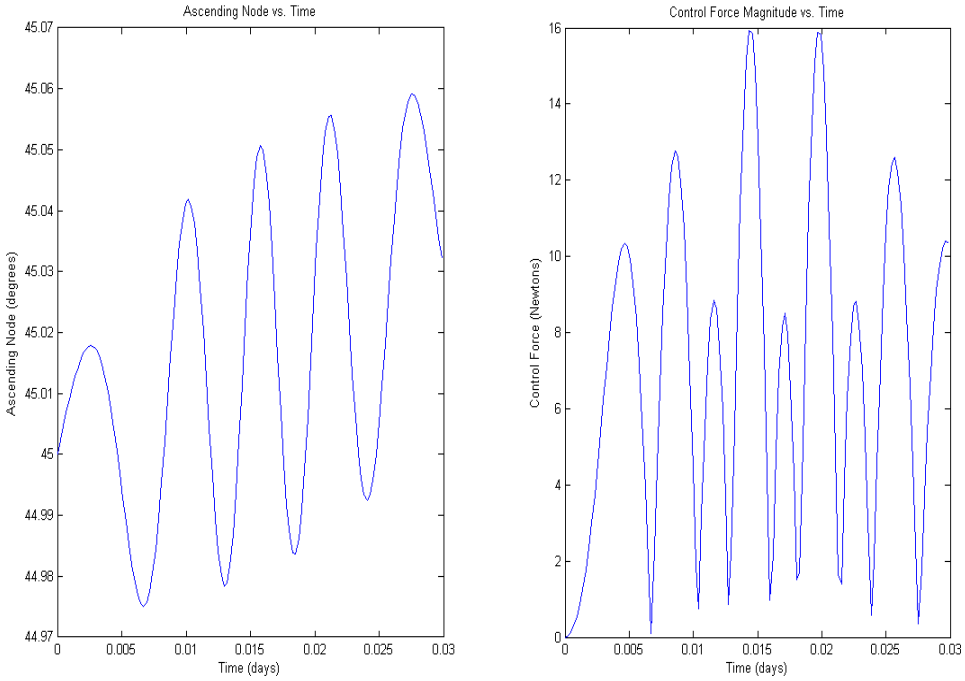

Figure 5.6. Case Study 1: $w_3 = 7$

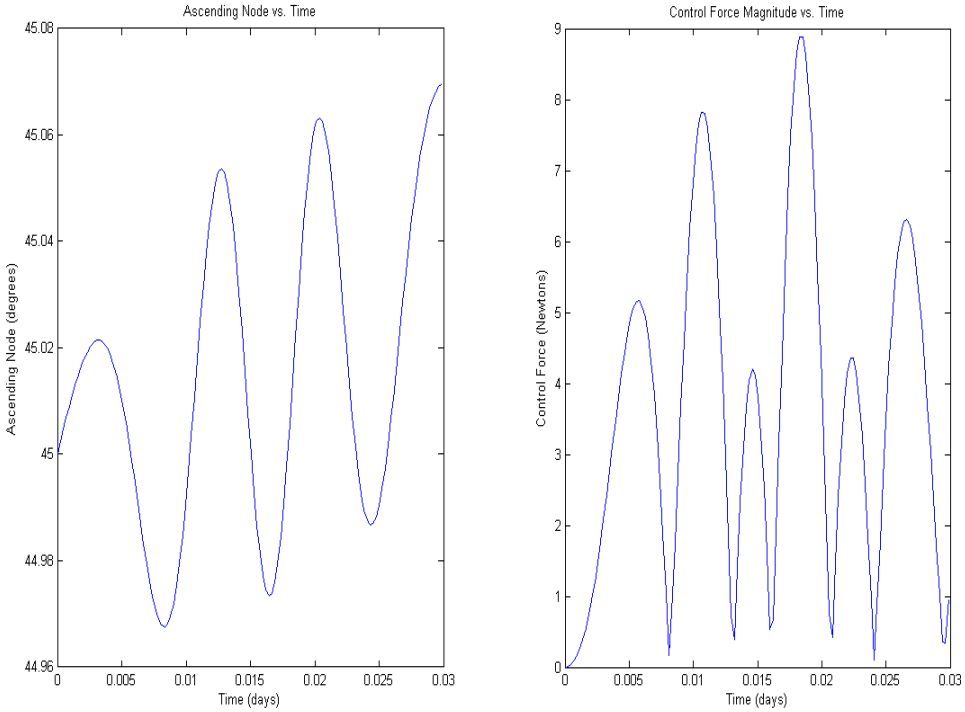

Figure 5.7. Case Study 1: $w_3 = 12$

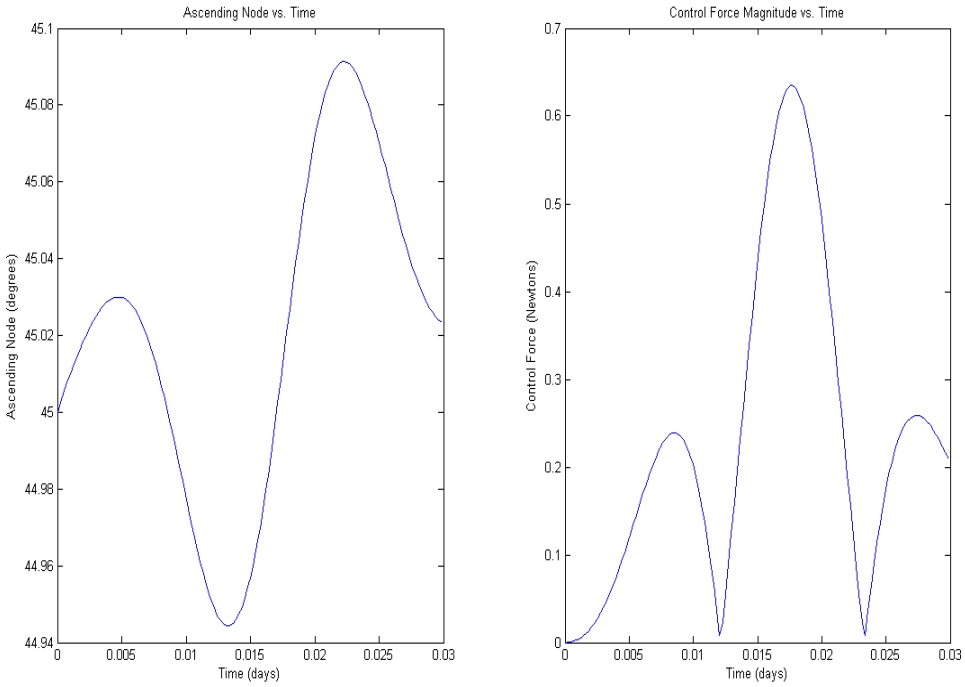

Figure 5.8. Case Study 1: $w_3 = 20$

An examination of Figures 5.4-5.8 shows that by increasing the control weighting, the magnitude of the control force decreases but the ascending node begins to deviate from the Sun-synchronous path. When $w_3 = 1$, the ascending node is tightly controlled with an average thrust magnitude of approximately 25 N, whereas when $w_3 = 20$ the ascending node deviates from the Sun-synchronous path by around 0.1° with a highly decreased average thrust magnitude that is less than 0.7 N. However, this 0.1° deviation is still usually acceptable, especially for long duration missions.

The above case study shows that a Sun-synchronous orbit can be achieved using thrust levels lower than 0.7 N, levels which are within the capabilities of current low-thrust hardware. Therefore, a low-thrust Sun-synchronous orbit can be achieved.

5.2. SIMULATIONS OF INCLINATION-ONLY CONTROL

In order to gauge the capabilities of the controllers for maintaining a polar orbit, simulations were performed where only inclination is controlled. Therefore, all of the

simulations in this section were created by setting the ascending node weight w_2 in Equation (4.30) to zero.

While the natural motion of the ascending node is to continuously deviate from the Sun-synchronous path, the inclination will naturally perform small oscillations about its initial value when left uncontrolled, as seen in Figures 3.5-3.10. This leads to the supposition that the control accelerations required for inclination stationkeeping will be less than the accelerations required for ascending node stationkeeping. This assumption is found to be true from the simulations presented in this section.

The first simulation presented in this section is a 0.03 day (43.2 minutes) integration of Controller A with inclination-only control. The initial orbital elements used for this simulation are defined in Table 5.2.

Table 5.2. Initial Orbital Elements for Inclination-only Control Simulations

Orbital Parameter	*Value*
Semimajor axis, a_i	1837.4 km
Eccentricity, e_i	0.0013
Inclination, i_i	90°
Ascending Node, Ω_i	45°
Argument of Periapsis, ω_i	20°
True Anomaly, ν_i	-80°

As in the simulation for ascending node-only control, the initial orbital elements were chosen to correspond to a 100 km, nearly circular polar orbit. However, a different true anomaly of -80° is chosen so that the orbit will begin directly after a pole crossing.

As with the simulations in the previous section, the duration of 0.03 days is chosen so that a switch from Controller A to Controller B is not required. Figures 5.9-5.11 show the results from this simulation in the form of the orbital element trajectories, the evolution of the costates, and the control accelerations.

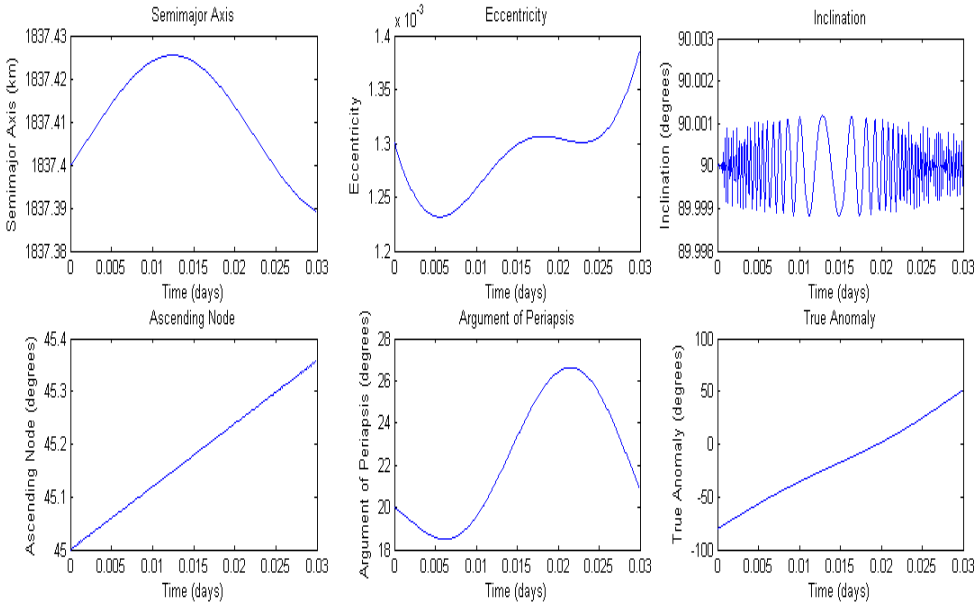

Figure 5.9. Simulation of Inclination-only Control

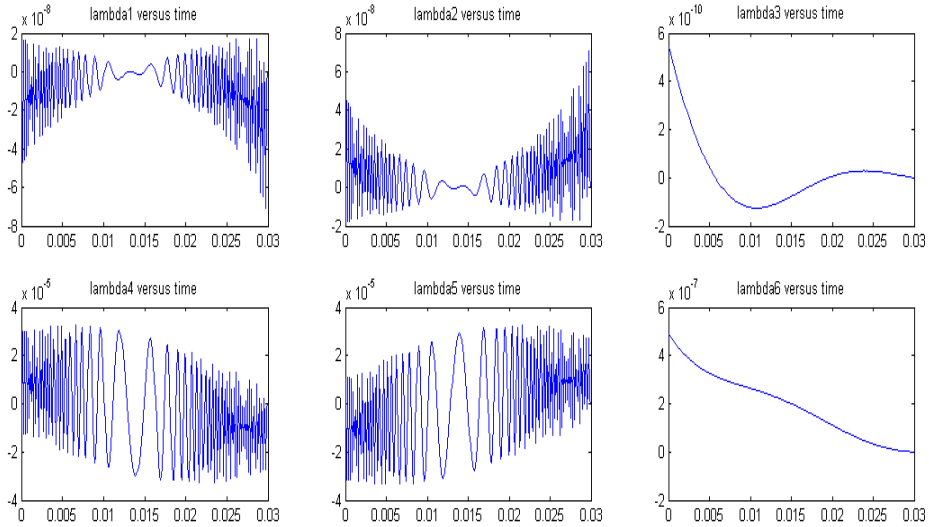

Figure 5.10. Costate Evolution for Inclination-only Control

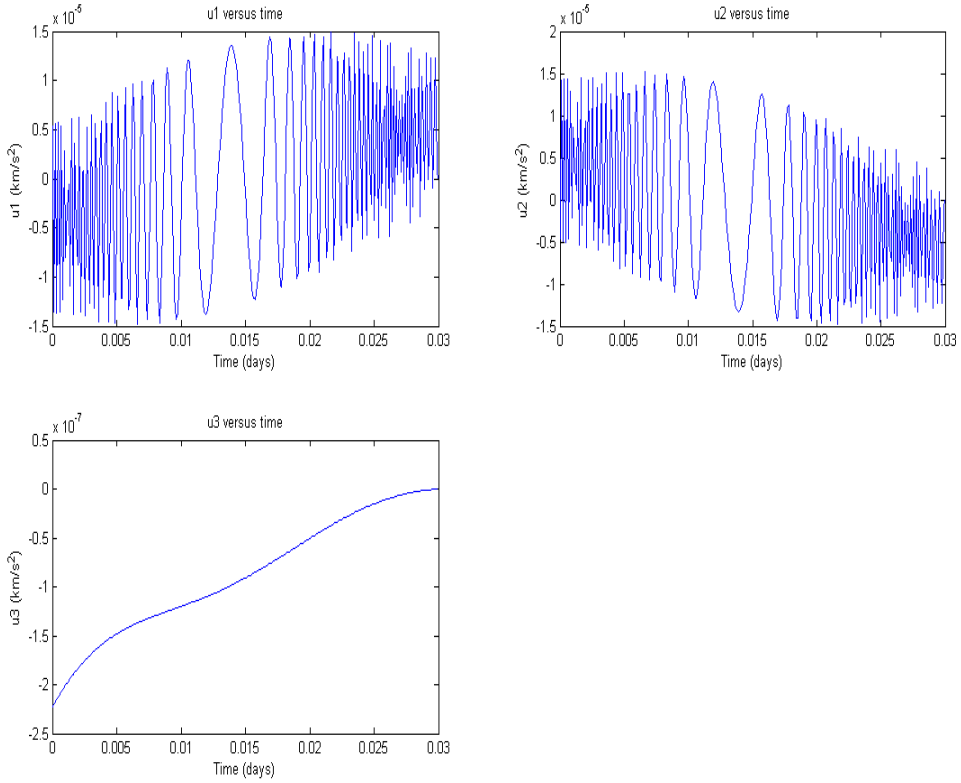

Figure 5.11. Control Accelerations for Inclination-only Control

Figure 5.9 shows that Controller A is able to perform very a tight stationkeeping control on the inclination, controlling the element to within approximately 0.001° of the desired 90°. Also, as seen in Figure 5.10, the costates are driven to the desired condition of $\lambda(t_f)=0$, implying that a stationary point of J is obtained. Finally, while it is seen from Figure 5.11 that the control accelerations are indeed slightly smaller than those required for ascending node control in Figure 5.3, the u_3 acceleration in particular is seen to be much smaller. This is due to the fact that the inclination in this simulation is maintained much closer to 90° than it is in the simulation shown in Figure 5.1, meaning that the $\hat{z}$ axis in this case is even closer to being parallel with the orbit plane. Because of this, and the fact that only out-of-plane thrusting is performed, it is intuitive that a larger portion of the total control acceleration will be delivered by the u_1 and u_2 components.

The previous simulations were all initiated with the initial states at their nominal values so that no corrections are needed initially. However, it is also desired to study the ability of combining Controller A and Controller B to correct the error in an initial element followed by maintenance of that element about its desired value. In this regard, a simulation was performed with an initial value for the inclination of 85°. The inclination is first corrected to 90° using Controller B, and then a switch is made to Controller A in order to stationkeep the inclination about 90°. The result of this simulation can be found in Figure 5.12. It should be noted that in this simulation, ascending node was not controlled.

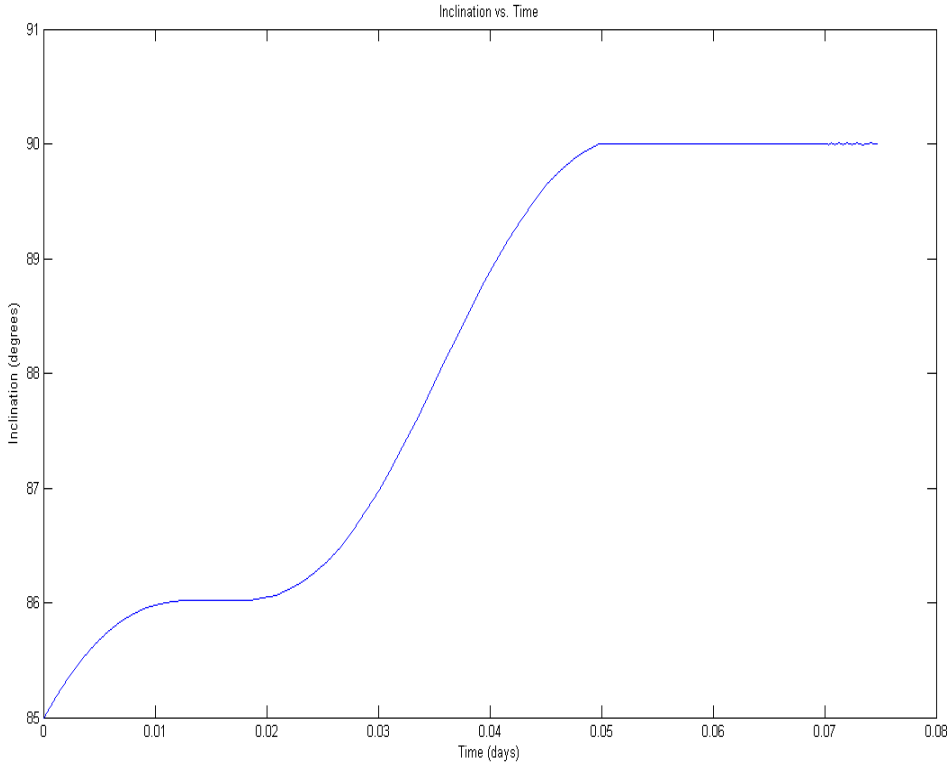

Figure 5.12. Initial Correction and Stationkeeping for Inclination

As shown in Figure 5.12, the initial 5° error is corrected in 0.05 days (72 minutes), and then successfully maintained about 90°. However, since a switch is performed between two controllers, the trajectory is only suboptimal.

Since it has been demonstrated that inclination stationkeeping can be successfully performed and that initial corrections can be made if needed, it is now desired to perform a case study in order to see the effects of control weighting on inclination control. As with the case study performed in Section 5.1, the study is conducted by performing 0.03 day integrations of Controller A with varying values of w_3. Also, a 1000 kg spacecraft mass is again assumed in order to convert the control accelerations into forces. The results of this case study can be found in Figures 5.13-5.17.

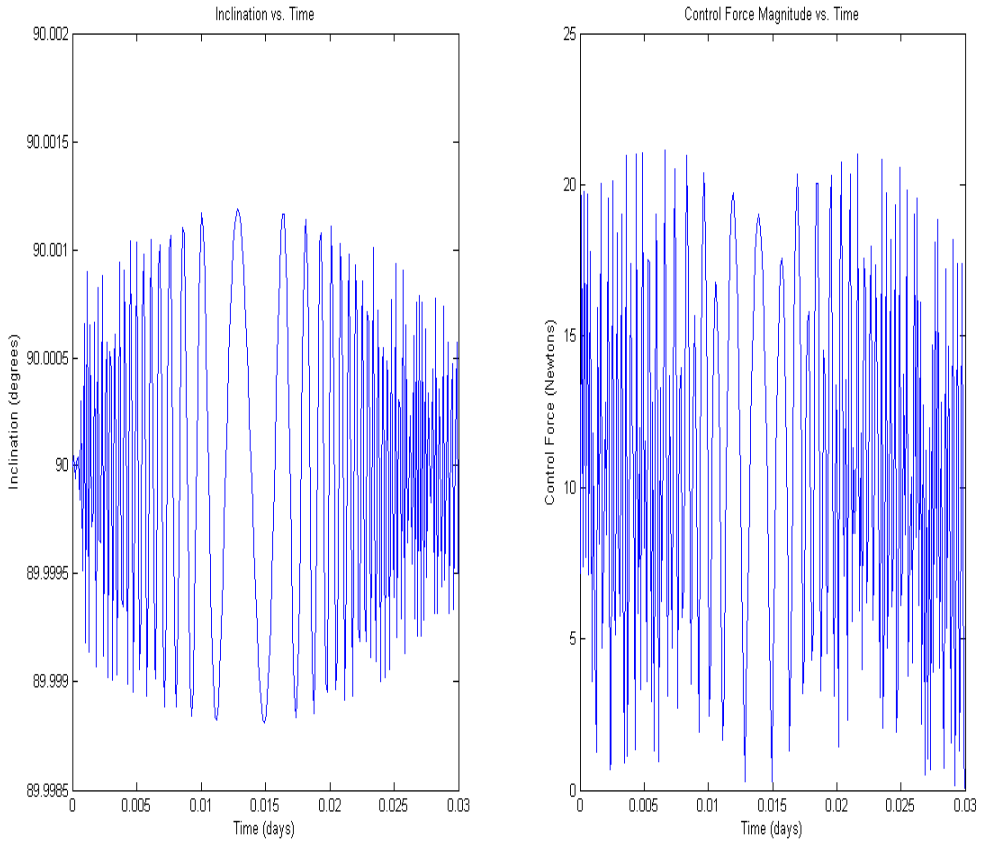

Figure 5.13. Case Study 2: $w_3 = 1$

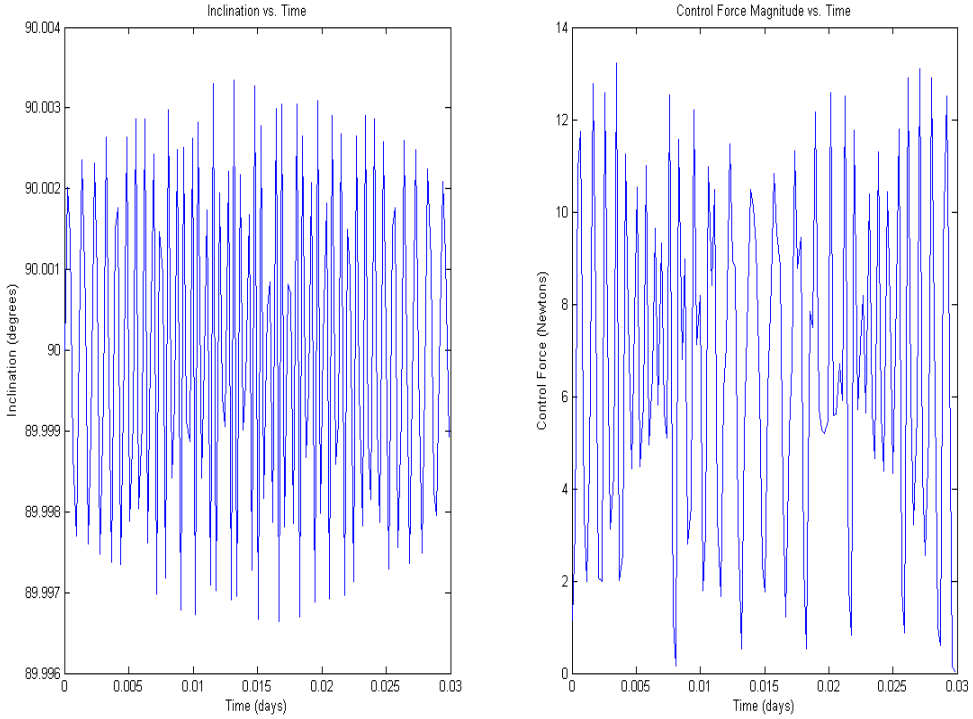

Figure 5.14. Case Study 2: $w_3 = 5$

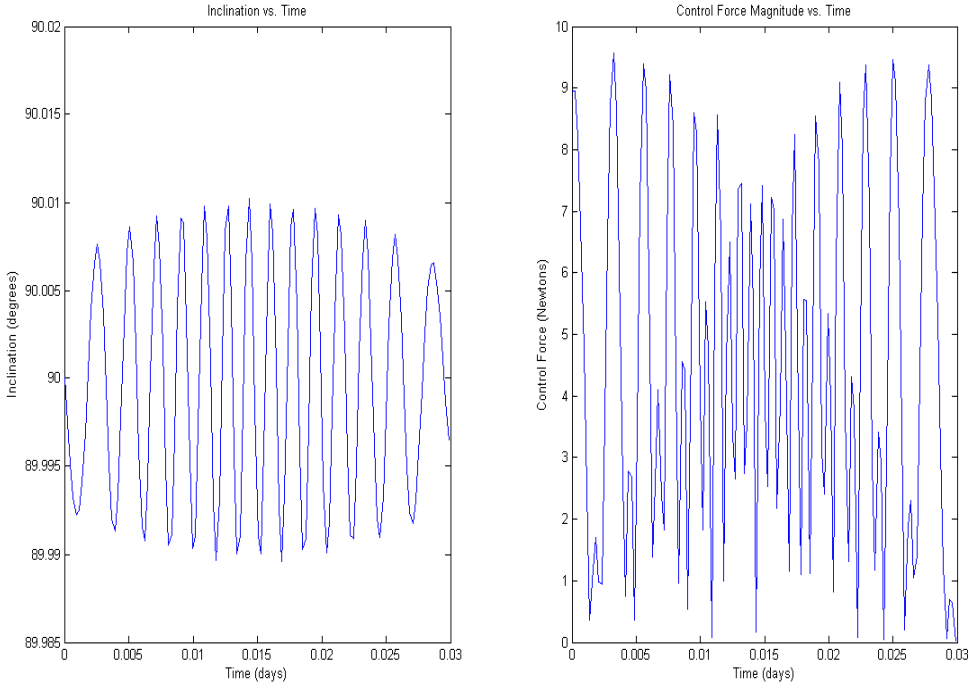

Figure 5.15. Case Study 2: $w_3 = 8$

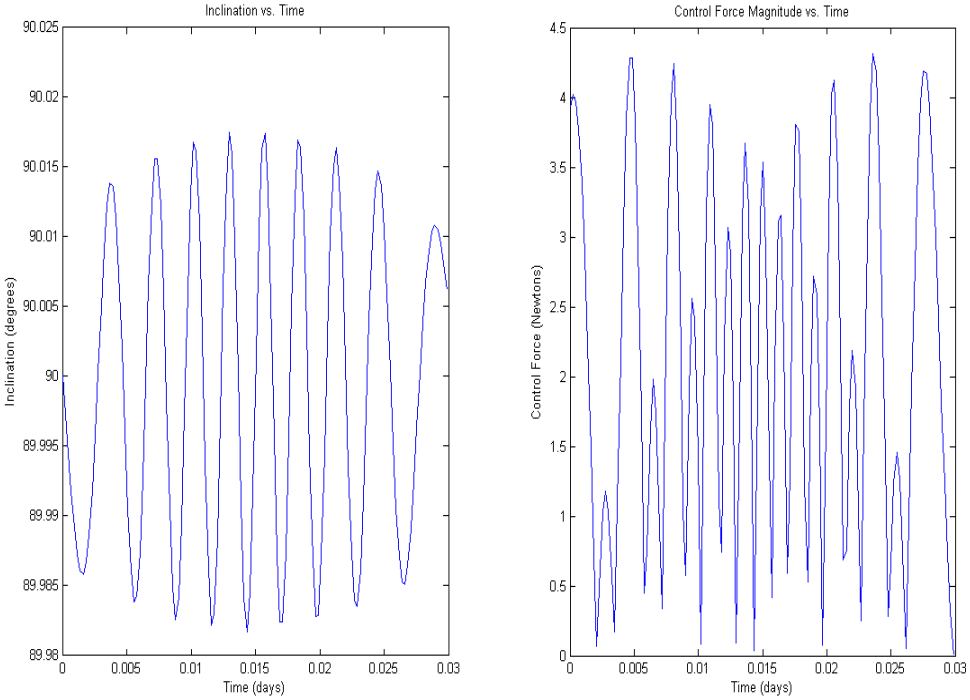

Figure 5.16. Case Study 2: $w_3 = 12$

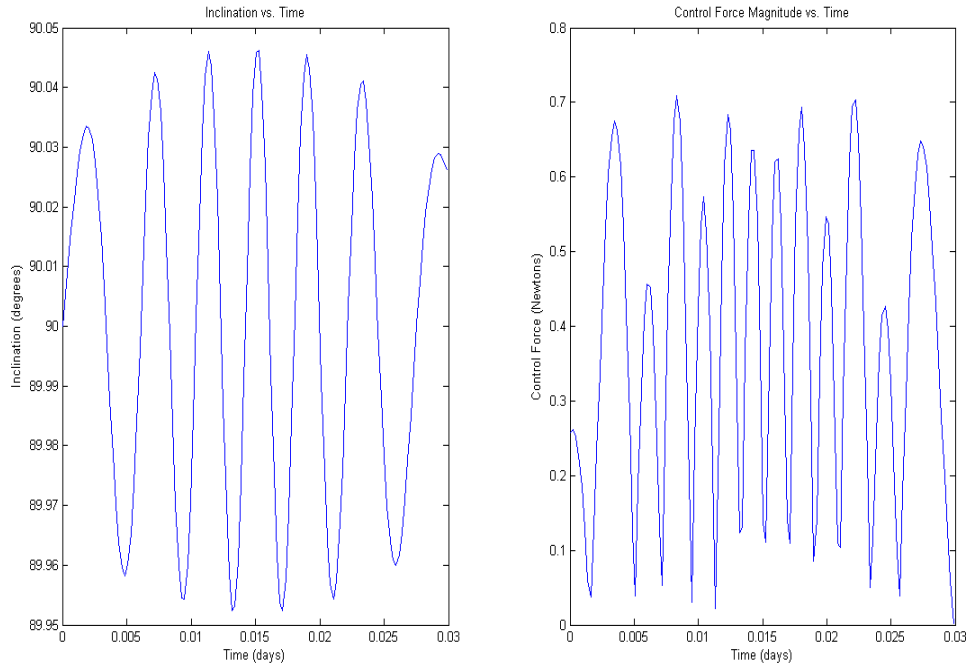

Figure 5.17. Case Study 2: $w_3 = 17$

As with the case study done in the previous section, it is again seen that increasing the control weighting will decrease the magnitude of the control force, but will also lead to larger variations in the inclination. By setting the control weighting to be equal to 17, the control force magnitude can be decreased by approximately 21 N to a low-thrust average of 0.7 N. Accompanied with this control decrease, the inclination variation is increased by approximately 0.04°. However, that amount of inclination variation is typically considered small and the orbit can still be regarded as polar.

Figures 5.13-5.17 also show that a smaller control force is required to control the inclination as compared to the ascending node. Comparing Figures 5.4 and 5.14, it is seen that with no extra weighting on the control, the inclination requires an average control force that is approximately 5 N less than that required for controlling the ascending node. It is also seen that a larger control weighting is required to decrease the ascending node control force so that it can be considered low-thrust.

5.3. SIMULATIONS OF COMBINED ASCENDING NODE AND INCLINATION CONTROL

Having proven the capability for controlling ascending node and inclination separately, it is now desired to examine how efficiently Controller A can control both of the elements at the same time. In this section, simulations are presented which incorporate both ascending node and inclination control, and it is shown that some difficulties arise when attempting to control both elements.

To study the effects of controlling both elements, a 0.01 day (14.4 minutes) integration of Controller A was performed with the weights on the ascending node and inclination terms in Equation (4.30) both set to one. The 0.01 day duration is chosen so that no pole or equator crossings are encountered, and thus no switching between Controller A and Controller B needs to be performed. The integration was performed with the initial orbital elements defined in Table 5.3. As with the previous simulations, these initial orbital elements were chosen in order to specify a 100 km, nearly circular polar orbit.

Table 5.3. Initial Orbital Elements for Combined Ascending Node and Inclination Control Simulations

Orbital Parameter	*Value*
Semimajor axis, a_i	1837.4 km
Eccentricity, e_i	0.0013
Inclination, i_i	90°
Ascending Node, Ω_i	45°
Argument of Periapsis, ω_i	15°
True Anomaly, ν_i	-80°

The results of this simulation can be found in Figures 5.18-5.20 in the form of the orbital element histories, the evolution of the costates, and the control accelerations.

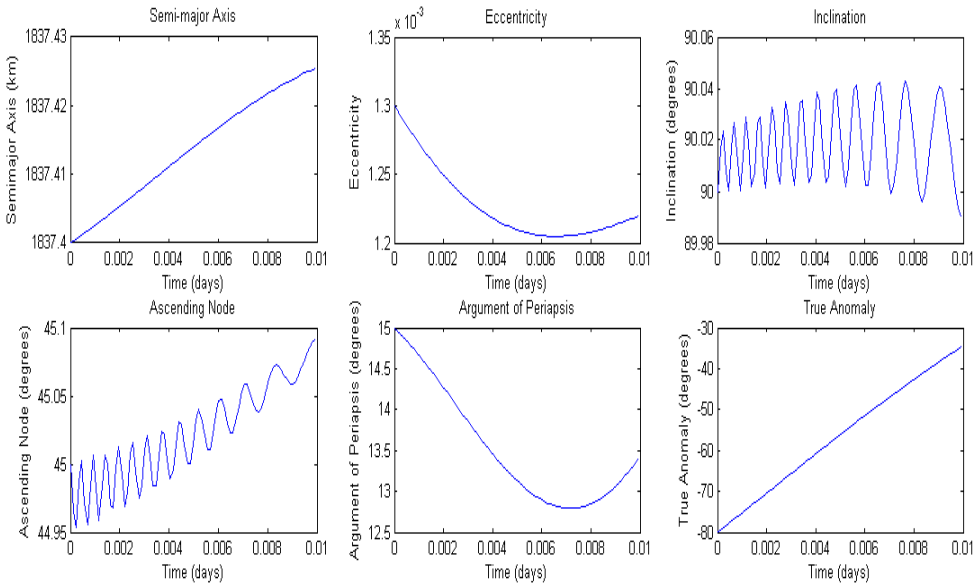

Figure 5.18. Simulation of Combined Ascending Node and Inclination Control

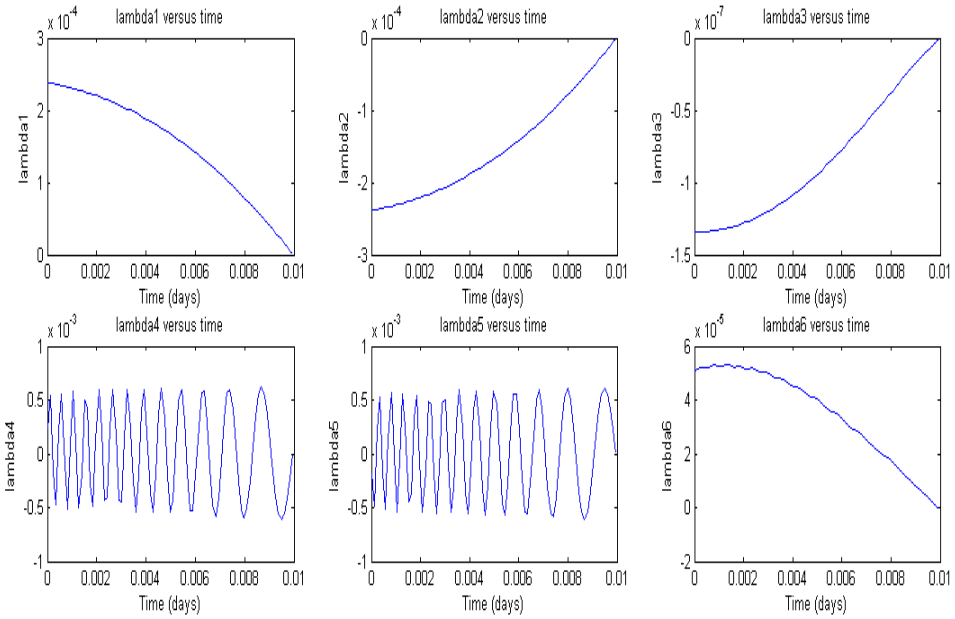

Figure 5.19. Costate Evolution for Combined Ascending Node and Inclination Control

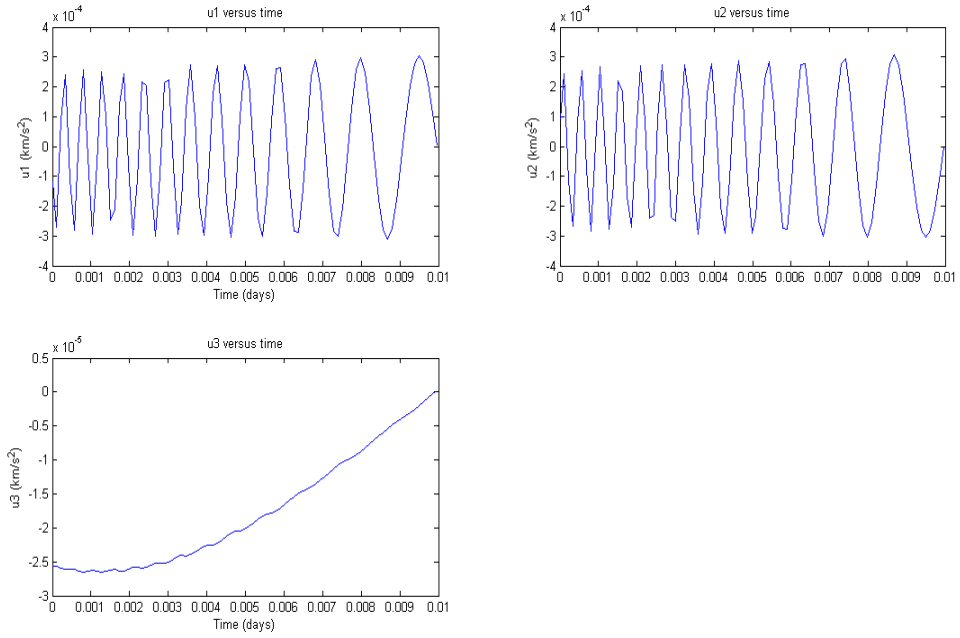

Figure 5.20. Control Accelerations for Combined Ascending Node and Inclination Control

It can be seen from Figure 5.18 that both the inclination and the ascending node have a fairly significant variance from their desired values. The inclination varies roughly 0.05° from the desired 90° value, and the ascending node deviates from the Sun-synchronous path by approximately 0.1°. While both of these variations would be tolerable, and as shown in Figure 5.19 the desired final costate is achieved, Figure 5.20 shows that the control accelerations are an order of magnitude larger than the accelerations required for controlling either element alone. Figure 5.21 contains a plot of the control force magnitude for this simulation where a 1000 kg spacecraft mass is assumed, and shows that the required control force is nearly 400 N larger than those presented in the previous sections.

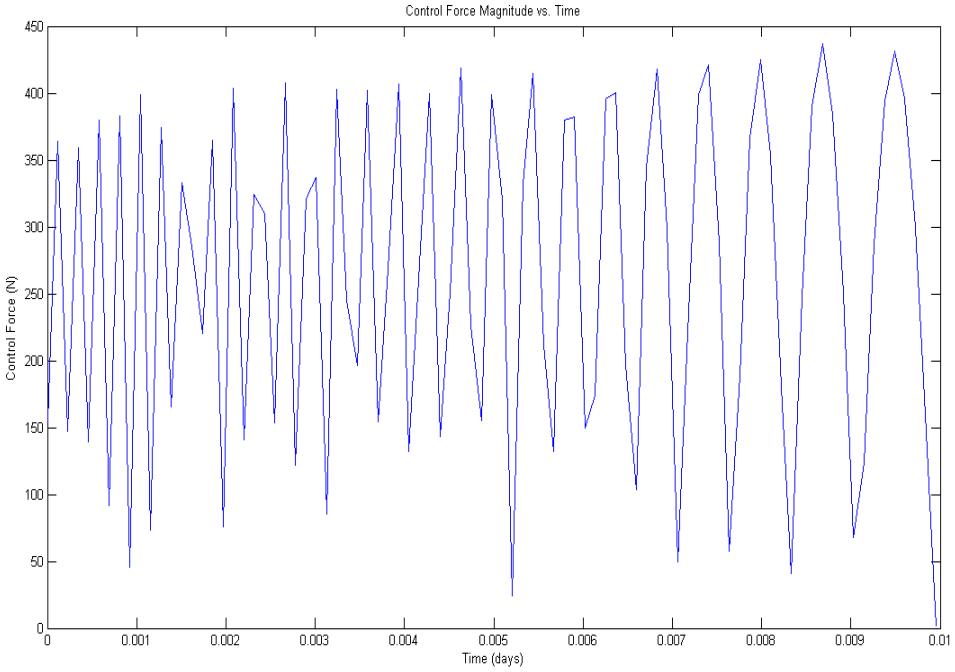

Figure 5.21. Control Force Magnitude for Combined Ascending Node and Inclination Control

Therefore, in order to decrease the control force to a magnitude where it would be considered low-thrust, a very large control weighting would have to be used. As shown in the case studies presented in Sections 5.1 and 5.2, this large control weighting will lead to

the ascending node and inclination variations in Figure 5.18 becoming substantially larger.

It is theorized that this difficulty with controlling both the ascending node and inclination stems from the fact that each element has a different requirement in terms of the force needed for control. For example, since the natural motion of the inclination is to oscillate, controlling the inclination requires an oscillating torque that will continuously be driving the inclination above and below 90°. The natural motion of the ascending node also tends to make large oscillations about its initial value, as shown in Figures 3.5-3.10, which means it will constantly tend to deviate from the desired Sun-synchronous path. Therefore, controlling the ascending node requires a torque that will constantly rotate it in the Sun-synchronous direction. Since controlling the ascending requires a relatively constant torque and controlling the inclination requires an oscillating torque, it is thought that attempting to control both orbital elements at the same time will lead to difficulties.

However, despite these difficulties, it is noticed from Figure 5.1 that when performing ascending node-only control the inclination still stays fairly close to 90°, deviating by only approximately 0.1°. Therefore, even if the ascending node is the only orbital element controlled, a polar orbit is still obtained. Also, the inclination would still be corrected back to the desired 90° when Controller B is used across equator crossings, so it is expected that in long duration simulations the inclination will not deviate substantially more than 0.1°.

From the knowledge gained from this analysis, it was decided that further long-term simulations would incorporate ascending node only control in order to achieve a polar, Sun-synchronous orbit. Since Controller A will be operating with the inclination weight w_1 set to zero, the poles will no longer be a problematic region and Controller B will only need to be used for equator crossings.

5.4 LONG TERM SIMULATIONS

5.4.1. Difficulties at Ascending Nodes of 0° and 180°. After performing simulations over a range of ascending nodes, it was found that controllability difficulties appear when the ascending node with respect to the rotating frame is near 0° or 180°. As with equator crossings, when entering one of these regions the ascending node will begin

to enter uncontrolled oscillations. However, unlike equator crossings, the time spent in these regions is substantial and on the order of 0.8 days (19.2 hours). This is an excessively large timespan for Controller B to be used, and therefore a different type of method must be used for these regions.

The reason for the control difficulties in these regions can be seen from Equations (4.48-4.53). When the ascending node with respect to the rotating frame is equal to 0° or 180°, the $\hat{\boldsymbol{x}}$ axis lies within the orbit plane. Since the angular momentum vector $\boldsymbol{h}$ is always directed perpendicular to the orbit plane, this implies that the component of the angular momentum vector in the $\hat{\boldsymbol{x}}$ direction (h_x) is equal to zero. The $\hat{\boldsymbol{x}}$ component of the angular momentum vector comes into Equations (4.48-4.53) through the auxiliary variable A. It can be seen from Equations (4.48-4.53) that when $A = 0$, $\frac{\partial L(x,u,t)}{\partial \boldsymbol{x}} = 0$. Therefore, the ascending node will experience uncontrolled oscillations when passing through these regions. However, this is strictly a property of the mathematics and the manner in which the cost function is designed. There is no physical reason for why the ascending node should be any more difficult to control at 0° than at any other angle.

Since the rotating frame $\hat{\boldsymbol{x}}$ axis rotates much faster with respect to the inertial frame than the Sun-synchronous ascending node, the rotation rate of the ascending node with respect to the rotating frame will be nearly equal to the $\hat{\boldsymbol{x}}$ axis rotation rate. In particular, the ascending node with respect to the rotating frame will rotate 360° in approximately 27.3 days. Therefore, a 0° or 180° crossing will occur roughly every 13.65 days.

As stated previously, Controller B cannot be used in these regions due to the long timespan, so a different type of method must be used. It was decided that 4° before the ascending node with respect to the rotating frame reaches a 0° or 180° value, Controller A will make a switch from ascending node-only to inclination-only control. Once the ascending node has passed either point by 4°, a switch will be made back to ascending node-only control. It should be noted that since these regions involve inclination-only control, Controller B will have to be used around equator crossings rather than pole crossings.

5.4.2. Simulations. Having devised a proper control scheme and identified all the problematic regions, it is now possible to perform simulations that gauge the controllers' effectiveness at maintaining a long-term polar, Sun-synchronous orbit. Aside from equator crossings and regions where the rotating ascending node is near 0° or 180°, these simulations involve Controller A performing ascending node-only control.

The initial orbital elements for the simulation presented in this section can be found in Table 5.4. Once again, these initial orbital elements are chosen to specify a 100 km altitude, nearly circular polar orbit.

Table 5.4. Initial Orbital Elements for Long-Term Control Simulation

Orbital Parameter	*Value*
Semimajor axis, a_i	1837.4 km
Eccentricity, e_i	0.0013
Inclination, i_i	90°
Ascending Node, Ω_i	45°
Argument of Periapsis, ω_i	15°
True Anomaly, ν_i	-80°

A 50-day simulation was performed using the initial orbital elements defined in Table 5.4 and the coefficients in the lunar gravity model up to 25x25, and can be found in Figures 5.22-5.24. Figure 5.22 contains a plot of the orbital element trajectories, Figure 5.23 shows the evolution of the control forces, and Figure 5.24 shows the total control force magnitude.

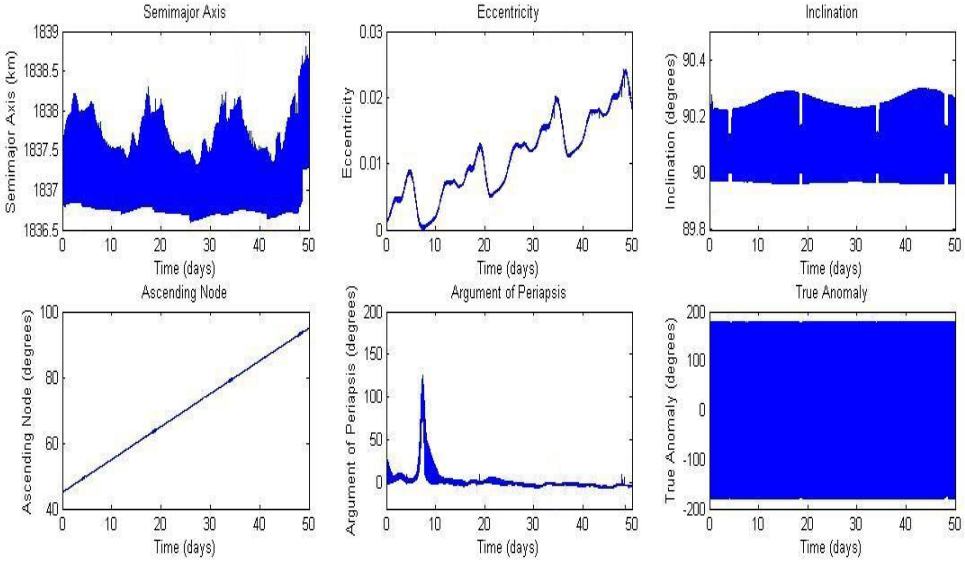

Figure 5.22. Orbital Element Trajectories for Long-Term Control Simulation

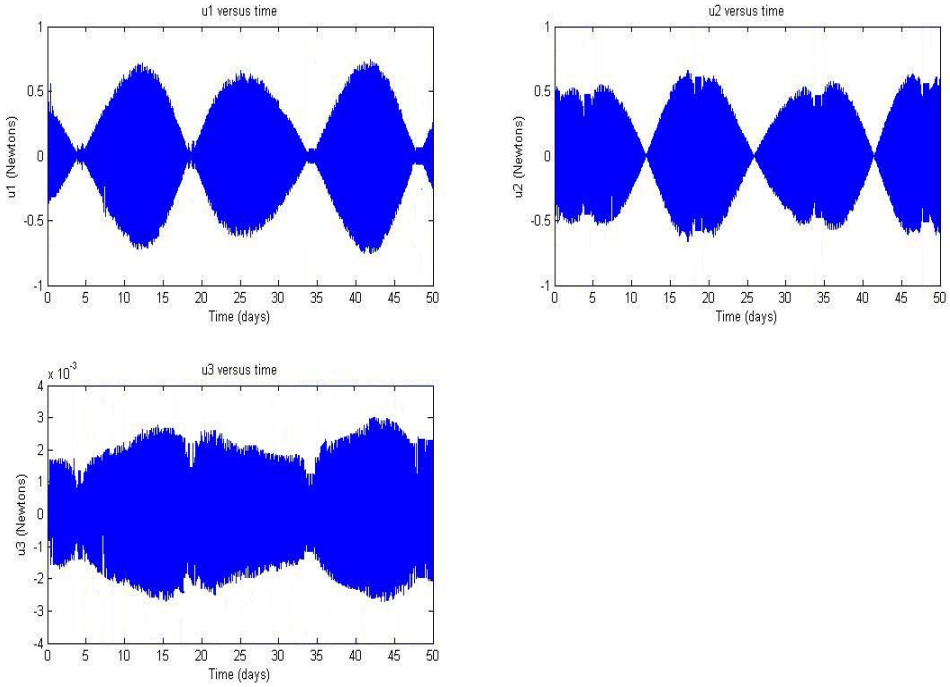

Figure 5.23. Control Force Evolution for Long-Term Control Simulation

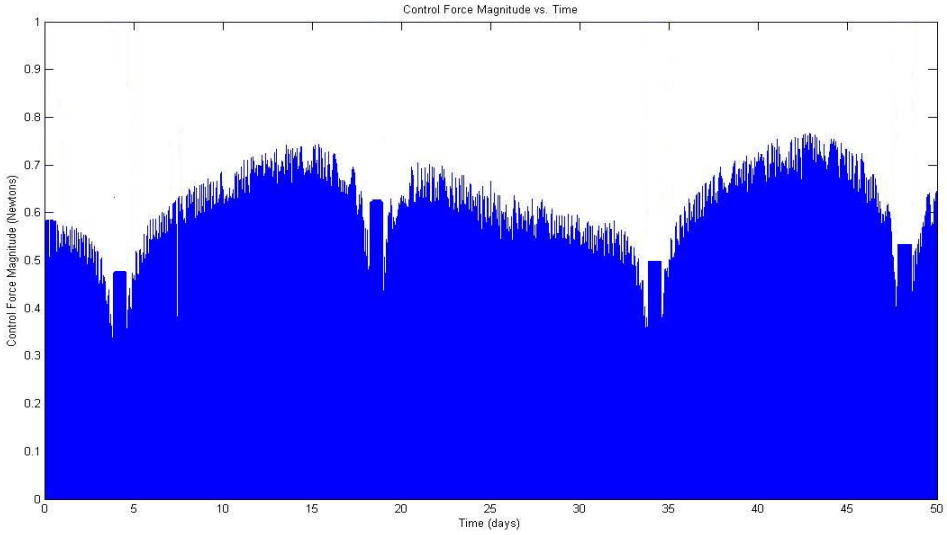

Figure 5.24. Total Control Force Magnitude for Long-Term Control Simulation

As shown in Figure 5.22, the ascending node is correctly rotated approximately 50° in 50 days. Also, the inclination is maintained close to 90°, with a maximum deviation of approximately 0.3°. Therefore, a long-term polar, Sun-synchronous orbit has been successfully achieved. Also, it can be seen from Figure 5.22 that there are four points at which the rotating ascending node is equal to 0° or 180° and a switch is made to inclination-only control. These regions are seen as spans across which the inclination is controlled much closer to 90° and the ascending node performs a slight variation from the Sun-synchronous path. It can also be seen, upon comparison to Figure 3.10, that the semimajor axis and eccentricity follow their uncontrolled trajectories and are thus not affected by the continuous thrusting.

Figures 5.23 and 5.24 show that this Sun-synchronous orbit is achieved using low thrust levels. In particular, the maximum control force in the $\hat{x}$ and $\hat{y}$ directions is approximately 0.76 N. It is also seen from Figure 5.23 that there is a slight control force in the $\hat{z}$ direction. This occurs due to the fact that the inclination is not exactly equal to 90°.

Having proven that a long-term Sun-synchronous orbit can be achieved, it is now of interest to check how close the spacecraft will get to the lunar surface and if it will

eventually impact. In this regard, a plot was made which shows the evolution of the periapsis altitude for the above simulation. The periapsis altitude is defined by

$$h_p = r_p - R_{Moon} = a(1-e) - 1737.4 \tag{5.1}$$

The periapsis is the point on the orbit at which the spacecraft is closest to the Moon's surface, and is therefore an indication of the risk of impact. The plot of the periapsis altitude evolution can be found in Figure 5.25.

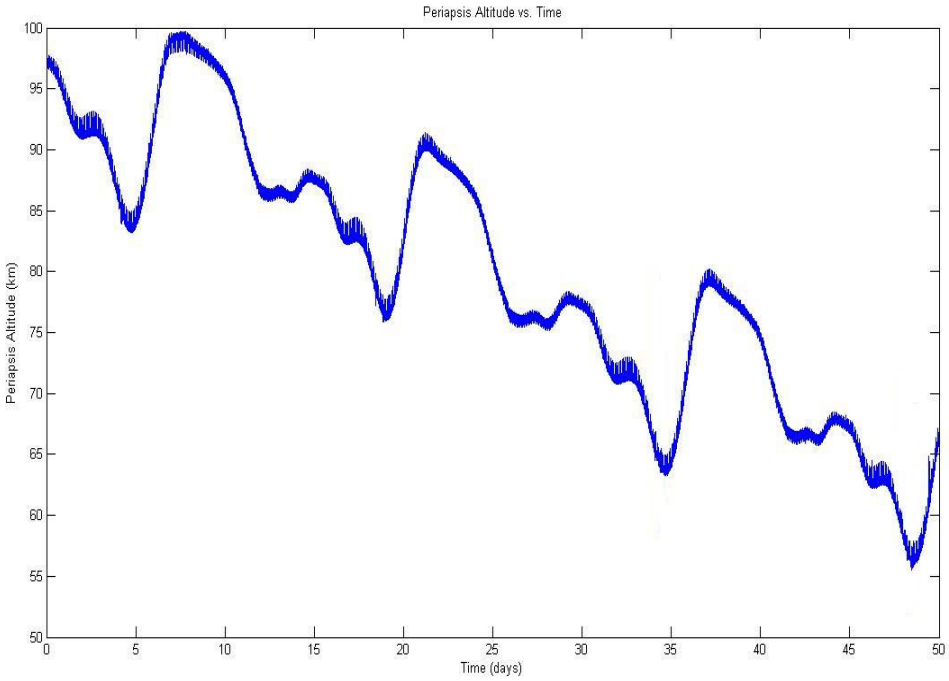

Figure 5.25. Periapsis Altitude Evolution for Long-Term Control Simulation

As shown in Figure 5.25, the periapsis altitude decreases significantly during the simulation, decreasing approximately 40 km in 50 days. This decrease in the periapsis altitude is directly affected by the highly nonspherical lunar gravity field, and is not related to the continuous thrusting that is being performed to control the inclination and ascending node. This can be seen by comparing Figure 5.25 to Figure 3.11, which shows

that the periapsis altitude evolution for the controlled case is the same as for the uncontrolled case.

From the trajectory presented in Figure 5.25, it can be seen that even though a polar, Sun-synchronous orbit was achieved, the spacecraft will eventually impact the Moon unless an in-plane control force is made to arrest the decrease in periapsis altitude. It should be emphasized, however, that the spacecraft would crash in the same amount of time even if the inclination and ascending node were not controlled.

6. CONCLUSIONS

This thesis presents a method for creating and maintaining a polar, Sun-synchronous lunar orbit using continuous low-thrust systems. This type of orbit would be very beneficial for a lunar mapping mission by providing for constant lighting conditions. A 50-day simulation is presented which shows that a Sun-synchronous orbit can be maintained for longer-duration missions, assuming that low-thrust hardware is available that could be used for such a timespan.

Also, it has been shown that optimal control theory can be used to control various orbital elements. The use of a transition matrix algorithm for solving the optimal control problem has been validated, and the algorithm quickly converges to the optimal trajectory provided that a sufficient guess for the initial costates is on hand.

Finally, this thesis illuminates many of the effects of the highly nonspherical lunar gravity field on a lunar orbiter. In particular, it has been found that the lunar gravity field will produce a large decrease in the periapsis altitude for long-term missions. It has also been shown that the argument of periapsis will go through large oscillations due to the nonspherical gravity field. For low-altitude orbits, the spherical Moon assumption will lead to large inaccuracies. However, it has been shown that the lunar gravity field can be accurately modeled using only the coefficients in the lunar gravity model up to 25x25.

7. FUTURE WORK

While the results presented in this thesis are very promising, there are still many areas that would benefit from future work. This section outlines some possible improvements to this work that will be conducted in the near future.

First, future developments in this work will involve the search for different control methods. The transition matrix algorithm used in this work is useful for special cases, but is not sufficiently robust to admit singular regions or trajectories in which a guess for the initial costates is not obvious. Since the algorithm is ineffective during singular regions, controller switches have to be performed and the generated trajectories are only suboptimal. Therefore, a search will be made for a "direct" optimal control method. Current direct methods exist that can deal with singular regions, and therefore true optimal trajectories may be found. Also, by not necessarily requiring accurate first guesses for the initial costates, a direct method could lead to a much more robust controller.

This work can also be improved by searching for a control method that is more representational of current low-thrust hardware. The control method presented in this thesis assumes that a constantly changing thrust level is available continuously in all three directions. However, many current low-thrust devices can only produce a constant low-thrust level. Therefore, a more realistic method would involve assuming a constant thrust magnitude and switching the thrusters "on" and "off" as needed. For this reason, future work will involve the study of "bang-bang" controllers.

While a Sun-synchronous orbit was successfully obtained, it has also been shown that in order to keep the spacecraft from eventually crashing into the Moon some in-plane control force will need to be made. This could be done by including other elements such as the semimajor axis and the eccentricity into the cost function, which would minimize the variations in each element and prevent the periapsis altitude from decreasing. Also, including a term involving the argument of periapsis into the cost function would minimize its variation and lead to a constant location for the periapsis. For these reasons, future efforts in this work will involve the inclusion of additional orbital elements into the cost function. Aside from creating a long-term Sun-synchronous with a constant periapsis

altitude, the overall of future developments will be to show that optimal control theory can be used to control any general orbit.

Finally, future efforts will involve continuously increasing the fidelity of the dynamic model. One way in which the fidelity could be increased would be to add additional perturbations to the equations of motion, such as solar radiation pressure and Jupiter's gravity. Also, with many lunar missions occurring in the near-future, there will be an improving base of knowledge of the lunar gravity field. Current lunar gravity models will be updated based on information gained from these missions. Therefore, future efforts will involve updating the lunar gravity model used in this work to coincide with current advances in lunar gravity models.

APPENDIX A.
CONVERSION FROM ORBITAL ELEMENTS TO CARTESIAN COORDINATES

For many computer applications, it is necessary to convert between classical orbital elements and Cartesian coordinates. This is due to the fact that orbital elements give a very good visual indication of the size and orientation of an orbit, while Cartesian coordinates are more useful mathematically when attempting to form differential equations for the motion of a satellite. Most computer applications begin with specifying the initial state of the satellite in terms of orbital elements, and then convert those orbital elements into Cartesian coordinates in order to provide differential equations that can be integrated. Finally, after integration the states are then typically converted back into orbital elements to form. This Appendix begins with a brief overview of orbital elements, and then describes the transformation from orbital elements to Cartesian coordinates and vice versa.

Six orbital elements are needed to fully describe the motion of a satellite, and these orbital elements can be divided into two categories: in-plane orbital elements and out-of-plane orbital elements. The in-plane orbital elements describe the size and shape of the orbit, while the out-of-plane orbital elements describe the orientation of the orbit plane with respect to some specified coordinate system. A basic understanding of both of these types of orbital elements is necessary for analyzing the three-dimensional motion of a satellite.

Figure A.1 is a sketch of a typical elliptical orbit, and indicates some of the primary in-plane orbital elements.

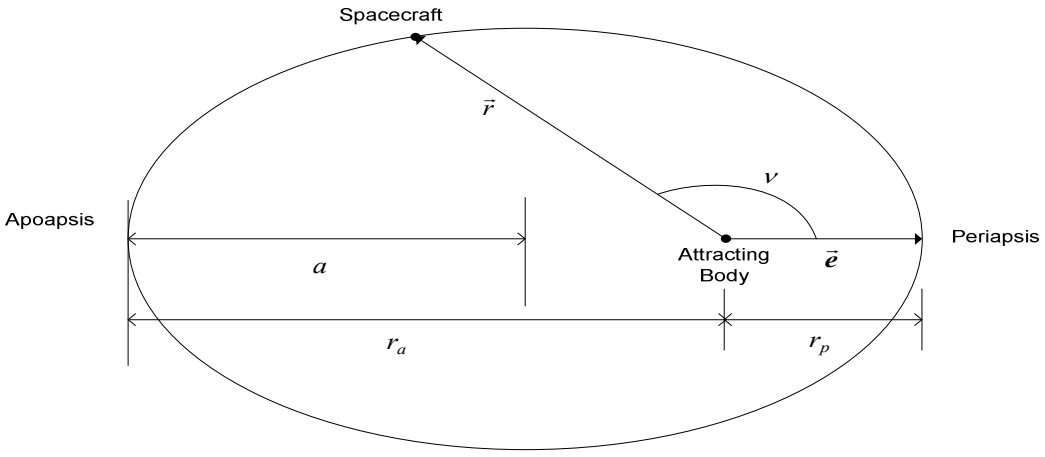

Figure A.1. General Elliptic Orbit

The attracting body is located at the primary focus of the ellipse, and the periapsis and apoapsis are the points on the orbit that are closest to and farthest from the attracting body, respectively. An orbital element that describes the size of the orbit is the semimajor axis *a*, which as shown in Figure A.1 is equal to half of the distance between periapsis and apoapsis. Another important orbital element shown in Figure A.1 is the true anomaly ν. The true anomaly locates the satellite in the orbital plane and is the angular displacement measured from periapsis to the position vector along the direction of motion [37]. One final in-plane orbital element is the eccentricity *e* which indicates the orbit's shape, or in other words its "roundness" or "flatness." An eccentricity of zero corresponds to a circular orbit, while an eccentricity of one corresponds to a parabolic orbit. As shown in Figure A.1, the eccentricity vector $\vec{e}$ is a vector from the attracting body to the orbit's periapsis.

The semimajor axis, eccentricity, and true anomaly define the size and shape of the orbit plane. However, in order to obtain the orientation of the orbit plane with respect to some fixed coordinate system, three out-of-plane orbital elements must be defined. Figure A.2 gives a sketch of an arbitrarily oriented orbit plane with respect to a fixed set of axes, and indicates the three out-of-plane elements.

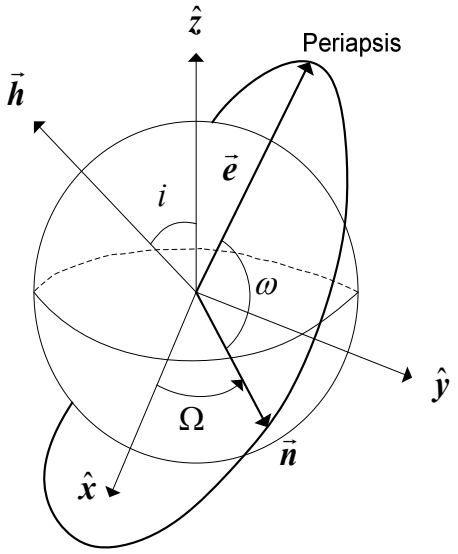

Figure A.2. Orientation of an Orbit Plane With Respect to a Fixed Coordinate System

One of the out-of-plane orbital elements seen in Figure A.2 is the right ascension of the ascending node (RAAN), Ω. The RAAN is defined as the angle from the $\hat{x}$ axis to

the point at which the orbit intersects the equator going from south to north. This point at which the equator and orbit plane meet is called the ascending node. As shown in Figure A.1, the ascending node is also identified by the node vector $\boldsymbol{n}$, which is a vector from the origin to the ascending node.

Another out-of-plane orbital element seen from Figure A.1 is the argument of periapsis, ω. The argument of periapsis is defined as the angle, measured along the orbit, from the ascending node to the orbit's periapsis.

The final out-of-plane orbital element is the inclination *i*. The inclination is defined as the angle between the $\hat{z}$ axis and the angular momentum vector $\boldsymbol{h}$, which is a vector that is always perpendicular to the orbit plane. In other words, the inclination indicates how inclined the orbit plane is with respect to the equator. An inclination of 0°corresponds to an equatorial orbit, while an inclination of 90° corresponds to a polar orbit.

Having given a brief description of the six orbital elements, it is now desired to find a method for converting from orbital elements into Cartesian coordinates. The bas goal of this conversion method is as such:

$$\text{Given} \begin{bmatrix} a \\ e \\ i \\ \Omega \\ \omega \\ \upsilon \end{bmatrix}, \text{ determine} \begin{bmatrix} x \\ y \\ z \\ \dot{x} \\ \dot{y} \\ \dot{z} \end{bmatrix}$$

A majority of the equations used in the analysis that follows are taken from Vallado [37].

Begin the transformation by defining the position magnitude *r* as

$$r = \frac{a\left(1-e^2\right)}{1+e\cos\left(\upsilon\right)} \tag{A.1}$$

Now, using the energy equation

$$\mathrm{E} = -\frac{\mu}{2a} = \frac{V^2}{2} - \frac{\mu}{r} \tag{A.2}$$

the velocity magnitude *V* can be found as

$$V = \sqrt{\frac{2\mu}{r} - \frac{\mu}{a}} \tag{A.3}$$

where μ is the gravitational parameter, which will vary depending on which body is being orbited.

Next, define the mean motion as

$$n = \sqrt{\frac{\mu}{a^3}} \tag{A.4}$$

and the eccentric anomaly as

$$E = 2\tan^{-1}\left(\tan\left(\frac{\upsilon}{2}\right)\left(\frac{1+e}{1-e}\right)^{-.5} \right) \tag{A.5}$$

The derivative of the eccentricity anomaly, $\dot{E}$, can be found as

$$\dot{E} = \frac{n}{1-e\cos(E)} \tag{A.6}$$

Now define the vectors $\boldsymbol{P}$ and $\boldsymbol{Q}$

$$\boldsymbol{P} = \begin{bmatrix} \cos(\omega)\cos(\Omega) - \sin(\omega)\cos(i)\sin(\Omega) \\ \cos(\omega)\sin(\Omega) + \sin(\omega)\cos(i)\cos(\Omega) \\ \sin(\omega)\sin(i) \end{bmatrix} \tag{A.7}$$

$$\boldsymbol{Q} = \begin{bmatrix} -\sin(\omega)\cos(\Omega) - \cos(\omega)\cos(i)\sin(\Omega) \\ -\sin(\omega)\sin(\Omega) + \cos(\omega)\cos(i)\cos(\Omega) \\ \cos(\omega)\sin(i) \end{bmatrix} \tag{A.8}$$

Using the vectors defined by Equations (A.7) and (A.8), the position and velocity vectors of the spacecraft in Cartesian coordinates can now be found through

$$\boldsymbol{r} = \begin{bmatrix} x \\ y \\ z \end{bmatrix} = a(\cos(E) - e)\boldsymbol{P} + a\sqrt{1\text{-}e^2}\,\sin(E)\boldsymbol{Q} \tag{A.9}$$

$$\boldsymbol{V} = \begin{bmatrix} \dot{x} \\ \dot{y} \\ \dot{z} \end{bmatrix} = -a\sin(E)\dot{E}\boldsymbol{P} + \boldsymbol{a}\sqrt{\boldsymbol{1}\text{-}\boldsymbol{e}^2}\,\cos(E)\dot{E}\boldsymbol{Q} \tag{A.10}$$

There are also times where it is needed to convert a system based in Cartesian coordinates into orbital elements. As explained previously, most dynamic models involve integrating equations of motions defined in terms of Cartesian coordinates, and after the

integration those coordinates are transformed into orbital elements when plotting the results. Therefore it is desired to find a second method that will perform the reverse of the method presented above. The objective of this second method is as such:

$$\text{Given} \begin{bmatrix} x \\ y \\ z \\ \dot{x} \\ \dot{y} \\ \dot{z} \end{bmatrix}, \text{ determine} \begin{bmatrix} a \\ e \\ i \\ \Omega \\ \omega \\ \upsilon \end{bmatrix}$$

Begin this second transformation by determining the position vector and velocity vector magnitudes

$$r = \sqrt{x^2 + y^2 + z^2} \tag{A.11}$$

$$V = \sqrt{\dot{x}^2 + \dot{y}^2 + \dot{z}^2} \tag{A.12}$$

Now, Equation (A.2) can be solved for the semimajor axis as

$$a = \frac{\mu r}{2\mu - rV^2} \tag{A.13}$$

Next, determine the magnitude of the angular momentum vector

$$h = |\boldsymbol{h}| = |\boldsymbol{r} \times \boldsymbol{V}| \tag{A.14}$$

Using Equations (A.14) and (A.2), the eccentricity can be found as

$$e = \sqrt{1 + \frac{2\mathrm{E}h^2}{\mu^2}} \tag{A.15}$$

Define the node vector $\boldsymbol{n}$ as

$$\vec{\boldsymbol{n}} = \hat{z} \times \frac{\vec{\boldsymbol{h}}}{|\vec{\boldsymbol{h}}|} \tag{A.16}$$

The right ascension of the ascending node can now be found through

$$\Omega = \cos^{-1}\left(\frac{\hat{\boldsymbol{x}} \cdot \boldsymbol{n}}{|\boldsymbol{n}|}\right) \tag{A.17}$$

Since the arccosine function will always return an angle between 0° and 360°, a quadrant check must be performed to ensure the correct Ω is taken. It can be seen from Figure A.2 that if the $\hat{\boldsymbol{y}}$ component of the node vector $\boldsymbol{n}$ is negative, then Ω must be between 180° and 360°. Therefore the following method will lead to the correct value for Ω from Equation (A.17):

$$[\text{ If } (n_y < 0), \text{ then } \Omega = 360° - \Omega \text{ }]$$

Next, the inclination can be found as

$$i = \cos^{-1}\left(\frac{h\hat{z}}{|h|}\right) \tag{A.18}$$

Since the inclination is defined as an angle between 0° and 180° no quadrant check is needed for Equation A.18.

The eccentricity vector can be determined by

$$\vec{e} = \frac{\left(V^2 - \frac{\mu}{r}\right)\boldsymbol{r} - (\boldsymbol{r}\cdot\boldsymbol{V})\boldsymbol{V}}{\mu} \tag{A.19}$$

With the eccentricity vector known, the argument of periapsis can be found as

$$\omega = \cos^{-1}\left(\frac{\boldsymbol{n}\cdot\boldsymbol{e}}{|\boldsymbol{n}||\boldsymbol{e}|}\right) \tag{A.20}$$

The argument of periapsis is defined as an angle between 0° and 360°, so a quadrant check must be performed. As seen in Figure A.2, if the $\hat{\boldsymbol{y}}$ component of the eccentricity vector $\boldsymbol{e}$ is negative, then ω is between 180° and 360°. This leads to the following quadrant check for the argument of periapsis:

$$[\text{ If } e_y < 0 \text{, then } \omega = 360° - \omega \text{ }]$$

Finally, the true anomaly can be found as

$$\nu = \cos^{-1}\left(\frac{\boldsymbol{e}\boldsymbol{r}}{|\boldsymbol{e}||\boldsymbol{r}|}\right) \tag{A.21}$$

This angle must also be put through a quadrant check. In order to determine a proper quadrant check for the true anomaly, the properties of the dot product between the position and velocity vectors can be analyzed. In particular, the product is always positive

when the spacecraft is going away from periapsis and negative when going towards periapsis. Therefore, the following quadrant check can be used:

$$[\text{ If } (\boldsymbol{r} \cdot \boldsymbol{V}) = 0 \text{, then } \nu = 360° - \nu \text{ }]$$

APPENDIX B.

CONVERSION FROM THE ROTATING FRAME TO THE INERTIAL FRAME

As discussed in Section 3, the coordinate system on which the equations of motion are based upon is a rotating selenographic frame. However, this presents problems when trying to define a Sun-synchronous orbit, as such an orbit requires some inertial $\hat{\boldsymbol{x}}$ axis to measure the ascending node from. Therefore, an inertial frame also needs to be specified from which the ascending node can be measured from. This appendix defines an inertial frame that can be used for this purpose, and also details a method for converting between the rotating and inertial coordinate systems.

The inertial frame chosen involves the placement of the Moon and Earth at the start of the integration. In particular, the inertial x-axis, $\hat{\boldsymbol{x}}_I$, is defined to be along the initial Earth-Moon line. The inertial z-axis, $\hat{\boldsymbol{z}}_I$, goes through the Moon's north pole and the $\hat{\boldsymbol{y}}_I$ axis completes the right-handed coordinate system. In other words, the inertial frame is chosen as the initial selenographic coordinates axes. It should be noted that since this inertial frame is defined based on the initial positions of the Earth and Moon, the orientation of the inertial frame may be different integrations. Basically, the orientation of the inertial frame will depend on the starting Julian date for the integration.

In order to form a conversion method, the properties of the selenographic coordinate frame must be analyzed. As stated in Section 3, the selenographic $\hat{\boldsymbol{x}}_s$ axis is always pointed towards Earth, and therefore the axis rotates as the Moon revolves about the Earth. One of the interesting properties of the Moon is that it revolves about the Earth at the same speed as which it rotates. It is because of this property that the same face of the Moon is always seen from Earth, and why there is currently a sparse amount of data for the back side of the Moon. The lunar rotation rate, called ω_m, is roughly constant at 2.661699 x 10^{-6} rad/sec. Therefore, after an amount of time *t*, the $\hat{\boldsymbol{x}}_s$ axis will have rotated by an angle $\omega_m t$. This rotation angle is shown in Figure B.1.

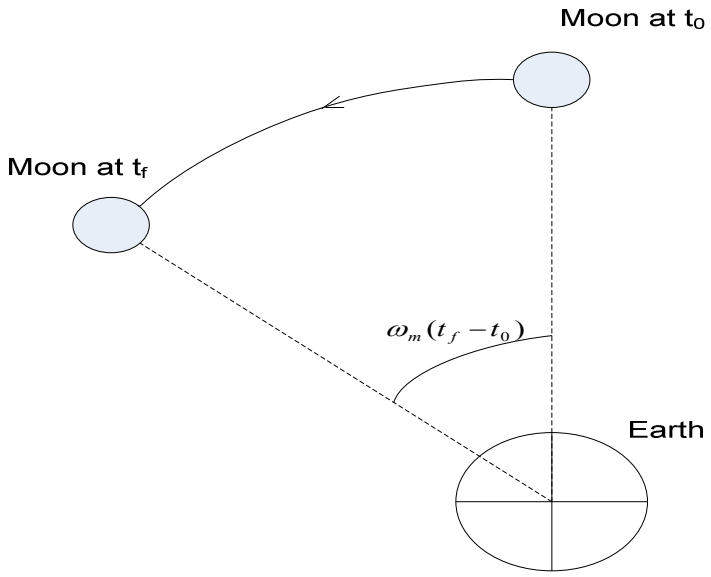

Figure B.1. Angle of Moon's Revolution about Earth

A product of the constant rotation rate ω_m is that the angle between the *x* and *y* axes for the inertial and selenographic coordinate frames will always be equal to $\omega_m t$, as shown in Figure B.2.

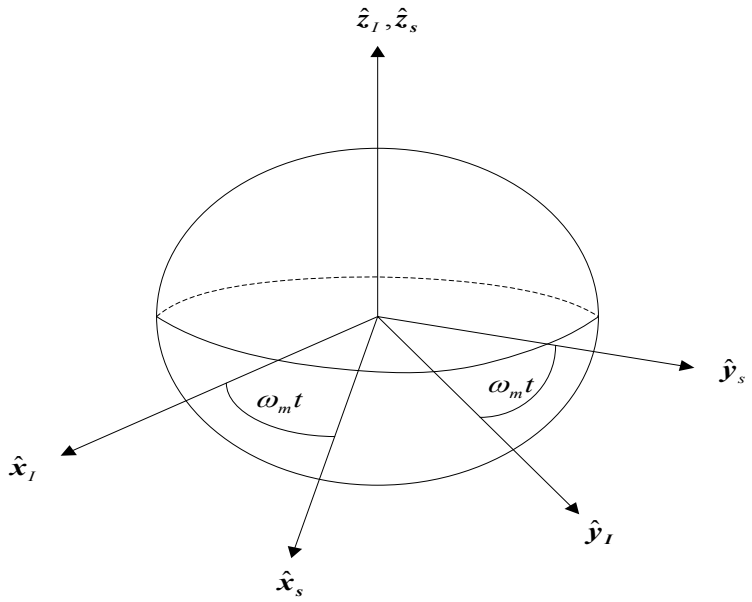

Figure B.2. Conversion Between Rotational and Inertial Coordinates

With the above knowledge, a direction cosine matrix can be made that will allow a conversion between the selenographic frame and the inertial frame. First define the angle

$$\Delta = \omega_m t \tag{B.1}$$

Using the angle Δ, the direction cosine matrix can be found as

$$DCM = \begin{bmatrix} \cos(\Delta) & -\sin(\Delta) & 0 \\ \sin(\Delta) & \cos(\Delta) & 0 \\ 0 & 0 & 1 \end{bmatrix} \tag{B.2}$$

Now, given a position vector $\boldsymbol{r_s}$ defined with respect to the selenographic frame, the corresponding position vector in the inertial frame is

$$\boldsymbol{r}_I = [DCM]\boldsymbol{r}_s \tag{B.3}$$

In order to convert a velocity vector from the selenographic frame to the inertial frame, the basic kinematic equation (BKE) must be used. Given a velocity vector $\boldsymbol{V}_s$ in the selenographic frame, the corresponding velocity vector in the inertial frame is found as

$$\boldsymbol{V}_I = \boldsymbol{V}_S + \boldsymbol{\omega}_m \times \boldsymbol{r_s} \tag{B.4}$$

Noting that $\boldsymbol{\omega}_m = \omega_m \hat{\boldsymbol{z}}$, Equation (B.4) can also be written as

$$\begin{bmatrix} \dot{x}_I \\ \dot{y}_I \\ \dot{z}_I \end{bmatrix} = \begin{bmatrix} \dot{x}_s \\ \dot{y}_s \\ \dot{z}_s \end{bmatrix} + \omega_m \hat{\boldsymbol{z}} \times \begin{bmatrix} x_s \\ y_s \\ z_s \end{bmatrix} \tag{B.5}$$

Finally, carrying out the cross product in Equation B.5 and using the state-space format defined in Section 3, the three inertial velocity components are

$$\dot{x}_I = x_4 - \omega_m x_2 \tag{B.6}$$

$$\dot{y}_I = x_5 + \omega_m x_1 \tag{B.7}$$

$$\dot{z}_I = x_6 \tag{B.8}$$

BIBLIOGRAPHY

[1] Boain, Ronald J. "A-B-C's of Sun-Synchronous Orbit Mission Design," AAS/AIAA Space Flight Mechanics Conference, 2005.

[2] Wilson, Fred C. "Recent Advances in Satellite Propulsion and Associated Mission Benefits," AIAA International Communications Satellite System Conference, 2006.

[3] Spores, R.A., Birkan M., "The USAF Electric Propulsion Program," 35th Joint Propulsion Conference and Exhibit, Los Angeles, CA, 1999, *AIAA Journal*, 99-2162.

[4] Brophy, John R. "Status of the Dawn Ion Propulsion System," AIAA International Communications Satellite System Conference, 2004, *AIAA Journal,* 2004-3433.

[5] Brophy, John R. "Development and Testing of the Dawn Ion Propulsion System," *AIAA/ASME/SAE/ASEE Joint Propulsion Conference and Exhibit*, 2006, *AIAA Journal*, 2006-4319.

[6] Jacobson, David T., Manzella, David H. "50 kW Class Krypton Hall Thruster Performance," *AIAA Journal*, 2003-4550.

[7] Pierson, Bion L., and Kluever, Craig A. "Three-Stage Approach to Optimal Low-Thrust Earth-Moon Trajectories," *Journal of Guidance, Control, and Dynamics*, Vol. 17, No. 6, 1994.

[8] Kluever, Craig A., Pierson, Bion L., "Optimal Low-Thrust Three-Dimensional Earth-Moon Trajectories," *Journal of Guidance, Control, and Dynamics*, Vol. 18, No. 4, 1995.

[9] Kluever, Craig A. "Optimal Earth-Moon Trajectories Using Combined Chemical-Electric Propulsion," *Journal of Guidance, Control, and Dynamics*, Vol. 20, No. 2, 1997.

[10] Herman, Albert L., Conway, Bruce A. "Optimal, Low-Thrust, Earth-Moon Orbit Transfer," *Journal of Guidance, Control, and Dynamics*, Vol. 21, No. 1, 1998.

[11] Kim, Mischa. "Continuous Low-Thrust Trajectory Optimization: Techniques and Applications," PhD Dissertation, Virginia Polytechnic Institute, 2005.

[12] Thorne, James D. "Optimal Continuous-Thrust Orbit Transfers," PhD Dissertation, Air Force Institute of Technology, 1996.

[13] Thorne, James D., Hall, Christopher D. "Minimum-Time Continuous-Thrust Orbit Transfers Using the Kustaanheimo-Stiefel Transformation," *Journal of Guidance, Control, and Dynamics*, 1997, Vol. 20, No. 4.

[14] Whiting, James K. "Orbital Transfer Trajectory Optimization," Masters Thesis, Massachusetts Institute of Technology, 2004.

[15] Hunziker, Raul R, "Low-Thrust Station Keeping Guidance for a 24-Hour Satellite," *AIAA Journal,* Vol. 8, No. 7, pp. 1186-1192, 1970.

[16] Oleson, Steven R., Myers, Roger M., Kluever, Craig A. "Advanced Propulsion for Geostationary Orbit Insertion and North-South Station Keeping," *Journal of Spacecraft and Rockets*, Vol. 34, No. 1, 1997.

[16] Oleson, Steven R., Myers, Roger M., Kluever, Craig A.

[17] Chan, J., Ariasti, A., Hur-Diaz, S "Comparisons of two station-keeping strategies for ionic propulsion systems," Flight Mechanics Symposium at NASA Goddard Space Flight Center*,* October 28-30, 2003.

[18] Losa, Damiana, "Electric Station Keeping of Geostationary Satellites: a Differential Inclusion Approach," 44th IEEE Conference on Decision and Control, December, 2005.

[19] Conway, Bruce A., Larson, K.M, "Collocation Versus Differential Inclusion in Direct Optimization," *Journal of Guidance, Control, and Dynamics*, Vol. 21, No. 5, 1998.

[20] Edelbaum, Theodore N. "Optimal Low-Thrust Rendezvous and Station Keeping," *Journal of Spacecraft and Rockets,* Vol. 40, No. 6, 1964.

[21] Billik, B. H., "Some Optimal Low-Acceleration Rendezvous Maneuvers," *AIAA Journal*, Vol. 2, No. 3, pp. 510-516, 1964.

[22] Euler, E. "Optimal Low-Thrust Rendezvous Control," *AIAA Journal*, Vol. 7, No. 6, pp. 1140-1144, Jan-June 1969.

[23] Dittberner, W., Stuhlinger, E., "Rendezvous Missions to Minor Planets with Electrically Propelled Spacecraft," AIAA International Electric Propulsion Conference, Oct. 30-Nov 1, 1979.

[24] Aleshin, M., and Guelman, M., "Optimal Power Limited Rendezvous with Fixed Terminal Approach Direction," *Journal of Guidance, Control, and Dynamics*, Vol. 19, No. 5, pp. 1124-1133, 1996.

[25] Guelman, M., Aleshin, M. "Optimal Bounded Low-Thrust Rendezvous with Fixed Terminal-Approach Direction," *Journal of Guidance, Control, and Dynamics*, Vol. 24, No. 2, pp. 378-385,March-April 2001.

[26] Park, S.Y., and Junkins, John L., "Orbital Mission Analysis for a Lunar Mapping Satellite," *The Journal of the Astronautical Sciences*, Vol. 43, No. 2, pp. 207-217, April-June 1995.

[27] Ramanan, R.V., and Adimurthy, V, "An Analysis of Near-Circular Lunar Mapping Orbits," *Journal of Earth System Sciences*, pp. 619-626, Dec. 2005.

[28] Kaufman, B., Middour, J., and Richon, K., "Mission Design of the Clementine Space Experiment," *AAS*-95-124, February, 1995.

[29] Richon, Karen V., and Newman, Lauri Kraft, "Flight Dynamics Support for the Clementine Deep Space Program Science Experiment (DSPSE) Mission," *Advances in the Astronautical Sciences*, Vol. 90, No.2, pp. 2045-2064, 1995.

[30] Folta, David and Beckman, Mark, "The Lunar Prospector Mission: Results of Trajectory Design, Quasi-Frozen Orbits, Extended Mission Targeting, and Lunar Topography and Potential Models," *Advances in the Astronautical Sciences*, Vol. 103, No. 2, pp. 1505-1523, 1999.

[31] Folta, D., Galal, K., and Lozier D., "Lunar Prospector Frozen Orbit Mission Design," Astrodynamics Specialist Conference, AIAA-98-4288, 1998.

[32] Beckman, Mark, and Folta, David, "Mission Design of the First Robotic Lunar Exploration Program Mission: The Lunar Reconnaissance Orbiter," AAS/AIAA Astrodynamics Specialist Conference, AAS-05-300, 2005.

[33] Beckman, Mark, "Mission Design for the Lunar Reconnaissance Orbiter," 29th Annual AAS Guidance and Control Conference, February 2006.

[34] Escobal, Pedro R. *Methods of Astrodynamics*. John Wiley & Sons, 1969.

[35] Skinner, David L. "QUICK – An Interactive Software Environment for Engineering," *AIAA Computers in Aerospace Conference*, AIAA-1989-3051, pp. 542-563, 1998.

[36] Skinner, David L. "Spacecraft Design Applications of QUICK," *Aerospace Design Conference,* AIAA-1992-1111.

[37] Vallado, David A. *Fundamentals of Astrodynamics and Applications*, Microcosm Press, Second Edition, 2004.

[38] Konopliv, A.S. “Recent Gravity Models as a Result of the Lunar Prospector Mission,” *Icarus*, Volume 150, Issue 1, pp. 1-18, 2001.

[39] Shampine, L. F. and M. K. Gordon, *Computer Solution of Ordinary Differential Equations: the Initial Value Problem*, W. H. Freeman, San Francisco, 1975.

[40] Forsyth, A.R., *Calculus of Variations*, Dover, 1960.

[41] Bryson, A., and Ho, Yu-chi, *Applied Optimal Control*, Taylor & Francis, Revised Edition, 1975.

[42] Lewis, Frank, and Syrmos, Vassilis, *Optimal Control*, Wiley Interscience, Second Edition, 1995.

[43] Betts, John T., “Survey of Numerical Methods for Trajectory Optimization,” *AIAA Journal of Guidance, Control, and Dynamics*, Vol. 21, No. 2, pp. 193-207, March-April 1998.

[44] Hargraves, C. R., Paris, S. W., “Direct Trajectory Optimization Using Nonlinear Programming and Collocation,” *Journal of Guidance, Control, and Dynamics*, Vol. 10, No. 4, pp. 338-342, 1987.

VITA

Nathan Robert Harl was born in Farmington, Missouri on May 11, 1983 to Fred Harl and Nancy Yount. He graduated from Valley R-6 High School in Caledonia, Missouri as Valedictorian in the spring of 2001 and enrolled at the University of Missouri-Rolla for the following fall. In May of 2005, he graduated with a Bachelors of Science degree in Aerospace Engineering from UMR. He later received his Masters degree in Aerospace Engineering from UMR in May of 2007. While at UMR, Nathan was a three-year member of UMR's newspaper, *The Missouri Miner*, working as the News Editor and Managing Editor. He also served as a member of AIAA, Sigma Gamma Tau, and the MR SAT satellite design team.